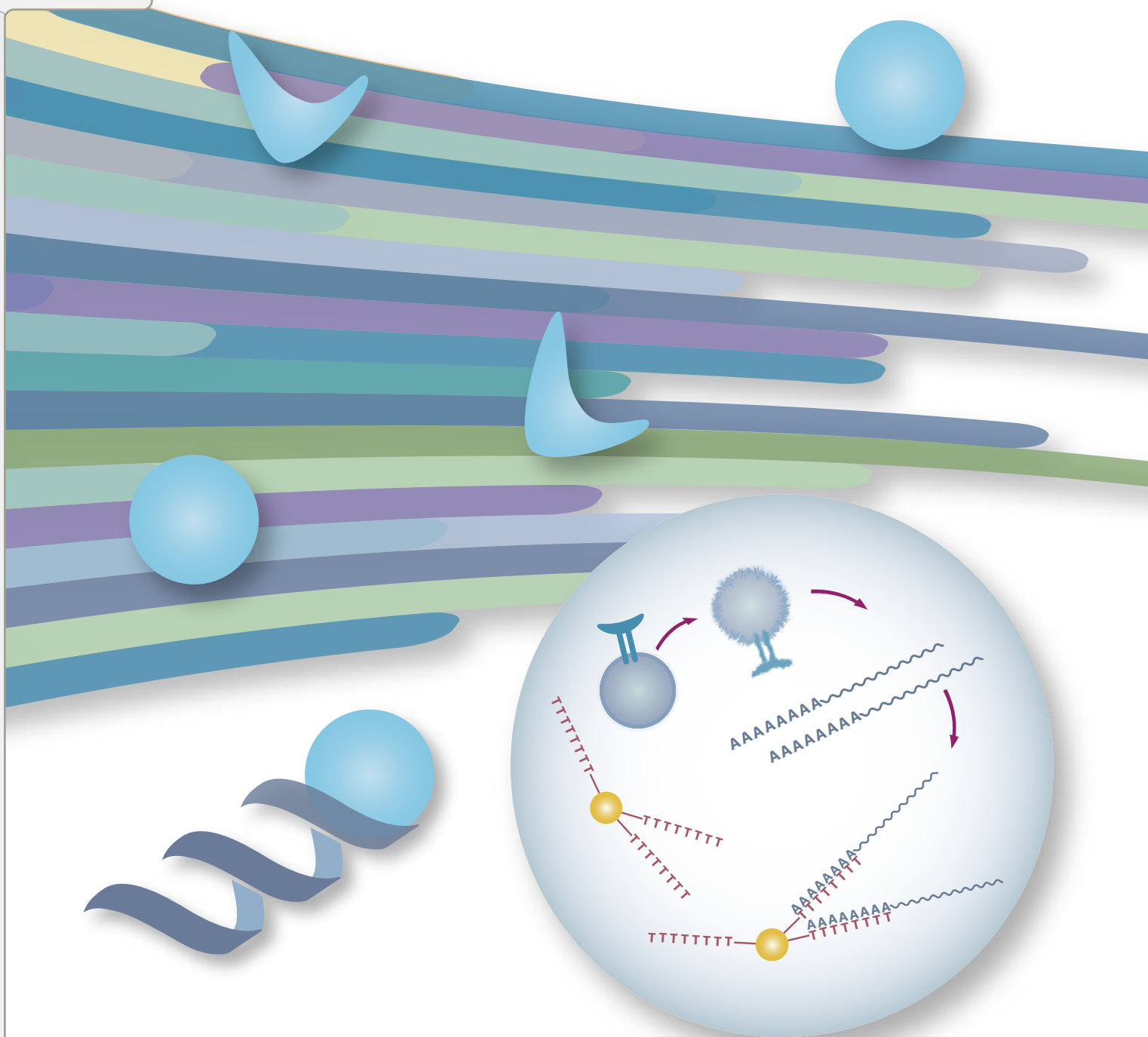


Tailored Microfluidic Droplets for High-throughput Biological Experimentation

Tailored Microfluidic Droplets for High-throughput Biological Experimentation



DISS. ETH NO. 24689

***Tailored microfluidic droplets for high-throughput
biological experimentation***

A thesis submitted to attain the degree of
DOCTOR OF SCIENCES of ETH ZURICH
(Dr. sc. ETH Zurich)

presented by

YUN DING

BEng. in Pharmaceutical Engineering, Zhejiang University, China (2009)
MSc. in Chemical and Bioengineering, ETH Zurich, Switzerland (2012)

born on 22.07.1986

citizen of China

accepted on the recommendation of

Prof. Andrew deMello
Prof. Giuseppe Storti
Dr. Roger Geiger

2017

**“To turn caring into action, we need to see a problem,
find a solution, and deliver impact.”**

- Bill Gates

Co-founder of Bill & Melinda Gates Foundation

Acknowledgements

This thesis is a testimony to my doctoral study and research. It would not be possible without the help and support of many mentors, colleagues and friends I am fortunate to have.

First and foremost, I would like to thank Prof. Andrew deMello for giving me the opportunity of pursuing my PhD dream. I deeply appreciate his great supervision, advice, inspiration, and especially, creating extraordinary friendly and motivating research environment for his students. I will never forget his encouragement, help and trust when I encountered difficulties. I want to thank my co-examiners, Prof. Storti and Dr Geiger, for their scientific support. Especially, I own Prof. Storti big thanks for his extremely kind help in academic also during my master study. The collaboration with Dr Geiger in that fascinating projects is exciting and full of pleasure. I memorise many fun moments, such as playing ping pong and hunting for yummy food together.

I would like to thank all the group members who either helped me or making the lab a joyful place to work: Simon, Flora, Gregor, Martina, Akkapol, Nadia, Jeff... I would like to dedicate a special mention to Ioannis. We shared a lot of wonderful and unforgettable moments together, such as exchanging "great ideas" and discussing "small business". I am sure our "friend-ship" will voyage for a long time. Of course, I appreciate the solid support from all the members of "Team China" in the lab, including both formal members and honourable members who are twin brothers from Poland, Tomasz and Bartosz.

Additionally, I want to give my special thanks and great respect to the principal of my primary school, Mrs Fang Aizhen. I feel indebted for her significant education and great appreciation for me during my early years of learning. One year after I graduated, she retired. I am very touched by her continuing to care and encourage me from time to time even until recently. I cannot wait to share the news with her once I get the degree.

Last but not least, I thank for my parents' unconditional love. This thesis should be one of the best gifts for them from their proud child.

Zürich, 4th September 2017

Abstract

The past 15 years has seen considerable progress in the development of droplet-based microfluidics with respect to basic manipulations and potential applications. Such flow-based miniaturized systems can generate a large number of nL- and pL-scale droplets with an unprecedented degree of control over droplet properties. These features combined with the ability to adjust the chemical or biological payload of the formed droplets make droplet-based microfluidic systems highly promising vehicles for large-scale biological experimentation. Unsurprisingly, recent years have witnessed a startling increase in the use of droplet-based microfluidics in a wide variety of chemical, and particularly, cell biological and biomedical assays because of the simple fact that physical processes can be more easily controlled and harnessed when analytical volumes are reduced to small scales.

The Chapter 1 introduces some of the most important aspects of droplet-based microfluidics in respect of their application in chemical and biological experimentation. Specifically, some of the most interesting functional tools for droplet formation, reagent encapsulation and manipulation have been described, and issues relating to droplet stability summarised.

That said, although a large number of methods for droplet formation and manipulation have been presented, there is still a significant need for novel methods that exert enhanced control over droplet properties, such as size, payload and location to tailor droplets for a specific application. To this end, studies presented in Chapter 2 and Chapter 3 are aimed at the development of novel microfluidic architectures that allow bespoke-droplet generation and manipulations.

Chapter 4 presents a discussion of key applications of droplet-based microfluidics in the biological sciences. Subsequently, integration of functional microfluidic components is used to define and develop a novel analytical platform for high-throughput profiling of antigen-specific T cell receptors at the single cell level. Results of these proof-of-principle studies are provided in Chapter 5.

Zusammenfassung

In den letzten 15 Jahren gab es grosse Fortschritte in der Entwicklung von Tröpfchen-basierter Mikrofluidik (droplet microfluidics) im Hinblick auf elementare Handhabungsschritte und deren Anwendungen. Solche miniaturisierte Systeme, basierend auf kontinuierlichem Durchfluss, erlauben die Erzeugung von nL- und pL-Tröpfchen in grosser Anzahl und gleichzeitiger Kontrolle der Tröpfcheneigenschaften. Diese Eigenschaften und die Möglichkeit der gezielten Ausstattung der Tröpfchen mit einem chemischen oder biologischen Fracht machen sie zu verheissungsvollen Vehikeln für grossangelegte biologische Experimente. Im Verlauf der letzten Jahre ist die Anzahl der Tröpfchen-basierten Mikrofluidik Anwendungen für chemische und speziell biochemische Analysen stetig gestiegen, dies ist zurückzuführen auf die einfachere Kontrolle und Nutzung der physikalischen Prozesse hervorgerufen durch die Verkleinerung der analytischen Volumen.

Kapitel 1 erklärt wichtige Aspekte der Tröpfchen-basierten Mikrofluidik im Hinblick auf deren Anwendung in chemischen und biochemischen Experimenten. Es wird speziell Augenmerk auf die wichtigsten funktionellen Werkzeuge für Tröpfchenerzeugung gelegt. Weiters wird auf Techniken zur Reagenzien Verkapselung und Manipulation und der damit verbundenen Tröpfchenstabilität eingegangen.

Trotz der besprochenen grossen Anzahl an Methoden für die Tröpfchenerzeugung und Handhabung gibt es noch grosses Verbesserungspotential, etwa bei der Kontrolle von Eigenschaften wie der Grösse, Ausstattung der Tröpfchen mit einer Fracht und deren Lage im Tröpfchen für spezielle Anwendungen. Die Untersuchungen in Kapitel 2 und 3 sind darauf ausgerichtet die Tröpfchenerzeugung und Handhabung zu optimieren.

Kapitel 4 zeigt Schlüsselapplikationen für Tröpfchen-basierte Mikrofluidiksysteme in biologischen Wissenschaften. Weiters wird die Entwicklung einer neuartigen analytischen Plattform für hoch-durchsatz Analyse von Antigen spezifischen T Zellen-Rezeptoren auf Einzelzellebene, ermöglicht durch Integration von funktionellen mikrofluidischen

Komponenten, erläutert. Die Resultate dieser Machbarkeitsstudie sind in Kapitel 5 wiedergegeben.

Contents

Acknowledgements	iii
Abstract	v
Zusammenfassung.....	vi
Contents	ix
List of Figures	xii
List of Tables.....	xx
List of Equations.....	xxi
Chapter 1 Droplet-based microfluidics.....	23
1.1 Droplet generation.....	23
1.2 Unit operations.....	26
1.3 Droplet stability.....	30
1.4 Particle encapsulation and Poisson statistics	32
1.5 Conclusions	35
Chapter 2 The “V-junction”: a novel structure for high-speed generation of bespoke droplet flows	37
2.1 Introduction	37
2.2 Materials and Methods.....	40
2.3 Results and Discussion	41
2.3.1 Binary mode: a world-to-chip interface that prevents unsolicited droplet introduction	41
2.3.2 A universal droplet generator with a magic knife	46
2.3.3 The return of droplets: temporal gradient formation	50
2.4 Conclusions	51

Chapter 3	Microfluidic-based droplet and cell manipulations using artificial bacterial flagella.....	53
3.1	Introduction.....	53
3.2	Equipment and Methods.....	55
3.2.1	ABF fabrication and suspension preparation.....	55
3.2.2	PDMS chip fabrication and ABF encapsulation.....	55
3.2.3	Magnetic control system.....	56
3.2.4	Treatment of biological cells.....	56
3.3	Experiment, Results and Discussion.....	56
3.3.1	Operation of an ABF inside a microfluidic droplet.....	56
3.3.2	Manipulation of microdroplets.....	60
3.3.3	A motorized cell.....	62
3.4	Conclusions.....	63
Chapter 4	From single-molecule detection to next-generation sequencing: microfluidic droplets for high-throughput nucleic acid analysis	65
4.1	The role of droplets in next-generation sequencing.....	65
4.1.1	Next-generation sequencing: an introduction.....	65
4.1.2	Droplet partitioning.....	67
4.1.3	Droplet-based nucleic acid amplification.....	69
4.2	One drop at a time: high-throughput nucleic acid assays	72
4.2.1	Single-molecule genomic screening.....	72
4.2.2	Single-cell genomic and transcriptomic investigations.....	74
Chapter 5	High-throughput profiling of antigen-specific T cell receptors using droplet-based microfluidics	79
5.1	Introduction.....	79
5.2	Workflow and Methods.....	81
5.2.1	Design of the microfluidic workflow.....	81
5.2.2	Microfluidic device and fabrication	84
5.2.3	Cell cloning.....	84
5.2.4	Reagents and materials.....	85
5.3	Results and Discussion	85
5.3.1	Co-encapsulation	85
5.3.2	mRNA capture and cDNA synthesis.....	89

5.3.3	TCR linkage	92
5.4	Further improvements and next steps.....	93
5.5	Conclusions.....	95
Chapter 6 Conclusions and Outlook		97
6.1	Portable droplet-based microfluidics for point-of-care diagnostics.....	98
6.2	Large scale integration to answer complex or unknown questions.....	98
Appendix A Supplementary information for Chapter 2.....		100
A.1	Operational upper flow rate limits in open-mode for varying V-junction angles	100
A.2	Measurement of droplet volumes.....	102
A.3	Comparison of the V-junction and T-junction.....	103
A.3.1	Size gradients.....	103
A.3.2	Relationship between size and frequency/spacing.....	104
Appendix B Supplementary information for Chapter 3.....		107
B.1	Assessment of swimming steadiness.....	107
B.2	Cell viability assessment	107
Appendix C Supplementary information for Chapter 5.....		109
C.1	Directly increase average bead number.....	109
C.2	Verify mRNA capturing by PCR	109
C.3	Optimization of droplet stability for PCR.....	110
Appendix D Supplementary information of videos		112
D.1	Supplementary videos for Chapter 2	112
D.2	Supplementary videos for Chapter 3	113
References		114
Curriculum Vitae.....		134

List of Figures

Figure 1:1 Structures of four common types of droplet generator.	24
Figure 1:2 Device geometry and mechanism of drop formation through confinement gradients. Such an approach allows high-throughput production of controlled emulsions. Images show an emulsion containing droplets with variable payloads but constant size. Adapted from reference [16] with permission.	25
Figure 1:3 (a) Schematic of a droplet barcode generator. The inlet flows of two fluorescent dyes (CF 647 and CF 488A) are first paired with an individual buffer flow each before being joined together. These aqueous flows are generated using four syringe pumps programmed to dynamically change the ratio of flow rates, whilst ensuring that the total aqueous flow rate is constant. FC-40 is used as the continuous oil phase to shear off the aqueous stream and form isolated droplets. (b) Fluorescence image of barcoded droplets. The left half of the frame (i) records the green signal and right half (ii) records the red signal. Channels and the direction of flow are marked by lines and arrows respectively. With this method, over 500 uniquely barcoded droplets were generated in less than 20 seconds[17].....	25
Figure 1:4 Examples of droplet unit operations. (a) Pillar-induced droplet merging[31]. (b) A selective droplet merging system[33]. (c) A microdroplet dilutor[35]. (d) Generation of concentration gradients[36]. (e) Parallel synchronization[42]. (f) Geometrically mediated droplet splitting[40]. (g) Droplet splitting used for heterogeneous phase separation[41]. (h) Electric field triggered picoinjection[37]. (i) A variant structure for injecting sample into droplets[39]. (j) Droplets extract molecules from the contact substrate[38]. (k) Fluorescence-activated droplet sorting[45]. (l) Density-dependent sorting by using the standing surface acoustic wave[46]. (m) A multifunctional droplet trap[48]. (n) On-demand droplet release[49]. (o) On-chip droplet incubation with arrays[51]. Images are adapted from corresponding references with permission.	27
Figure 1:5 1-million droplet array for dPCR contains a single droplet generator, 256 splitters and a 27 mm × 40.5 mm viewing chamber. Adapted from reference [53] with permission.	28
Figure 1:6 Complex microfluidic droplet workflows enable long and accurate DNA sequencing reads via barcoding short-read fragments. Left: Schematics and false-coloured images of devices. Right:	

Cartoons of molecular processes occurring inside droplets. *First stage* (top): Single templates are encapsulated into droplets by a flow-focusing drop maker. Inside each droplet PCR or MDA is used to amplify the single template. *Second stage* (middle): A split-merger is used to add transposases and precisely adjust template concentrations. Template droplets are injected on the left side, split at junction (1) so that 1/10th of the droplet continues to pair with a reagent droplet generated on-chip at (2), with the pair merging at the channel expansion (3). Inside droplets, the transposase reaction fragments templates and adds adaptors to each fragment. *Third stage* (bottom): The device used for attaching barcodes to DNA fragments. Template droplets (1) and barcode droplets (2) are injected into the device where they pair with each other and a large PCR reagent droplet generated on-chip (3). The three droplets merge at the electrode (4) and are split into smaller droplets for thermal cycling (5). Inside droplets, barcodes are spliced onto fragments by overlap-extension PCR. Scale bars are 100 μm . Adapted from reference [59] with permission..... 29

Figure 1:7 Probability distribution functions for the number of particles per droplet according to Poisson statistics. Curves are plots for N equal to 0.1, 0.3, 0.5, 1, 2, 3, 4, 5, 6 and 7 respectively. 32

Figure 1:8 Variation of target copies per droplet as a function of the fraction of positive droplets in ddPCR. This curve can be directly used to correct ddPCR data. Adapted from reference [82] with permission..... 34

Figure 1:9 The number of positive droplets is directly related to the concentration of target in the sample. Adapted from reference [82] with permission..... 35

Figure 2:1 (a) Schematic of the V-junction structure containing an oil inlet 1, side channel 2 for water introduction, side channel 3 for control, and a main channel and observation zone 4. In the current design, all channels are 50 μm in height. The angle between the two side channels is 60°. (b-d) Schematic illustration of chip operation. (b) A 30 cm long control-tubing connected at the end of channel 3, all the system is filled with oil. (c) Open-mode: with oil continuously being infused, the water phase begins to enter channel 2. Air bubbles, transitional emulsions and water are drained through channel 3. (d) Closed-mode: once impurities have been completely removed, the control-tubing is blocked and water enters the main channel forming stable droplets..... 39

Figure 2:2 PIV analysis of two basic operation modes. The speed and direction of oil flow are indicated with arrows. (a) In open-mode, the oil flow goes into both the main channel and the side channel. A barrier flow by oil (marked with a hollow pink arrow) prevents the water phase from entering the main channel. (b) In closed-mode, no net flow occurs in the control channel. The water phase creates droplets at the main channel by shearing in the oil flow. Video for both cases is provided in the Appendix D.1, VideoS 2. The scale bar is 50 μm 41

Figure 2:3 Sequence of steps used to create stable water droplets from the first one. (a-c) Open-mode. (a) The initial chaotic mixture of phases is eliminated. (b) Adjusting the water flow rate leads to the desired droplet size at (h). (c) When the system has stabilized droplets are generated in the

control channel. (d-h) Switch to closed-mode. (d-g) The water phase stops, recedes and moves forward. (h) The first droplet in main channel is generated. Subsequent droplets can be seen in VideoS 3. The scale bar is 200 μm 42

Figure 2:4 Measurement of droplet areas for the first 25 droplets (area standard deviation = 1.8%)..... 43

Figure 2:5 Electrical equivalent circuit models for the two modes. (a) Open-mode. (b) Closed-mode. 45

Figure 2:6 Images showing clean sample switching. (a-d) Water droplets are generated by the method illustrated in Figure 2:3. (e) By opening the control-tubing and removing the water input tubing, oil refills the entire chip. (f) Connection of the ink input tubing. Initial unwanted impurities are removed until ink droplets are generated in the control channel (g). (h) Closure of the control tubing causes stable ink droplet generation in the main channel. The scale bar is 200 μm 46

Figure 2:7 (a) A droplet size gradient generated by linearly increasing suction at the control channel. Images (ai) to (aiii) display the full sequence of droplet formation (consisting of 72 droplets). Numbers on droplets indicate droplet ID. The scale bar is 200 μm . Small ‘satellite’ droplets in the pictures originate from oil impurities (see VideoS 4). (b) The area of the droplets for (a) is plotted, with the largest 15910 μm^2 (~900 pl in volume) and the smallest 416 μm^2 (~8 pl in volume)..... 47

Figure 2:8 Plot for relationship between droplet generation frequency and size for V and T when oil flow rates both are 2 $\mu\text{l}/\text{min}$. Detail measurement is available in Appendix A.3.2..... 48

Figure 2:9 Four size series of droplets are generated at a V-junction and pass through a microfluidic network. The scale bar is 300 μm . The corresponding video is shown in VideoS 5..... 49

Figure 2:10 Image showing the formation of small droplets by application of a slight negative pressure in the control channel. Such droplets are obtained by splitting the forming droplet into two unequal daughter droplets. Smaller droplets, with a size of 4.0 ± 0.6 μm in diameter, are conveyed along the control channel. The area marked with a purple dashed box is magnified to highlight these small droplets. The scale bar is 50 μm . The corresponding video is shown in VideoS 6..... 49

Figure 2:11 Generation of residence time gradients. (a) Droplets are generated in the control channel under negative pressure. (b) Water infusion is stopped. (c-d) Subsequently, a positive pressure is applied on the control channel: droplets come back and enter the main channel in a reversed sequence. The scale bar is 200 μm . The associated VideoS 7 is available. 50

Figure 2:12 Variation of residence time of droplets in the sequence (*i.e.* temporal gradient) is measured at the area marked with the dashed box in Figure 2:11d. 51

Figure 3:1 (a) Illustration of a helical ABF propelled by a rotating weak magnetic field B ; (b) SEM image of a printed (and uncoated) MS array on a glass substrate (scale bar is $10\ \mu\text{m}$); (c) Schematic of the PDMS microdevice that contains a flow focusing structure for encapsulating ABFs in droplets. Port A serves as the oil inlet and port B is coupled to a chip-to-world connector, from which the aqueous suspension of ABFs is introduced..... 57

Figure 3:2 (a) Image showing the formation of an ABF-containing droplet. The ABF is shown within the white dotted circle; (b) A time-lapse image showing controlled locomotion of an ABF within a droplet. The magnetic field is $90\ \text{Hz}$ and $9\ \text{mT}$; (c) Variation of ABF position and speed for experiment shown in (b). The upper plot illustrates the x,y position as a function of time and the lower plot shows the variation of velocity in the x direction. It is noted that when the ABF reaches the droplet boundary (at 17.5s), the net displacement and average speed in x are both zero. Scale bars correspond to $100\ \mu\text{m}$ 58

Figure 3:3 (a) Time lapse images of an ABF transporting a microdroplet within a $25\ \mu\text{m}$ deep PDMS chamber, under the application of a $70\ \text{Hz}$, $7\ \text{mT}$ magnetic field. The scale bar corresponds to $50\ \mu\text{m}$; (b) Assessment of the relative distance between the transported droplet and a reference droplet as a function of time..... 59

Figure 3:4 (a) A time-lapse image showing the transportation of a large droplet by an ABF across a $25\ \mu\text{m}$ deep PDMS chamber, under the application of a $70\ \text{Hz}$, $7\ \text{mT}$ magnetic field. Note the “swinging” behaviour observed in region A; (b) A time-lapse image showing two large droplets being simultaneously transported along a $100\ \mu\text{m}$ deep PDMS chamber; (c) Schematic explanation of the “soft” adhesion observed between surfactant coated droplets and the tip of an ABF. The scale bar corresponds to $20\ \mu\text{m}$ and the straight black line defines the chamber wall..... 60

Figure 3:5 Swimming characterization in FC-40 oil (containing 3% w/w PFPE-PEG-PFPE tri-block surfactant) along a $100\ \mu\text{m}$ deep PDMS chamber. (a) Forward swimming speed of ABFs as a function of magnetic field strength and rotation frequency; (b) Evaluation of the steadiness of swimming. Here, higher values represent reduced steadiness. The degree of “wobbling” and “shifts” in movement are two major (negative) factors used to assay the swimming performance of ABFs (the assay methodology is provided in Appendix B.1). The combination of these data provides the range of operational parameters that deliver stable swimming performance..... 61

Figure 3:6 The process by which a motorized cell is assembled and disassembled. In (i) and (ii) an ABF approaches the desired cell, contacts it and assembles. The B-cell-ABF assembly then moves forward following the direction of the applied rotating magnetic field (iii and iv). To disassemble, the rotating direction of magnetic field is simply reversed, allowing the ABF to move back and detach from the cell; (b) A time-lapse image of a cell being dragged; (c) A time-lapse image of the process of forming an ABF-cell-ABF configuration. The scale bar corresponds to $20\ \mu\text{m}$ 63

Figure 4:1 Classification of next-generation sequencing methods. Data are based on throughput metrics for different platforms since their introduction. Results are visualised by plotting

throughput in raw bases per run versus read length. Adapted from reference [185] under a CC BY license..... 66

Figure 4:2 Workflow comparison between two commercial synthetic long-read sequencing platforms. Left: Illumina's *TruSeq* technology. Genomic DNA templates are fragmented into 8–10 kb pieces. They are then partitioned into a microtitre plate, such that there are around 3,000 templates in a single well. Within the plate, each fragment is sheared to around 350 bp and barcoded with a single barcode per well. The DNA is then be pooled and sent through standard short-read pipelines. Right: 10X Genomics' emulsion-based sequencing platform. With as little as 1 ng of starting material, the *GEMCode* can partition arbitrarily large DNA fragments, up to ~100 kb, into micelles (called 'GEMs') along with gel beads containing adapter and barcode sequences. GEMs typically contain ~0.3× copies of the genome and 1 unique barcode out of 750,000. Within each GEM, the gel bead dissolves and smaller fragments of DNA are amplified from the original large fragments, each with a barcode identifying the source GEM. After sequencing, the reads are aligned and linked together to form a series of anchored fragments across a span of ~50 kb. Unlike the Illumina system, this approach does not attempt to get full end-to-end coverage of a single DNA fragment. Instead, the reads from a single GEM are dispersed across the original DNA fragment and the cumulative coverage is derived from multiple GEMs with dispersed—but linked—reads. Adapted from reference [192] with permission..... 67

Figure 4:3 (a) Well-based high-throughput sequencing of an antibody repertoire. (i) B cell populations are sorted for desired phenotype. (ii) Single cells are isolated by random settling into wells (56 µm diameter) printed in PDMS slides (170,000 wells/slide); 2.8 µm poly(dT) microbeads are also added to the wells (average 55 beads/well). (iii) Wells are sealed with a dialysis membrane and equilibrated with lysis buffer to lyse cells and anneal VH and VL mRNAs to poly(dT) beads. (iv) Beads are recovered and emulsified for cDNA synthesis and linkage PCR to generate an ~850-base pair VH-VL cDNA product. (v) Next-generation sequencing is performed to sequence the linked strands. (vi) Bioinformatic processing is used to analyse the paired VH:VL repertoire. Adapted from reference [195] with permission. (b) Droplet-based high-throughput sequencing of an antibody repertoire. (i) An axisymmetric flow-focusing nozzle isolated single cells and poly(dT) magnetic beads into emulsions of predictable size distributions. (ii) Single-cell VH and VL mRNAs annealed to poly(dT) beads within emulsion droplets. (iii) poly(dT) beads with annealed mRNA were recovered by emulsion centrifugation to concentrate the aqueous phase (left) followed by diethyl ether destabilization (right). (iv) Recovered beads were emulsified for cDNA synthesis and linkage PCR to generate an ~850-base pair VH-VL cDNA product. (v) Next-generation sequencing analysis. Adapted from reference [196] with permission..... 68

Figure 4:4 (a) Design of a radial PCR device. The device contains an oil inlet A that joins two aqueous inlet channels B1 and B2 to form droplets at a T-junction C. The droplets pass through the inner circles (500 µm wide channels) in the hot zone D to ensure initial denaturation of the template and travel on to the periphery in 200 µm wide channels where primer annealing and template extension occur E. The droplets then flow back to the center, where the DNA is denatured

and a new cycle begins. Finally, the droplets exit the device after 34 cycles F. Adapted from reference [96] with permission. (b) ddPCR enables the absolute quantitation of nucleic acids from a sample in a high-throughput. The process includes three steps: on-chip droplet generation, off-chip droplet incubation and on-chip detection of fluorescence. Adapted from reference [155] with permission. (c) Workflow of centrifugal step emulsification without associated dead volumes. The system is located on a spinning disk and consists of an inlet chamber (i), a channel (ii) which connects the inlet to a nozzle, and a droplet collection chamber (iii). The inlet chamber is located closer to the centre of rotation than the droplet collection chamber and both chambers are equipped with an air vent. *Step 1:* the inlet chamber is filled with oil. *Step 2:* during centrifugation, the oil flows to the radial outer droplet collection chamber. *Step 3:* a sample is introduced to the inlet. *Step 4:* the sample is emulsified during centrifugation by step emulsification, and some sample remains in the inlet channel. *Step 5:* oil is filled into the inlet. *Step 6:* during centrifugation, the oil flows to the droplet collection chamber pushing the remaining sample through the nozzle which enables the production of droplets with zero dead volume. Adapted from reference [222] with permission. 73

Figure 4:5 (a) *Drop-seq*. A custom-designed microfluidic device joins two aqueous flows before their compartmentalization into discrete droplets. One flow contains cells, and the other flow contains barcoded primer beads suspended in a lysis buffer. Immediately following droplet formation, the cell is lysed and releases its mRNAs, which then hybridize with primers on the microparticle surface. The droplets are broken by adding a reagent to destabilize the oil-water interface, and the microparticles collected and washed. The mRNAs are then reverse-transcribed in bulk, forming STAMPs (single-cell transcriptomes attached to microparticles), and template switching is used to introduce a PCR handle downstream of the synthesized cDNA. Adapted from reference [244] with permission. (b) *In-Drops*. Cells are encapsulated into droplets with lysis buffer, reverse-transcription mix, and hydrogel microspheres carrying barcoded primers. After encapsulation primers are released. cDNA in each droplet is tagged with a barcode during reverse transcription. Droplets are then broken and material from all cells is linearly amplified before sequencing. UMI = unique molecular identifier. Adapted from reference [218] with permission. 75

Figure 5:1 Three general approaches of adoptive cell transfer therapy. Adapted from reference [259] with permission. 80

Figure 5:2 (a) The structure of a T-cell receptor (TCR). The TCR consists of two chains with each chain having a *V* domain and a *C* domain. (b) Universal mRNA capture by an oligo(dT) modified bead. mRNA has a poly(A) tail which is conjugated to oligo(dT). 82

Figure 5:3 Microfluidic workflow for extracting linkage TCR receptors. *Step 1*, T cells and beads (with a lysis buffer) are co-encapsulated within microfluidic droplets. The concentrations of cells and beads are adjusted so that each droplet contains at least one bead, but no more than one cell, assuming Poisson statistics (see Section 1.4 in Chapter 1). Cells are then lysed in droplets, mRNAs released and subsequently captured on beads. *Step 2*, involves the breakage of droplets, collection

of beads and performance of RT to convert the captured mRNAs into cDNAs. *Step 3*, re-encapsulation of single beads into droplets together with linker PCR reagents. TRAs and TRBs can then be amplified and linked within droplets. 83

Figure 5:4 Microfluidic device design for experiments with 10 μm diameter beads. The height of all microfluidic channels is 70 μm . The structure comprises an oil inlet, a bead inlet, a cell inlet (not used in *step 3*). The width of channel in area A is larger than that in area B. The wider channel in area A facilitates a uniform and smooth loading of beads. The channel width in area B is a crucial factor for the size of droplets. 84

Figure 5:5 Bead occupancies are adjusted by controlling the relative flow rates of the aqueous and oil phases. From (a) to (d), the flow rate ratios between the aqueous and oil are 5, 2.5, 1.25 and 0.5 respectively. In (d), 100% observed droplets contain beads with $N = 5.26$. The curves are theoretical Poisson fitting according to the observed N 87

Figure 5:6 Co-encapsulation of cells and 30 μm beads. (a) The image shows single cells and beads at the point of co-encapsulation. (b) Image of a formed droplet population. Bead size distribution is 20 – 40 μm (>80% within range). The corresponding bead number distribution is shown in panel (c). The percentage of empty droplets is below 1.7%, with the average number of beads per droplet being 2.5. The solid curve represents the expected distribution based on Poisson statistics. Scale bars are 100 μm 88

Figure 5:7 Co-encapsulation of cells and 1 μm beads. (a) The microscope image shows droplets containing both beads and single cells moving through a microfluidic device. White artefacts near the top and bottom of droplet trains are a consequence of image processing of background subtraction. The scale bar is 50 μm in length. (b) Frequency distribution of beads (columns). The solid curve represents the expected distribution based on Poisson statistics, $N = 7.0$. (c) Bead distribution for droplets containing a cell, with the solid curve representing the expected distribution based on Poisson statistics, $N = 6.6$ 89

Figure 5:8 Co-encapsulation of T cells and 1 μm oligo(dT) beads within 35 pL volume droplets containing lysis buffer. (a) Image illustrating the process of droplet formation and co-encapsulation. Lysis buffer is introduced through the bead stream. It should be noted that the generated droplet in the image does contain beads. These are difficult to see due to the fact that the droplet is moving at high speed along the channel ($5.5 \text{ cm}\cdot\text{s}^{-1}$). (b) Image of droplets subsequent to production and collected in an off-chip reservoir for observation. For the population shown, 12% of droplets contain a single cell. Scale bars are 50 μm 90

Figure 5:9 (a) Representative data assaying mRNA capture in bulk. Beads are flow-cytometry detected by BD FACSAria III. Figures in each column represent the results of a case using a specific concentration of ATTO647 d(A)25 plus a water control. Figures in the first row are the distinction of beads from other impurity particles using parameters of SSC-A (side scatter pulse area, indicating the surface information, *i.e.* granularity, for the particle) and FSC-A (forward scatter

pulse area, giving a relative size for the particle). Figures in the second row are further distinguishing beads by looking at green (note that beads are coated with FITC) and red (due to the captured ATTO 647) fluorescence signals. Figures in the third row are the number distribution of beads according to the detected intensity of red fluorescence signal (b) Fluorescence images reporting mRNA capture within droplets. Left panel shows a fluorescence image captured using a FITC fluorescein optical filter. The middle panel shows the corresponding bright-field image. The left panel shows the corresponding fluorescence image using an optical filter for ATTO 647. The scale bar is 50 μm 91

Figure 5:10 Droplet-based TCR linkage PCR. (a) cDNA-linked beads were encapsulated in 35 pL droplets at a flow focusing geometry. (b) Image of a droplet population collected in an off-chip reservoir, with approximately 12% droplets containing a single bead. Scale bars in panels (a) and (b) are 50 μm . (c) Gel electrophoresis of PCR products. Lanes 1 and 2 represent an analysis of products from droplet-based PCR, and with lane 3 representing the bulk PCR control. Expected bands for linker TCR PCR should occur at approximately 1 kb for single chains and between 1.5 and 2 kb for linked products. No bands were observed for the negative control (data not shown). 92

Figure 5:11 Schematic of paring one cell and one bead in a droplet..... 94

Figure 5:12 Schematic of injecting an enzyme into droplets to increase the efficiency of linkage PCR. The principle of this method can be referred to elsewhere[37, 55]. 94

List of Tables

Table 1:1 Comparison between mineral oils and fluorinated oils.....	31
Table 1:2 Probability values for N (average particle number per droplet) between 0.1 and 7 under Poisson conditions. The characteristic values discussed in main text are highlighted.....	33
Table 4:1 Emulsion PCR summary	71

List of Equations

(1:1)	32
(1:2)	34
(2:1)	44
(2:2)	44
(2:3)	44
(2:4)	44
(2:5)	45
(2:6)	45
(2:7)	45
(2:8)	45
(2:9)	45
(2:10)	45
(2:11)	45
(2:12)	45
(3:1)	59
(S:1)	102

Chapter 1 Droplet-based microfluidics^ψ

Emulsions (collections of isolated droplets surrounded by a continuous and immiscible carrier fluid) have long been used in chemical and biological experimentation, with the large number of contained droplets serving as isolated vessels in which reactions or assays may be performed[1]. The use of bulk shear forces, although efficient in making large numbers of droplets on short timescales, generates polydisperse droplet populations that prohibit quantitative experimentation[2–4]. Conversely, flow-based microfluidic systems can be used to generate similarly large numbers of droplets, but with an unprecedented degree of control over droplet properties. These features combined with the ability to adjust the chemical or biological payload of the formed droplets make droplet-based microfluidic systems highly promising vehicles for large-scale biological experimentation. Not surprisingly, the past 15 years has seen considerable progress in the development of droplet-based microfluidics with respect to basic manipulations and potential applications. This chapter introduces essential background knowledge regarding droplet-based microfluidic systems, including an assessment of functional components for droplet formation and manipulations, and methods for probing the chemical/biological composition of droplets.

1.1 Droplet generation

Emulsions formed using bulk shear forces have long been used to good effect in areas such as polymer chemistry[5], cosmetic formulations[6] and complex food systems[7]. Despite their utility, the challenges associated with controlling droplet size, composition and population size distributions are immense, making their use in quantitative experimentation demanding at best and impossible at worst. Conversely, droplets (having volumes on the

^ψ This chapter was published in part in: Yun Ding, Jaebum Choo, and Andrew J. deMello, *From Single-Molecule Detection to next-Generation Sequencing: Microfluidic Droplets for High-Throughput Nucleic Acid Analysis*, *Microfluidics and Nanofluidics* 21, 58 (doi:10.1007/s10404-017-1889-4).

femtoliter to nanoliter scale) can be generated in a variety of ways within microfluidic systems. Critically, passive strategies that leverage geometrical variations of fluidic structures can be used to transform arbitrary volumes of fluid into sub-nanoliter droplets at kHz to MHz frequencies[8].

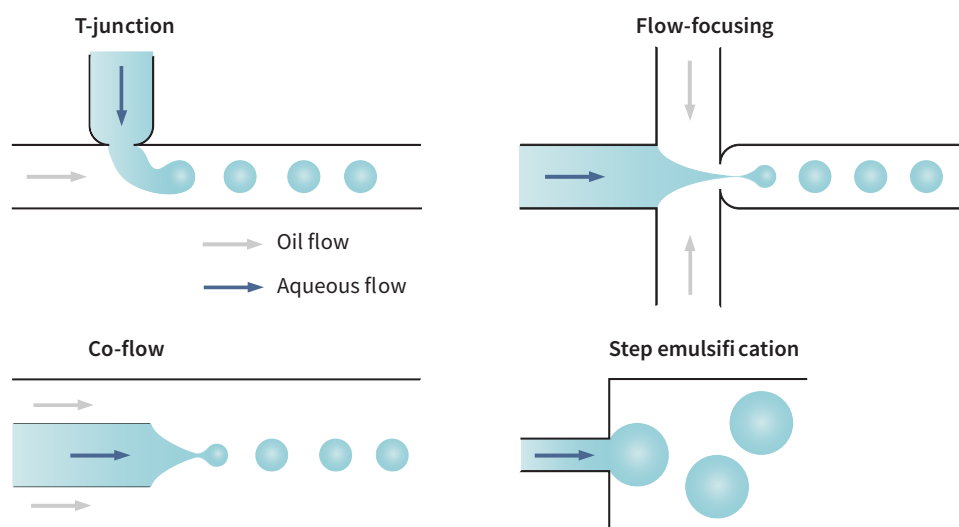


Figure 1:1 Structures of four common types of droplet generator.

The most common strategies for droplet production involve the use of cross-flow structures (T-junctions)[9], flow-focusing geometries[10], co-flow structures[11, 12] and step emulsification[13, 14] (Figure 1:1). In planar, chip-based systems immiscible aqueous and oil streams confined within microfluidic channels are brought together via hydrodynamic forces (typically using syringe or pressure pumps), with droplets (or plugs¹) being formed at the point of confluence. Although the exact droplet generation mechanism is quite different in each these geometries, all involve the establishment of an interface between co-flowing, immiscible fluids, followed by self-segregation of one of the fluids into droplets that are surrounded by the other fluid. Interestingly, variations on the above strategies have also been used to good effect when preparing large populations of droplets[15, 16]. For example, Dangla *et al.* exploited gradients of confinement to realise highly robust droplet formation (Figure 1:2)[16]. Using this method, droplets can be formed due to a curvature imbalance along the interface, without the need for shear associated with the continuous phase flow. In turn, this means that droplet size is primarily determined by the gradient geometry and is insensitive to fluid properties (such as flow rate). Unsurprisingly, such a “pump-free”

¹ Plugs typically are capsule-like droplets squeezed by the side walls of a microchannel.

droplet generation method has wide ranging utility and potential in point-of-care or point-of-use applications.

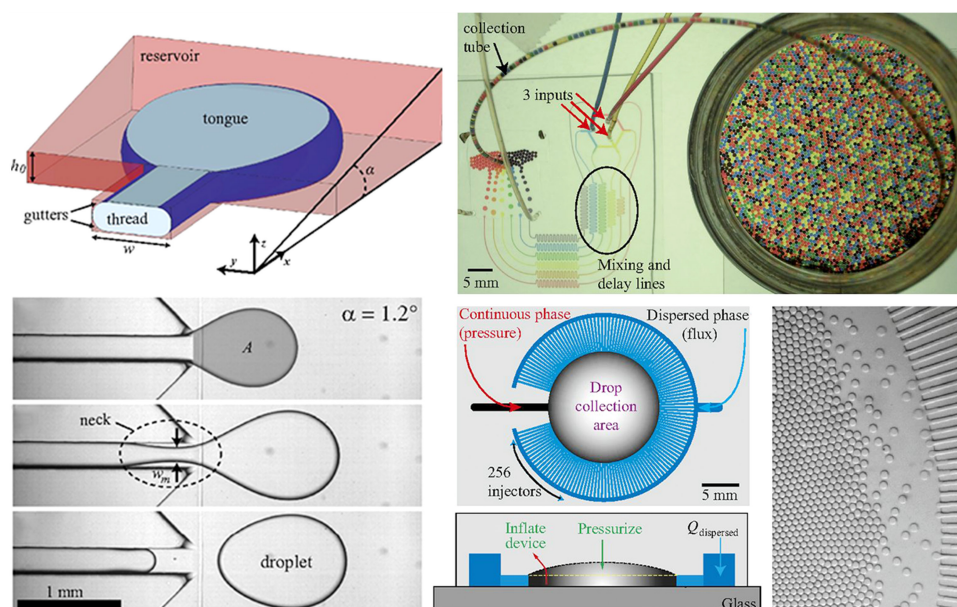


Figure 1:2 Device geometry and mechanism of drop formation through confinement gradients. Such an approach allows high-throughput production of controlled emulsions. Images show an emulsion containing droplets with variable payloads but constant size. Adapted from reference [16] with permission.

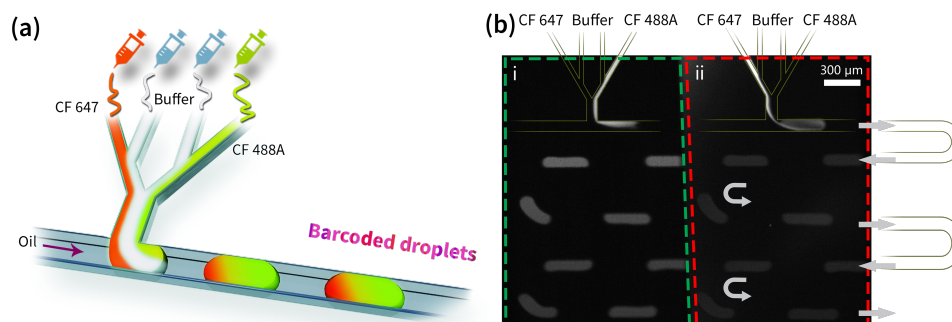


Figure 1:3 (a) Schematic of a droplet barcode generator. The inlet flows of two fluorescent dyes (CF 647 and CF 488A) are first paired with an individual buffer flow each before being joined together. These aqueous flows are generated using four syringe pumps programmed to dynamically change the ratio of flow rates, whilst ensuring that the total aqueous flow rate is constant. FC-40 is used as the continuous oil phase to shear off the aqueous stream and form isolated droplets. (b) Fluorescence image of barcoded droplets. The left half of the frame (i) records the green signal and right half (ii) records the red signal. Channels and the direction of flow are marked by lines and arrows respectively. With this method, over 500 uniquely barcoded droplets were generated in less than 20 seconds[17].

The ability to control droplet size is of obvious importance when performing quantitative experiments, however the ability to “load” droplets with multiple reagents at user defined concentrations is perhaps even more critical. Introduction of the dispersed phase through

an upstream branched inlet channel allows for the direct combination of multiple laminar streams prior to droplet formation[18], with the relative concentration of each reagent being defined by the associated volumetric flow rate ratios[19]. Notably, this strategy has been effective in creating droplet barcodes, in which co-encapsulation of multiple fluorophores spectrally encodes droplets and yields uniquely identifiable signatures[20–22]. A proof-of-concept example of such a system is shown in Figure 1:3.

The passive production of droplets is simple, quick and efficient, however, limited in its ability to independently manipulate droplets in a dynamic and bespoke manner. In this respect, active methods show clear utility in allowing the creation of user-defined droplets in a “droplet-on-demand” fashion. Common actuating sources for such purposes include pneumatic pressure[23–25], electrical fields[26], acoustic waves[27], optical traps[28] and thermal gradients[29]. For example, Rane and co-workers[30] used a pneumatic valve-based architecture to assemble combinatorial populations of enzyme-substrate droplets. Specifically, 650 unique combinations could be programmed and generated in series in a highly reproducible manner. However, it should be remembered that active methods typically produce droplets at low generation frequencies (several Hertz at best) and require the use of complex control architectures. Accordingly, the choice of droplet generation method should always be made based on the specific requirements of the experimental platform.

1.2 Unit operations

Subsequent to their generation, droplets need to be manipulated in ways that engender standard analytical procedures used on the laboratory. Fortunately, a wide range of (both passive and active) functional components have been presented for operations that include droplet merging[31–34], dilution[35, 36], dosing[37–39], splitting[40, 41], pairing[42–44], sorting[45–47], trapping/releasing[48–50] and incubation[51, 52] (Figure 1:4). An instructive example in this respect was reported by Hatch *et al.*[53], who used successive bifurcations to split single droplets into 256 daughter droplets in a rapid and passive fashion (Figure 1:5). Using such a strategy, over one million droplets (that are either empty or contain one copy of target DNA) could be generated in between 2 and 7 minutes. Droplet populations formed in this manner could be subsequently packed into on-chip storage chambers and thermally cycled for digital PCR analysis[54]. Conversely, Eastburn *et al.* reported a powerful and robust (active) method, termed “picoinjection”, which utilises a pressurized microchannel and periodic electric field to inject a controlled volume of reagent into a moving droplet[55]. Picoinjection has proved to be immensely useful in a range of

complex, droplet-based assays, being compatible with common biological reagents such as nucleic acids and enzymes.

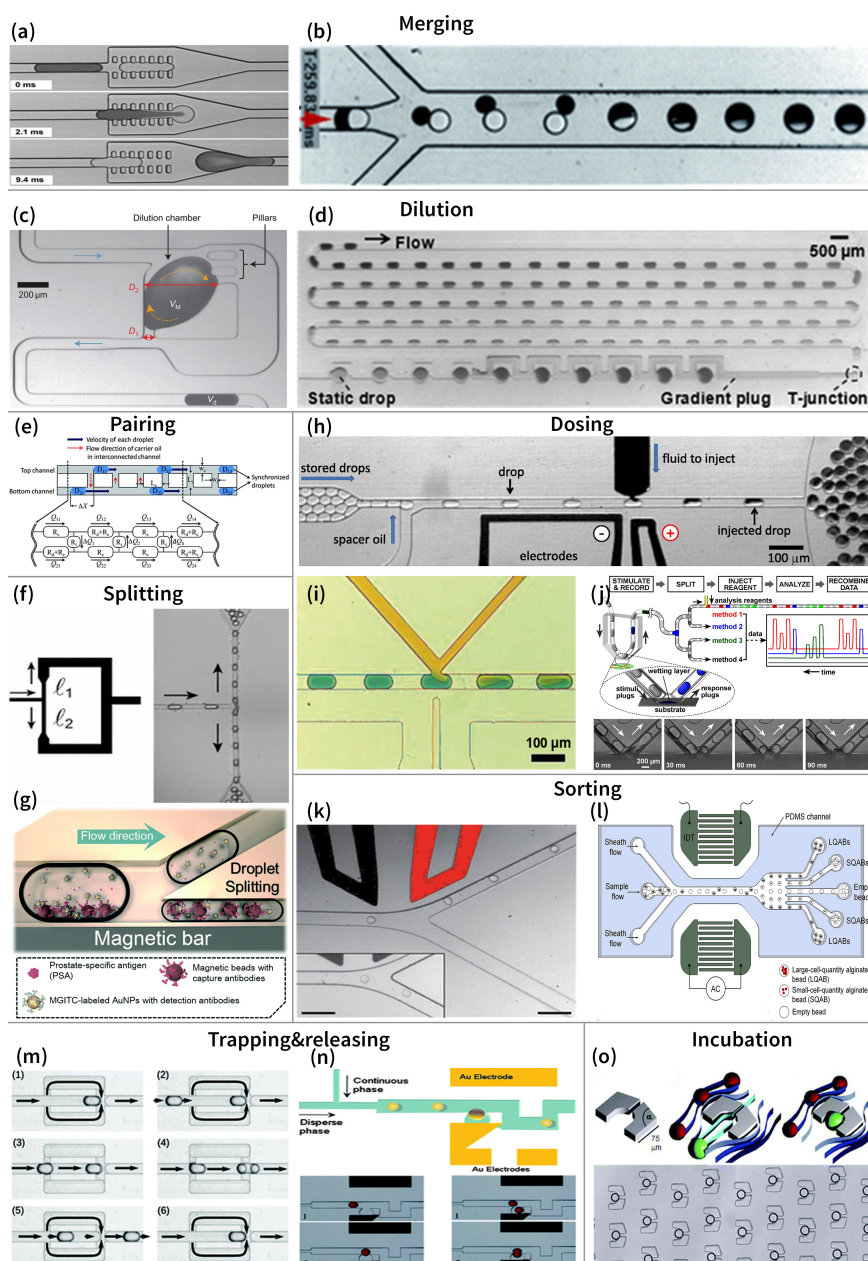


Figure 1:4 Examples of droplet unit operations. (a) Pillar-induced droplet merging[31]. (b) A selective droplet merging system[33]. (c) A microdroplet dilutor[35]. (d) Generation of concentration gradients[36]. (e) Parallel synchronization[42]. (f) Geometrically mediated droplet splitting[40]. (g) Droplet splitting used for heterogeneous phase separation[41]. (h) Electric field triggered picoinjection[37]. (i) A variant structure for injecting sample into droplets[39]. (j) Droplets extract molecules from the contact substrate[38]. (k) Fluorescence-activated droplet sorting[45]. (l) Density-dependent sorting by using the standing surface acoustic wave[46]. (m) A multifunctional droplet trap[48]. (n) On-demand droplet release[49]. (o) On-chip droplet incubation with arrays[51]. Images are adapted from corresponding references with permission.

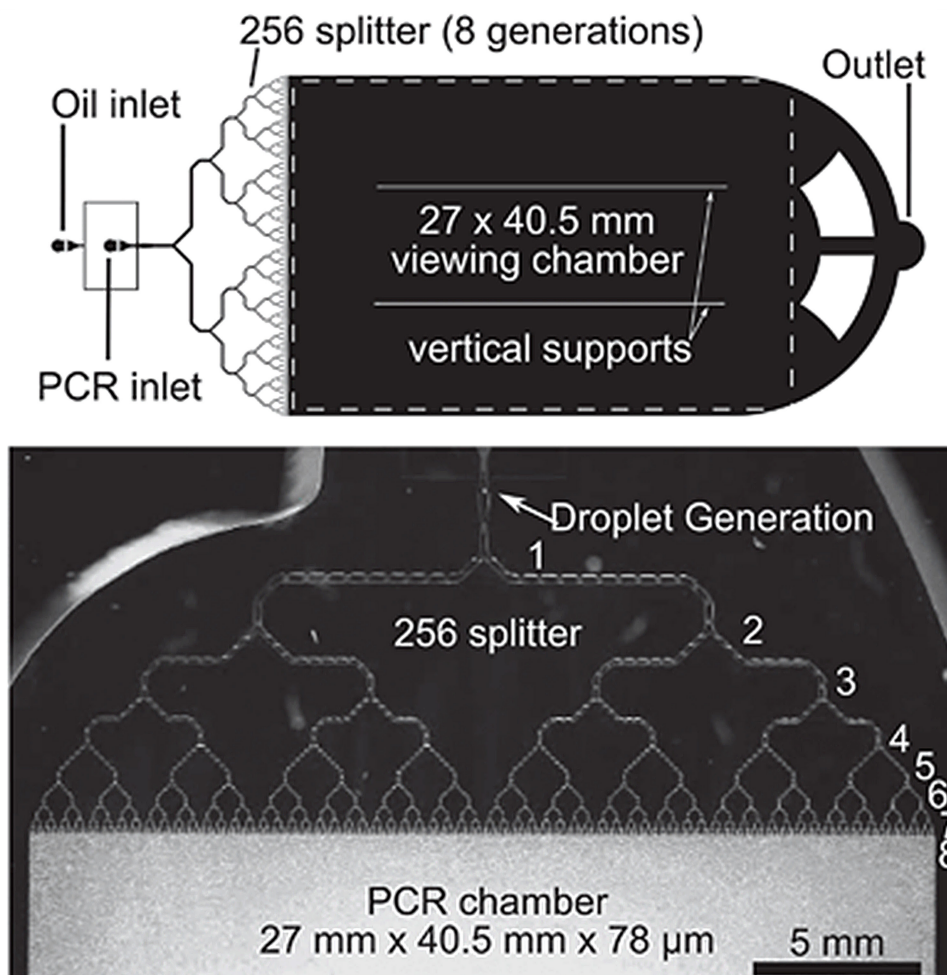


Figure 1:5 1-million droplet array for dPCR contains a single droplet generator, 256 splitters and a 27 mm × 40.5 mm viewing chamber. Adapted from reference [53] with permission.

The ability to link functional components within integrated and sequential workflows has been a key reason why droplet-based microfluidic systems have proved so advantageous in biological experimentation[56–58]. For example, complex chemical and biological assays can be performed in a rapid and efficient manner. In this respect, Lan and co-workers assembled an elaborate workflow that leverages short-read DNA sequencing to obtain long and accurate sequence reads (Figure 1:6)[59]. Central to this process was the use of unique barcodes to label long-DNA molecules, thus allowing short-reads of breakage fragments to be accurately reassembled. Functional operations within such a workflow included droplet generation, thermal cycling, splitting, pairing/merging, incubation, triple-droplet pairing/merging, splitting, pinched-flow size sorting, and secondary thermal cycling. Significantly, such an approach enables accurate sequencing of reads up to 10 kb, and opens new opportunities for the identification of rare mutations that are inaccessible to conventional sequencing.

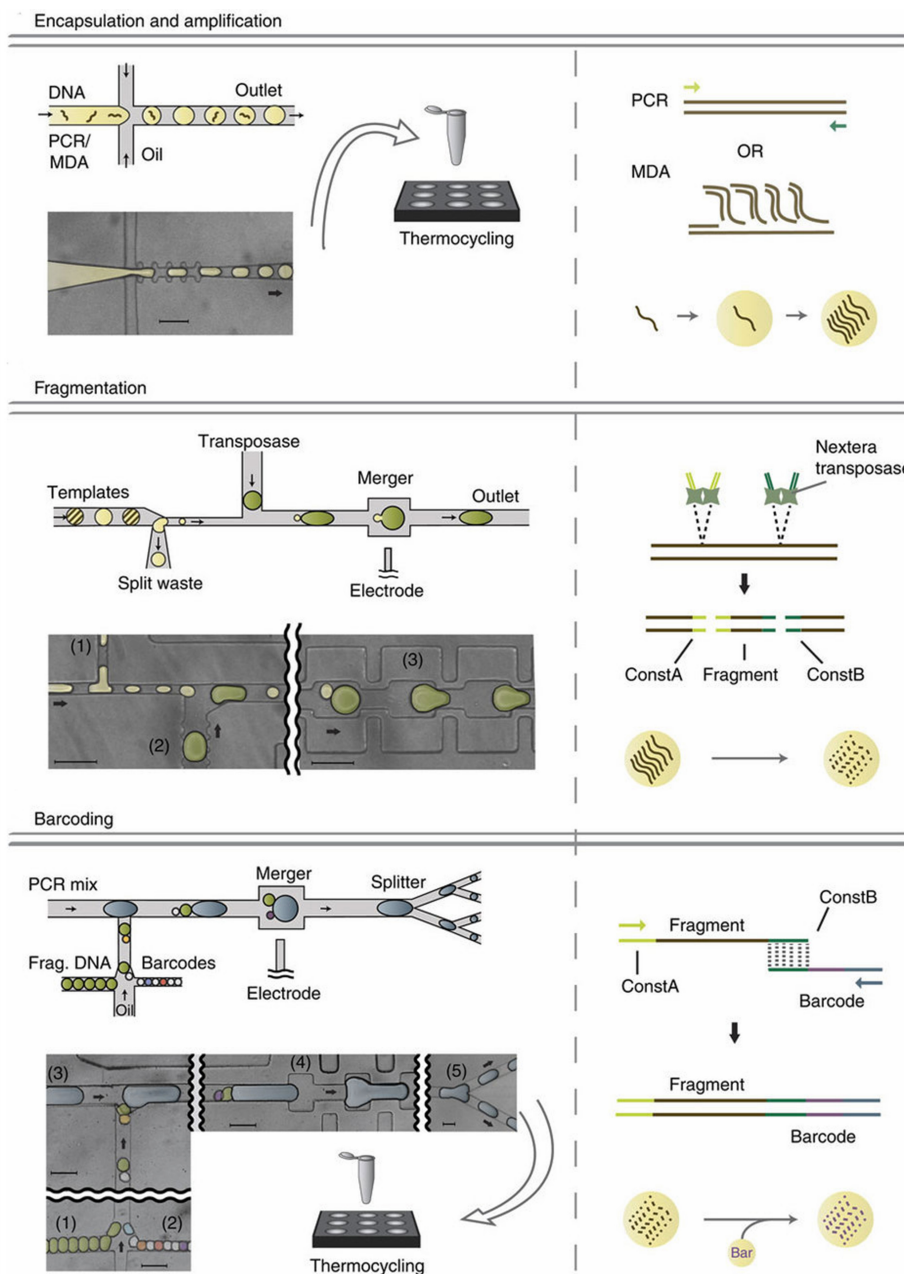


Figure 1:6 Complex microfluidic droplet workflows enable long and accurate DNA sequencing reads via barcoding short-read fragments. Left: Schematics and false-coloured images of devices. Right: Cartoons of molecular processes occurring inside droplets. *First stage* (top): Single templates are encapsulated into droplets by a flow-focusing drop maker. Inside each droplet PCR or MDA is used to amplify the single template. *Second stage* (middle): A split-merger is used to add transposases and precisely adjust template concentrations. Template droplets are injected on the left side, split at junction (1) so that 1/10th of the droplet continues to pair with a reagent droplet generated on-chip at (2), with the pair merging at the channel expansion (3). Inside droplets, the transposase reaction fragments templates and adds adaptors to each fragment. *Third stage* (bottom): The device used for attaching barcodes to DNA fragments. Template droplets (1) and barcode droplets (2) are injected into the device where they pair with each other and a large PCR reagent droplet generated on-chip (3). The three droplets merge at the electrode (4) and are split into smaller droplets for thermal cycling (5). Inside droplets, barcodes are spliced onto fragments by overlap-extension PCR. Scale bars are 100 μm . Adapted from reference [59] with permission.

1.3 Droplet stability

In most situations, it is desirable for droplets to maintain their size and composition over extended periods of time. Long-term stability of droplets is almost exclusively facilitated by the use of appropriate surfactants, which act to inhibit droplet coalescence by stabilizing the interface between the component immiscible phases. Surfactant molecules are normally mixed into the continuous phase, and upon contact with the discrete phase self-organise at the interface.

An excellent review of droplet surfactants that provides a comprehensive discussion of surfactant selection in droplet-based microfluidics can be found elsewhere[60]. However, in the current context some key issues are worthy of discussion. First, although many oils and organic solvents can be used as carrier fluids in droplet-based microfluidic systems, when performing nucleic acid analysis choices are more restricted due to biocompatibility requirements and the need to exclude biological impurities[60]. Mineral oils and perfluorinated oils (such as HFE-7500, FC-40 and FC-70) have been most frequently used in the droplet-based microfluidics. When using mineral oils, droplets can be efficiently stabilised by Span 80 (sorbitan monooleate) and Abil EM 90 (a non-ionic, silicone-based emulsifier)[61–63]. Nevertheless, due to the prevalence of fluorinated oils as carrier fluids (because of their excellent biocompatibility and high gas permeabilities), fluorosurfactants (perfluoropolyethers containing hydrophilic head groups), such as perfluoropolyether-polyethylenoxide triblock copolymers, have proved to offer exceptional long-term stabilization of droplets in a range of situations. Second, droplet size plays a critical role in emulsion stability, with the existence of thermodynamically and kinetically stable regions with respect to droplet radii[64]. Indeed, although fluorosurfactants can stabilize droplets (having diameters on the tens of microns scale) for months at room temperature[65], unless it is absolutely essential droplets should be processed and assayed on the shortest appropriate timescale. Put simply, when droplets are in close proximity for long periods of time (*e.g.* when packed in an incubation chamber) undesirable mass transfer between droplets will occur to some extent due to phenomena such as Ostwald ripening, phase partitioning, bilayer diffusion or micelle-mediated transport[66–71]. That said, controlled molecular transport between droplets can actually open up new and unexpected opportunities[72]. For example, recent studies suggest that additives (such as Bovine Serum Albumin) can decrease diffusion rates by forming barrier layers, and can also maintain high enzymatic activities (when performing droplet PCR) through competitive adsorption on surfactant layers[70, 73, 74]. It should also be noted that although mineral and fluorinated oils are both compatible with droplet PCR, their physical and chemical differences defining particular limitations and advantages.

These are compared and summarised in Table 1:1. Finally, it must not be forgotten that control of channel surface properties is critical in ensuring efficient generation and processing of droplets[75]. Although more detailed discussions of this issue can be found elsewhere[71], it should be noted that channels made from hydrophilic materials (such as glass) must be made hydrophobic through silanisation and for naturally hydrophobic surfaces (such as PDMS and PMMA) to be treated with fluoroalkylsilanes prior to experimentation[76].

Table 1:1 Comparison between mineral oils and fluorinated oils.

Property	Mineral oils	Advantages/disadvantages	Fluorinated oils	Advantages/disadvantages
Chemical formation	C-H bonds, Polarized with a certain degree of polarizability[77], Stronger intermolecular forces	Limited usage in organic droplets. Not compatible with droplets for highly sensitive fluorescent detection. Not compatible with droplet cell culture.	C-F bonds, Highly polarized but extremely low polarizability[78], Weak intermolecular forces, bringing about the availability of interstitial space[79]	Chemically inert, immiscible with many organic solvents, widely applied for organic droplets as continuous phase[79]. Significantly lower solubility for small organic molecules such as fluorescein[70]. Gases such as oxygen and carbon dioxide are permeable and highly soluble, allowing for droplet cell culture[70].
Density	Lighter than water	Droplets are under the oil layer during storage. Oil itself prevents evaporation of droplets during bulk droplet PCR in tube.	Heavier than water	Droplets are above the oil layer during storage. Need to be sealed tightly for bulk droplet PCR in tube, sometimes, a top layer of mineral oil is added for further protection.
Vapor pressure	Low	Less volatile. Compatible with on-chip droplet PCR even with PDMS (gas permeable) device[53].	High	Evaporate quickly in an open environment. Challenging for on-chip droplet PCR. The device should not be gas permeable, and it should be enclosed under high pressure.
Viscosity	High	Very likely to stick on the wall of tubes and tips. Highly possible to mix with undesired air gas bubble whilst pipetting.	Low	Comfortable to transfer droplets. Best fit for multi-step assays requiring on- and off-chip switching such as ddPCR workflow.
Capillary number ($Ca = \eta V / \gamma$, η , the viscosity of the continuous phase, V , the velocity of the continuous phase, γ , the interfacial tension between the oil and water phases)[80]	Viscosity dominates the stress for the moving droplets	A reliable manipulation of droplets primarily relies on an elegant control of the range of flow rates. Large deformations of the droplets and asymmetric shapes are easy to form through fluid dynamics[80]. Over flow rates lead to droplet failure modes: beading, splitting and satellite droplets[71].	Interfacial tension dominates the stress for the moving droplets	A reliable manipulation of droplets mainly relies on an efficient surfactant formulation and concentration[70]. Droplet surface area is nearly minimized by producing spherical ends[80]. Easy to perform ultra-high-throughput experiments in terms of generation rate and transportation speed.

1.4 Particle encapsulation and Poisson statistics

The encapsulation of functional particles (here the term “functional particles” refers to small pieces of matter such as cells, bacteria, beads, enzyme and DNA) is a significant task in droplet-based microfluidics. The idea behind this strategy is to partition such particles within the compartments formed by nano-/picoliter droplets, so that a large number of biochemical assays (*e.g.* single cell screening, molecule capture and enzymatic reactions) at small scales can be accessed independently and in a highly parallel fashion. Particles are usually loaded into droplets together with the aqueous phase. Such a loading process is passive in nature, being simple and rapid in operation. Although the ability to control the number of particles loaded, in a droplet-by-droplet fashion, is challenging if not impossible, population behaviour can still be assessed through statistical analysis. Random passive encapsulation of particles will obey Poisson statistics[81], since loading occurs at a known average rate and independently of the time since the last event. For example, the probability that a droplet will contain n particles is given by:

$$P_n(N) = \frac{N^n \exp(-N)}{n!} \quad (1:1)$$

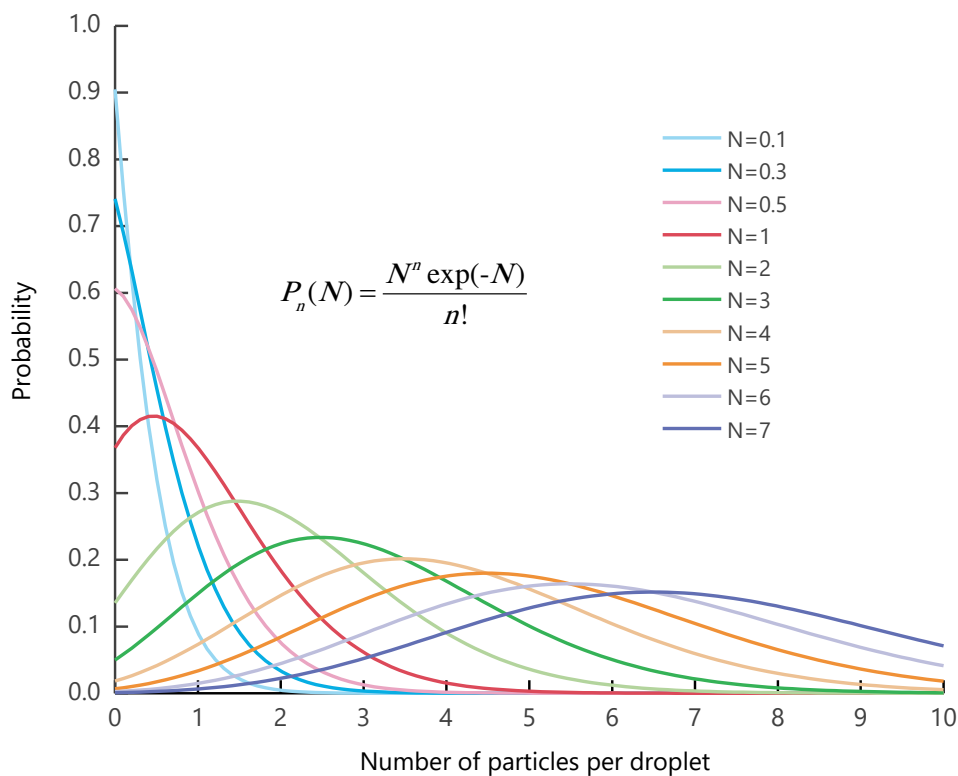


Figure 1:7 Probability distribution functions for the number of particles per droplet according to Poisson statistics. Curves are plots for N equal to 0.1, 0.3, 0.5, 1, 2, 3, 4, 5, 6 and 7 respectively.

Where N is the average number of particles per droplet. Equation (1:1) is plotted in Figure 1:7, and quantified in Table 1:2 for N values between 0.1 and 7. Inspection of Table 1:2 highlights some important features. First, to achieve single particle encapsulation, whilst avoiding droplet containing multiple particles (*i.e.* $1 - [P_0(N) + P_1(N)] < 0.5\%$) the input suspension should be diluted so that N is less than 0.1. Under these conditions, approximately 90.5% droplets will be empty, with 9% containing a single particle. Second, when $N = 1$, the proportion of droplets containing a single particle reaches a maximum (~36.8%). Finally, when N is larger than 4, empty droplets account for less than 1.8% of all droplets.

Table 1:2 Probability values for N (average particle number per droplet) between 0.1 and 7 under Poisson conditions. The characteristic values discussed in main text are highlighted.

N	$P_0(N)$	$P_1(N)$	$P_2(N)$	$P_3(N)$	$P_4(N)$	$P_5(N)$	$P_6(N)$	$P_7(N)$	$P_8(N)$	$P_9(N)$	$P_{10}(N)$	$1 - P_0(N)$	$P_0(N) + P_1(N)$
0.1	0.905	0.090	0.005	0.000	0.000	0.000	0.000	0.000	0.000	0.000	0.000	0.095	0.995
0.3	0.741	0.222	0.033	0.003	0.000	0.000	0.000	0.000	0.000	0.000	0.000	0.259	0.963
0.5	0.607	0.303	0.076	0.013	0.002	0.000	0.000	0.000	0.000	0.000	0.000	0.393	0.910
1	0.368	0.368	0.184	0.061	0.015	0.003	0.001	0.000	0.000	0.000	0.000	0.632	0.736
2	0.135	0.271	0.271	0.180	0.090	0.036	0.012	0.003	0.001	0.000	0.000	0.865	0.406
3	0.050	0.149	0.224	0.224	0.168	0.101	0.050	0.022	0.008	0.003	0.001	0.950	0.199
4	0.018	0.073	0.147	0.195	0.195	0.156	0.104	0.060	0.030	0.013	0.005	0.982	0.092
5	0.007	0.034	0.084	0.140	0.175	0.175	0.146	0.104	0.065	0.036	0.018	0.993	0.040
6	0.002	0.015	0.045	0.089	0.134	0.161	0.161	0.138	0.103	0.069	0.041	0.998	0.017
7	0.001	0.006	0.022	0.052	0.091	0.128	0.149	0.149	0.130	0.101	0.071	0.999	0.007

In practice, conformance to Poisson statistics means that desired encapsulation properties are achieved through appropriate control of droplet size and input particle concentration. Additionally, this description can be used to evaluate encapsulation data after a given experiment. A good example of this is in the analysis of digital droplet PCR (ddPCR) data. ddPCR is an absolute quantification technique widely used in DNA analysis². Put simply, ddPCR encapsulates single DNA templates into thousands of discrete nanoliter droplets.

² A survey of the applications of ddPCR will be provided in Chapter 4.

Subsequent to PCR amplification, the number of templates is quantified through the number of “positive” droplets, detected using a fluorescent probe. Typically, ddPCR involves processing of a dilute DNA sample where That said, the direct use of the number of positive droplets will underestimate the amount of template DNA, since there exists a small probability that some events are associated with multiple DNA template molecules within a droplet. In such a situation, the template count can be corrected with a confidence interval > 95%[82]. The correction, most normally, uses the following formula:

$$N = -\ln(1 - P) \quad (1:2)$$

Here P is the fraction of positive droplets measured experimentally and N is the corrected average number of DNA templates per droplet. This relationship is shown graphically in Figure 1:8, whilst Figure 1:9 shows four situations (in ddPCR) corresponding to different sample densities[82].

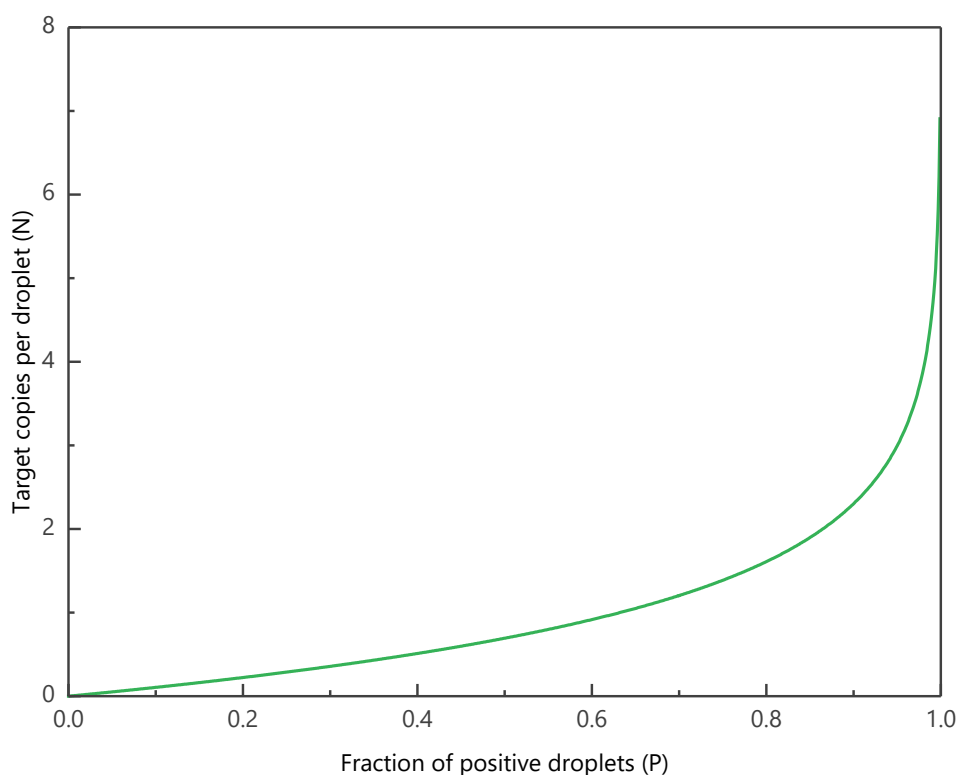


Figure 1:8 Variation of target copies per droplet as a function of the fraction of positive droplets in ddPCR. This curve can be directly used to correct ddPCR data. Adapted from reference [82] with permission.

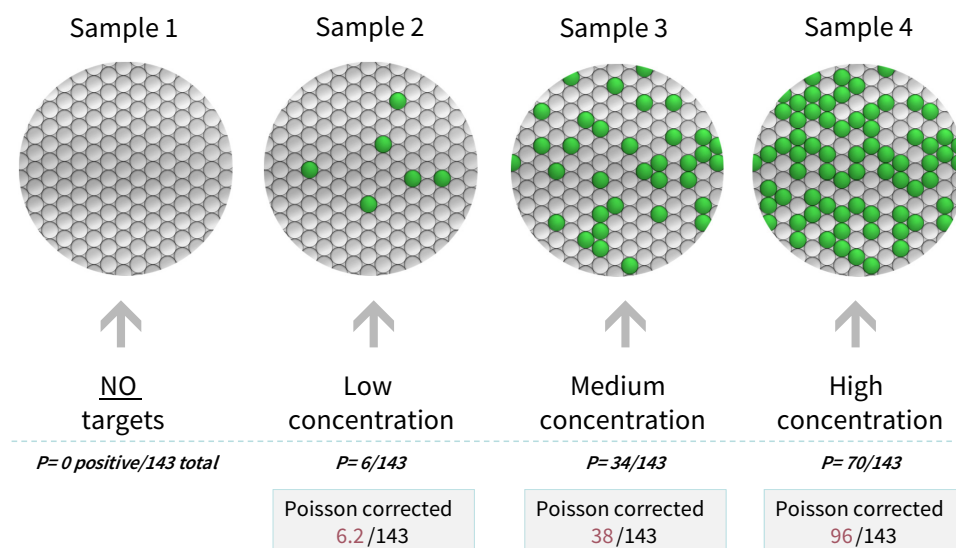


Figure 1:9 The number of positive droplets is directly related to the concentration of target in the sample. Adapted from reference [82] with permission.

Put simply, adherence to Poisson statistics is fundamental to understanding and performing the encapsulation of functional particles within droplet-based microfluidic systems. Indeed, this scenario has been used to guide a number of important experiments described in Chapter 3 and Chapter 5.

1.5 Conclusions

This chapter has introduced some of the most important aspects of droplet-based microfluidics with respect to their application in chemical and biological experimentation. Specifically, some of the most interesting functional tools for droplet formation, reagent encapsulation and manipulation have been described, and issues relating to droplet stability summarised. Unsurprisingly, recent years have witnessed a startling increase in the use of droplet-based microfluidics in a wide variety of chemical and biological assays because of the simple fact that physical processes can be more easily controlled and harnessed when analytical volumes are reduced to the pL-scale.

That said, although a large number of methods for droplet formation and manipulation have been presented in the literature, there is still a significant need for novel methods that exert enhanced control over droplet properties, such as size, payload and location. To this end, studies presented in Chapter 2 and Chapter 3 are aimed at the development of novel microfluidic architectures that allow bespoke-droplet generation and manipulations, with

Chapter 4 presenting a discussion of key applications of droplet-based microfluidics in the biological sciences. Subsequently, integration of functional microfluidic components is used to define and develop a novel analytical platform for high-throughput profiling of antigen-specific T cell receptors at the single cell level. Results of these proof-of-principle studies are provided in Chapter 5.

Chapter 2 The “V-junction”: a novel structure for high-speed generation of bespoke droplet flows^ψ

This chapter presents the use of microfluidic “V-junctions” as a droplet generation tools. V-junctions incorporate enhanced performance characteristics when compared to more traditional “T-junction” formats, including the ability to generate target-sized droplets from the very first one, efficient switching between multiple input samples, the production of a wide range of droplet sizes (and size gradients) and the facile generation of droplets with residence time gradients. Additionally, the use of V-junction droplet generators enables the suspension and subsequent resumption of droplet flows at times defined by the user. The high degree of operational flexibility allows a wide range of droplet sizes, payloads, spacings and generation frequencies to be obtained, which in turn provides for an enhanced design space for droplet-based experimentation. Results show that the V-junction retains the simplicity of operation normally associated with T-junction formats, whilst offering functionalities traditionally associated with droplet-on-demand technologies.

2.1 Introduction

Microfluidic technologies have engendered many new and exciting opportunities within the chemical and biological sciences. They provide for high analytical efficiency and through-

^ψ This chapter was published in part in: Yun Ding, Xavier Casadevall i Solvas, and Andrew deMello, ‘V-Junction’: A Novel Structure for High-Speed Generation of Bespoke Droplet Flows, *Analyst* 140, 414 (doi:10.1039/C4AN01730G).

put, and harness the dependency of fluid-flow on scale to empower new experimental formats (such as digital PCR and single cell-based screens)[83–85]. These features are made possible due to reduced sample and reagent consumption, efficient mass and thermal transport (due to smaller volumes) and an exquisite ability to integrate a range of functional components within a monolithic format[86–89]. In recent years, droplet-based (or segmented-flow) microfluidic systems have been used to great effect when performing high-throughput and high-efficiency chemical and biological assays. Sub-nanoliter droplets may be generated at high speeds (kHz rates), with their size and chemical payloads being controlled in a reproducible manner. Each droplet acts as an individual compartment that isolates and protects its contents from microchannel surfaces and cross-contamination between adjacent samples[90, 91]. Almost 15 years has passed since Thorsen *et al.*[9] and Anna *et al.*[10] first demonstrated highly monodisperse droplet formation using either T-junctions or flow focusing geometries, and during this time a diversity of functional components have been developed to process such droplet flows. These include elegant tools for droplet immobilization, mixing, incubation, dosing, merging, splitting, diluting and sorting[31, 35, 51, 53, 92–95]. Accordingly, droplet-based microfluidic platforms have been enthusiastically adopted as powerful research tools in many chemical and biological laboratories. As such, an increasing number of non-expert researchers are becoming interested in using microfluidic technologies to address specific chemical or biological problems, but are often reluctant to fully embrace them due to their complexity and high instrumental investment threshold. Therefore, direct strategies that require only simple equipment are highly desirable. For example, and in an ideal world, an experimental process could be “hardcoded” into a microfluidic device through geometric design and control of the physicochemical properties, such as hydrodynamic resistances, surface properties and the diffusion, solubility and chemical activity of the contained reagents[32, 43, 94, 96, 97]. In such a situation, the user would simply introduce the desired sample, with the experiment then “running itself”.

Although numerous functions and droplet manipulations have been achieved through the use of passive microfluidic systems, there remain some key challenges that must be addressed prior to the realization of autonomous operation. Of special relevance is adoption of a droplet generation strategy that guarantees stable production of droplets of desired size, frequency and spacing. Although formats for droplet generation are well known, formation of bubbles at the beginning of an experiment or droplet generation at inconvenient times (such as during the initial unsteady transitory phases[95] or when asynchronous trains of droplets are produced)[32] are often terminal for experiment progress. Currently, there

exists no strategy that allows for passive droplet generation, whilst eliminating or preventing the formation of rogue droplets or bubbles. Conventional droplet generators, based on T-junctions and flow focusing geometries, benefit from operational simplicity but suffer from the above problems, thus impacting experimental reproducibility[98, 99]. To date, these issues have been resolved by adopting droplet-on-demand technologies[25, 100, 101], which commonly involve the use of elaborate microvalves or mechanical actuators to allow control of the droplet generation process. These methods typically require complex fabrication procedures and necessitate development of custom actuation and control algorithms. In this respect, it should also be noted that droplet-on-demand operation has been realized through the adoption of complex, off-chip robotic solutions[102].

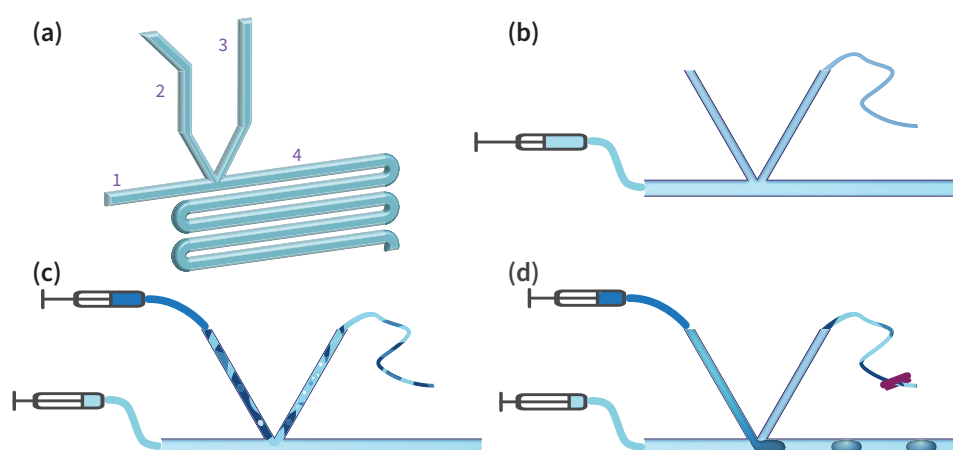


Figure 2:1 (a) Schematic of the V-junction structure containing an oil inlet 1, side channel 2 for water introduction, side channel 3 for control, and a main channel and observation zone 4. In the current design, all channels are $50\ \mu\text{m}$ in height. The angle between the two side channels is 60° . (b-d) Schematic illustration of chip operation. (b) A 30 cm long control-tubing connected at the end of channel 3, all the system is filled with oil. (c) Open-mode: with oil continuously being infused, the water phase begins to enter channel 2. Air bubbles, transitional emulsions and water are drained through channel 3. (d) Closed-mode: once impurities have been completely removed, the control-tubing is blocked and water enters the main channel forming stable droplets.

Herein, we present a modification of the traditional T-junction design, which we term a V-junction (Figure 2:1a). The V-junction allows the generation of controllable droplet streams (from the first to the last) and requires only basic fabrication and manipulation techniques. By simply incorporating an additional side (or control) channel (Figure 2:1a-3) at the T-junction, generation of droplets is easily achieved and accompanied by several attractive features. These include the prevention of unwanted droplets, clean switching between multiple input samples, production of a large range of droplet sizes (and size gradients) and generation of droplets streams with residence time gradients. It is important to note that a structurally similar design (termed a K-junction) has recently been introduced by Lin and

co-workers[103]. This was used for the on-demand generation of cell encapsulating droplets using the assistance of an integrated pneumatic micropump. In comparison, we report for the first time a passive droplet generation system that fills in the gap between high-end (but complex) droplet-on-demand systems and passive (but utility-limited) droplet generation methods.

2.2 Materials and Methods

Polydimethylsiloxane (PDMS) devices were fabricated using SU-8 master moulds and standard soft-lithographic methods[104]. After degassing and casting over an SU-8 master, PDMS (Sylgard 184, Dow Corning, USA) was oven-cured at 70°C for 2 hours. The structured PDMS layer was then peeled off the master and sealed onto a flat (unstructured) PDMS layer by plasma bonding. Subsequently, the chip was kept overnight at 70°C to firm the bond and to allow channel walls to recover their inherent hydrophobic surface properties[105]. During droplet-generation experiments the entire microfluidic device was held on a glass slide (Thermo Scientific, Germany) and imaged under a microscope (Eclipse Ti-E, Nikon, Japan) using a high-speed camera (MotionPro Y5, IDT, UK). Figure 2:1a illustrates the basic microfluidic structure, with all channels being 50 μm high. The main channel used to infuse the carrier phase (typically oil) and generate the segmented flow has a width of 100 μm . Side channels for discrete phase (typically water) infusion and droplet control (labelled 2 and 3, respectively) are divided in two segments: the top section being 100 μm wide and the lower section, being 50 μm wide. The angle between the side channels is 60°, with the bisector perpendicular to the main channel. It should be noted that three sets of devices, with 30°, 60° and 90° angles, were designed and tested (FigureS 1). It was observed that a 60° angle provided for the best control capability.

Mineral oil (Sigma-Aldrich, light oil form, 0.84 g/ml, UK) and deionized water (containing blue ink in some experiments) were used to create droplet streams. 5 wt% Span 80 (Sigma-Aldrich, UK) was added as a surfactant into mineral oil to stabilize droplets after formation. The oil-surfactant mixture was vortexed and degassed before use and syringe pumps (neMESYS Low Pressure Dosing Module, Cetoni, Germany) used to inject oil and water phases into the microchannels.

Unless otherwise indicated, droplet analysis was accomplished with using ImageJ (v1.47, NIH, Bethesda, Maryland, USA) and Droplet Morphometry and Velocimetry software (DMV)[106].

2.3 Results and Discussion

2.3.1 Binary mode: a world-to-chip interface that prevents unsolicited droplet introduction

The initial capabilities of the V-junction are first presented by applying two operational modes on the control channel: ‘open’ or ‘closed’. These modes allow the dispersed phase (water in the current experiments) to either enter the main channel (open-mode) or the control channel (closed-mode). Figure 2:1 illustrates a schematic of the set up for each mode of operation. It is noted that a length (30 cm) of soft tubing (TYGON ND 100-80 Tubing, ID 0.020 inches, OD 0.040 inches, USA) is connected to the exit of the control channel. Before starting an experiment (Figure 2:1b), only the oil inlet (1) and control channel (3) are connected to the tubing. The device is first primed by pumping oil throughout the whole system, including the control-tubing. This step ensures that residual air (which is compressible) in the control-tubing is removed, and also aids in building a pressure balance during the initial state. Whilst oil is continuously pumped at the desired flow rate, the water inlet is then connected to the tubing to allow infusion of water into the system. During open-mode operation, all the fluid from the water inlet is directly eliminated through the control channel, including transitional air bubbles, oil, water and transient droplets. For the current device and an oil influx of $2 \mu\text{l}/\text{min}$, the volumetric flow rate of water is maintained below $6 \mu\text{l}/\text{min}$ (although operation is still successful for flow rates as high as $11 \mu\text{l}/\text{min}$, FigureS 3). Switching to closed-mode is simply achieved by closing the tubing of the control channel. As soon as the flow in the control channel stops, water enters the main channel and droplets are generated. Thereupon, the system functions as a T-junction (with improvements that will be discussed in the next section).

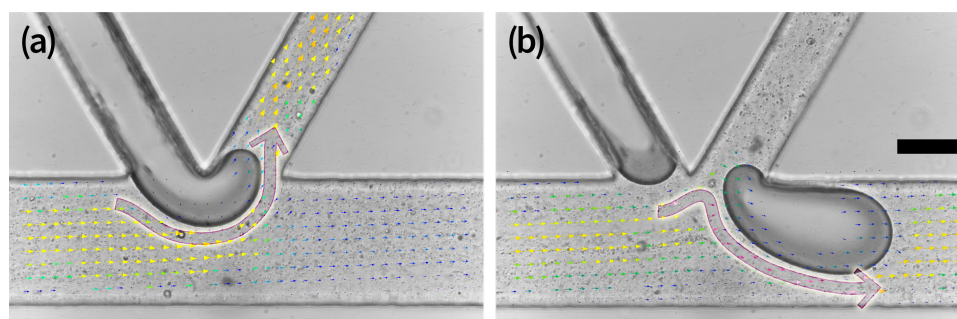


Figure 2:2 PIV analysis of two basic operation modes. The speed and direction of oil flow are indicated with arrows. (a) In open-mode, the oil flow goes into both the main channel and the side channel. A barrier flow by oil (marked with a hollow pink arrow) prevents the water phase from entering the main channel. (b) In closed-mode, no net flow occurs in the control channel. The water phase creates droplets at the main channel by shearing in the oil flow. Video for both cases is provided in the Appendix D.1, VideoS 2. The scale bar is $50 \mu\text{m}$.

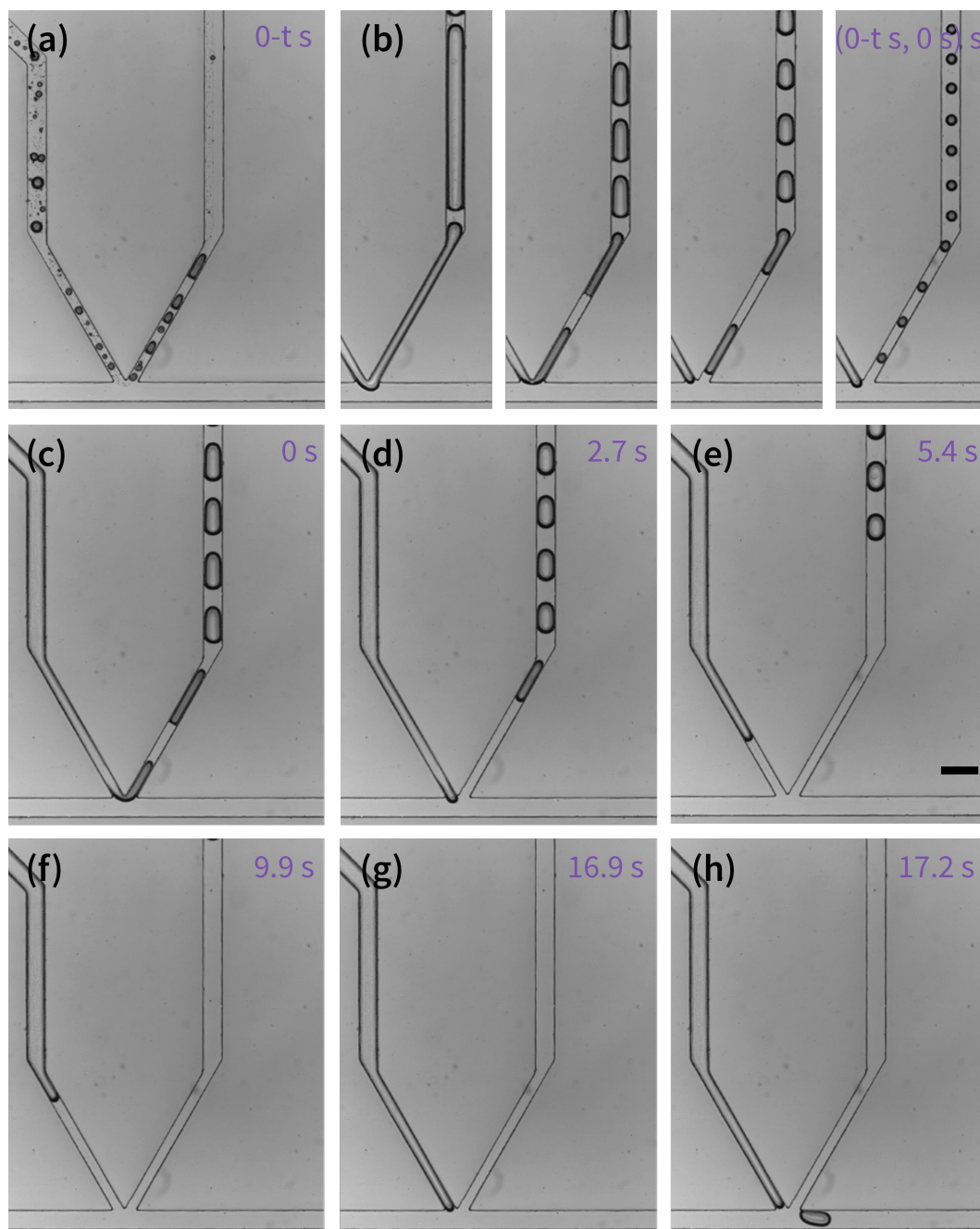


Figure 2:3 Sequence of steps used to create stable water droplets from the first one. (a-c) Open-mode. (a) The initial chaotic mixture of phases is eliminated. (b) Adjusting the water flow rate leads to the desired droplet size at (h). (c) When the system has stabilized droplets are generated in the control channel. (d-h) Switch to closed-mode. (d-g) The water phase stops, recedes and moves forward. (h) The first droplet in main channel is generated. Subsequent droplets can be seen in VideoS 3. The scale bar is 200 μm .

To better understand the transition between open and closed modes, profiles of the oil flow for both modes of operation were visualized using Particle Image Velocimetry (PIV)[107], by seeding a small number (0.1 wt%) of polystyrene microspheres (5 μm diameter in aqueous suspension) into the oil phase. The results of the PIV analysis are shown

in Figure 2:2 and VideoS 2. In open-mode (Figure 2:2a), the hydraulic resistances at the main channel side and at the control channel side are comparable. Accordingly, the continuous oil phase will flow into both channels. Under these conditions, the discrete water phase requires additional kinetic energy to break the oil ‘barrier’ (marked with a hollow pink arrow) and penetrate the main channel. Therefore, water flows into the control channel and is carried away by the continuous oil phase. In closed-mode operation (Figure 2:2b), the resistance of the control channel suddenly becomes infinitely higher than the main channel. Hence, there is no net flow through the control channel and the incoming water and oil phases are forced to enter the main channel. A more detailed analysis of the force balances at the interface is provided elsewhere[103].

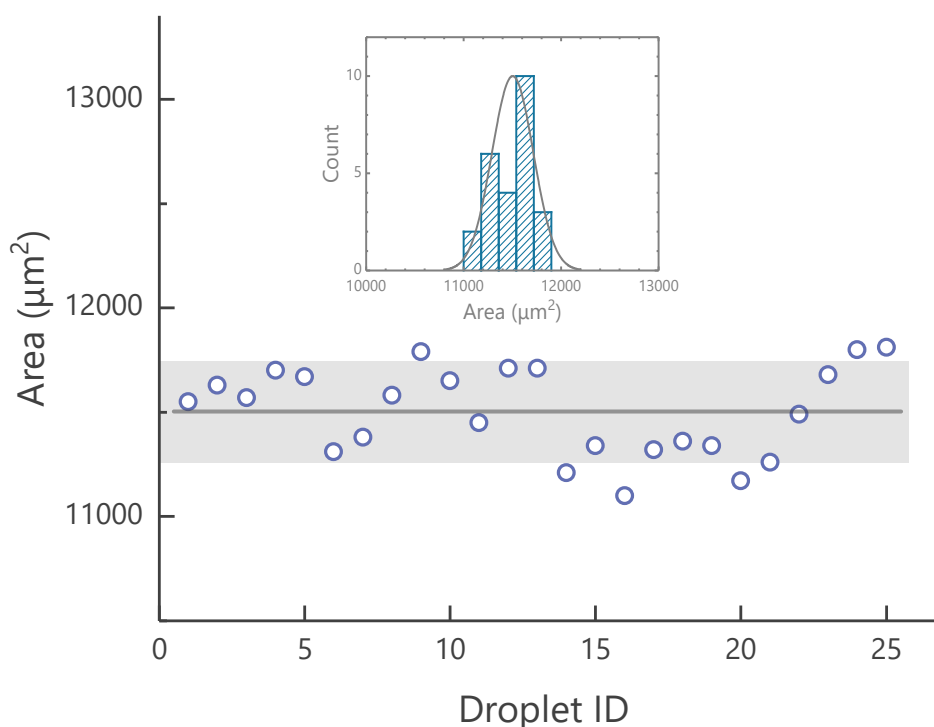


Figure 2:4 Measurement of droplet areas for the first 25 droplets (area standard deviation = 1.8%).

By utilising this simple control mechanism only stable droplets of a given size (from the very first one) can be motivated into the main channel of the chip (where the experiment of interest has been hardcoded). The operational method is outlined in Figure 2:3 (and VideoS 3). In open-mode, initial impurities (most normally a chaotic mixture of different phases) can be fully eliminated through the control channel (Figure 2:3b and c). When the stable, water stream is introduced, it is sheared by the oil flux at the junction and forms a regular droplet stream that is expelled through the control channel. The desired size of “future” droplets can then be set by simply adjusting the water flow rate without inducing contamination (Figure 2:3b to e). Triggering the closed-mode results in the water stream

receding into the inlet channel and the termination of droplet production (Figure 2:3e and f). The water steam then moves forward again and is sheared by oil in the main channel, creating stable droplets of the desired size. Figure 2:4 illustrates the high level of monodispersity of the droplets generated by this method (with an area standard deviation of 1.8%).

Water stream recession into the water inlet is caused by a certain degree of elasticity inherent to the microfluidic system (due to the use of an elastomeric chip and flexible tubing), which in turn causes a temporal pressure fluctuation. However, as evidenced by the high degree of monodispersity of the formed droplets, this transient instability does not affect droplet production. Pressure-based instabilities can be conveniently analysed and harnessed by equivalent electrical circuit theory[108]. Two analogous electronic circuits corresponding to the microfluidic networks in the two operational modes are presented in Figure 2:5. With analogy to Ohm's law for electrical circuits, the Hagen-Poiseuille law describes the pressure drop in pressure-driven fluid channels at steady state, and can be simplified as,

$$\Delta P = QR \quad (2:1)$$

here P is the pressure, Q is the volumetric flow rate and R is the hydraulic resistance. Assuming that oil and water are both incompressible (Newtonian) fluids, pressure fluctuations can trigger temporal changes in the channel (and tubing) volumes due to their elasticity. This short-lived transitional behaviour can be treated as an equivalent electric capacitance, *i.e.*

$$Q_t = C \frac{d\Delta P}{dt} \quad (2:2)$$

where C is the hydrodynamic capacitance and Q_t is the transitional flow rate. The formal positive directions of Q are marked with arrows in Figure 2:5a, where a positive value of Q means that flow follows the arrow. In open-mode (Figure 2:5a), after the system has reached equilibrium, the pressure at the junction, P_j , is equal to P_4 , *i.e.*

$$P_j = P_4 \quad (2:3)$$

$$P_4 = P_o + Q_4 R_4 \quad (2:4)$$

where P_o is the pressure at the outlet of the main channel (*i.e.* atmospheric pressure). Furthermore

$$P_j = P_2 \quad (2:5)$$

$$Q_1 + Q_2 = Q_3 + Q_4 \quad (2:6)$$

and using the observation that all the water flow (plus some oil) is taken into the control channel

$$Q_2 < Q_3 \quad (2:7)$$

Shortly after closing the control channel (closed-mode, Figure 2:5b), all the oil immediately flows through the main channel. Along the main channel (from the oil inlet to the outlet) and for the different channels close to the junction a transient steady state is reached, and it can be assumed that the pressure is constant. Accordingly,

$$P'_j = P'_4 \quad (2:8)$$

$$P'_4 = P_o + Q'_4 R_4 \quad (2:9)$$

$$Q'_4 = Q_1 \quad (2:10)$$

$$P'_2 = P_2 \quad (2:11)$$

Combination of equations (2:3)–(2:11), leads to

$$P'_j - P'_2 = (Q_3 - Q_2)R_4 > 0 \quad (2:12)$$

which indicates that an increase in pressure at the junction due to control channel closure upsets the local pressure balance, and leads to a temporary recessive flow into the water channel (coupled with a channel/tubing expansion).

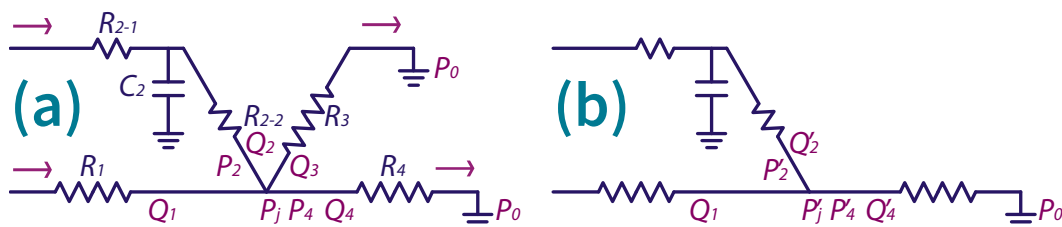


Figure 2:5 Electrical equivalent circuit models for the two modes. (a) Open-mode. (b) Closed-mode.

By switching between these two modes the device can achieve a 'droplet-on-demand'-like operation (although the exact number of droplets produced is not selected). This function can be extended further to enable clean switching of multiple samples (Figure 2:6). To

begin with, and by using the protocol discussed above, droplets containing the first aqueous sample are precisely delivered into the main channel (Figure 2:6a-d). To form droplets containing a second sample, the system is reset to open-mode (by removing the clip from the tubing). Droplets of the first sample are then eliminated through the control channel (not shown). Subsequently, the world-to-chip interface for the first sample can be disconnected whilst maintaining the flow of oil that keeps the main channel isolated (Figure 2:6e). Next, the world-to-chip interface of the second sample can be connected. Infusion of the second sample is then initiated until, after impurities from the previous sample have been eliminated (Figure 2:6f), stable droplets are produced again in the control channel (Figure 2:6g). At this point, the system can be switched to closed-mode and stable droplets of the second sample of the desired volume are delivered into the main channel (Figure 2:6h). A key feature of this simple strategy is that during the whole process not a single unsolicited droplet or contaminant pollutes the main channel. Furthermore, the procedure does not require any special skills or equipment to function.

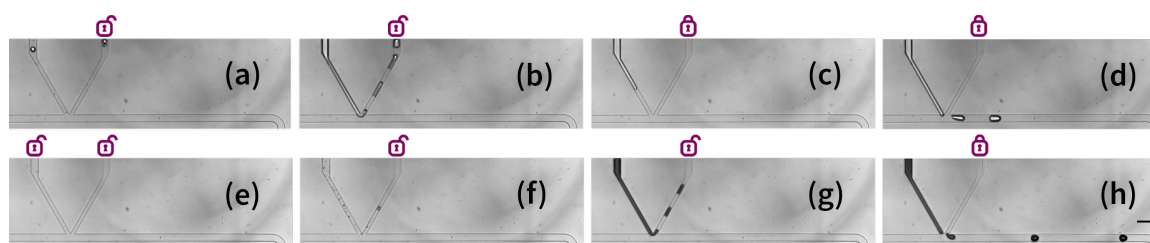


Figure 2:6 Images showing clean sample switching. (a-d) Water droplets are generated by the method illustrated in Figure 2:3. (e) By opening the control-tubing and removing the water input tubing, oil refills the entire chip. (f) Connection of the ink input tubing. Initial unwanted impurities are removed until ink droplets are generated in the control channel (g). (h) Closure of the control tubing causes stable ink droplet generation in the main channel. The scale bar is 200 μm .

2.3.2 A universal droplet generator with a magic knife

The ability to precisely control the size of the droplets is a key feature of microfluidic emulsion generation. Certain droplet operations are only possible for a limited range of droplet sizes, spacings and frequencies, and especially important for passive droplet manipulations such as fusion[31, 109], dilution[35, 48], synchronization[42], and trapping[51, 97, 110]. Furthermore, droplet size is an essential parameter in applications such as bubble logic[108, 111], microgel particle synthesis[95, 112], and studies at the single molecule level (where femtoliter or sub-femtoliter droplets are attractive assaying platforms)[8, 113].

With the addition of simple control strategies (such as connecting the control channel to another pump in “withdraw” mode) highly tuneable and precise droplet volumes can be

obtained. In the current system, the sharp corner between the control and main channels provides a “knife-like” structure that “cuts” forming droplets and splits them between the two channels. Such a splitting process can be controlled by adjustment of the pressure in the control channel. In essence, the system can behave as an asymmetric, tuneable droplet splitter.[114] To demonstrate the additional functionalities of this system, a sequence of droplets with a size gradient was created (Figure 2:7a and b) by linearly increasing suction on the control channel whilst keeping the flow rates of oil and water flows constant (at $2 \mu\text{l}/\text{min}$ and $1 \mu\text{l}/\text{min}$, respectively). Although it is possible to produce droplets with size gradients at a conventional T-junction by varying the flow of the discrete phase (see Appendix A.3.1), a much larger range of size gradients is attainable using the V-junction. Specifically, in the current system, the maximum/minimum volume ratio using the V-junction is above 100 whilst in the T-junction experiment this ratio is less than 2.

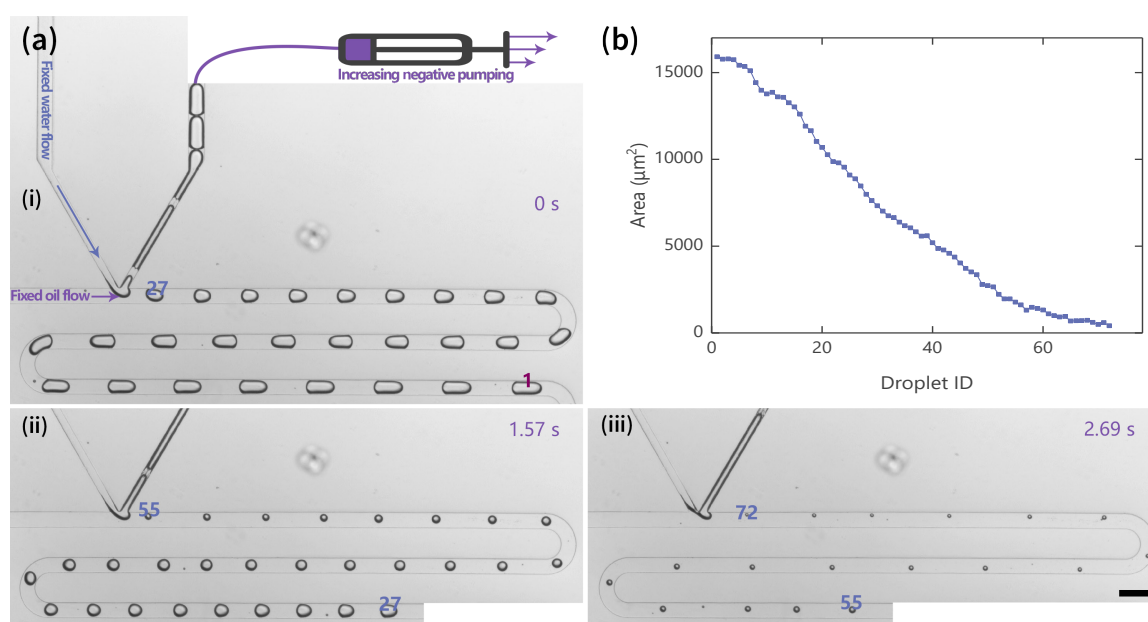


Figure 2:7 (a) A droplet size gradient generated by linearly increasing suction at the control channel. Images (ai) to (aiii) display the full sequence of droplet formation (consisting of 72 droplets). Numbers on droplets indicate droplet ID. The scale bar is $200 \mu\text{m}$. Small ‘satellite’ droplets in the pictures originate from oil impurities (see VideoS 4). (b) The area of the droplets for (a) is plotted, with the largest $15910 \mu\text{m}^2$ ($\sim 900 \text{ pl}$ in volume) and the smallest $416 \mu\text{m}^2$ ($\sim 8 \text{ pl}$ in volume).

Another key attribute of our system is its operational flexibility. When producing droplets using T-junction geometries, the parameters that define the droplet generation process (size, spacing and frequency) are intimately related, *i.e.* it is not possible to modify one without altering another in some way. For example, to produce the smallest possible droplets ($65 \mu\text{m}$ diameter) in a T-junction of comparable dimensions to the current V-junction, the water flow rate (with an oil flow rate of $2 \mu\text{l}/\text{min}$) is decreased to $0.05 \mu\text{l}/\text{min}$. Under

these conditions, lower frequencies and larger spacings result, which is not the case when using the V-junction (see FigureS 7). This is primarily due to the different droplet formation mechanisms that apply to each system. In addition to the capillary number (which determines droplet size for the T-junction)[115], the size of droplets at the V-junction is dominated by the splitting effect. A comparison of the relationship between droplet size and generation frequency for an oil flow rate of $2 \mu\text{l}/\text{min}$ is provided in Figure 2:8 (and TableS 3). Besides the evident capacity of the V-junction to generate smaller droplets, the generation frequency is also independent of droplet size. Detailed measurements and a discussion of the relationship between spacing and size are provided in the Appendix A.3.2. Due to these unique properties, the V-junction can become a convenient tool for the study of droplet traffic in microfluidic networks[116], and is likely to accelerate the design of complex networks[108]. A simple example is shown in Figure 2:9. Here, four size series of droplets are generated at a V-junction and then passed through a channel network. Those four droplet populations are controlled in a close frequency and space with the only variable of size. Thus, the occurred splitting effect and (or) path selection at a fork are only determined by the sizes. It is intuitive to observe and easy to perform quantitatively analysis for a design of fluidic network.

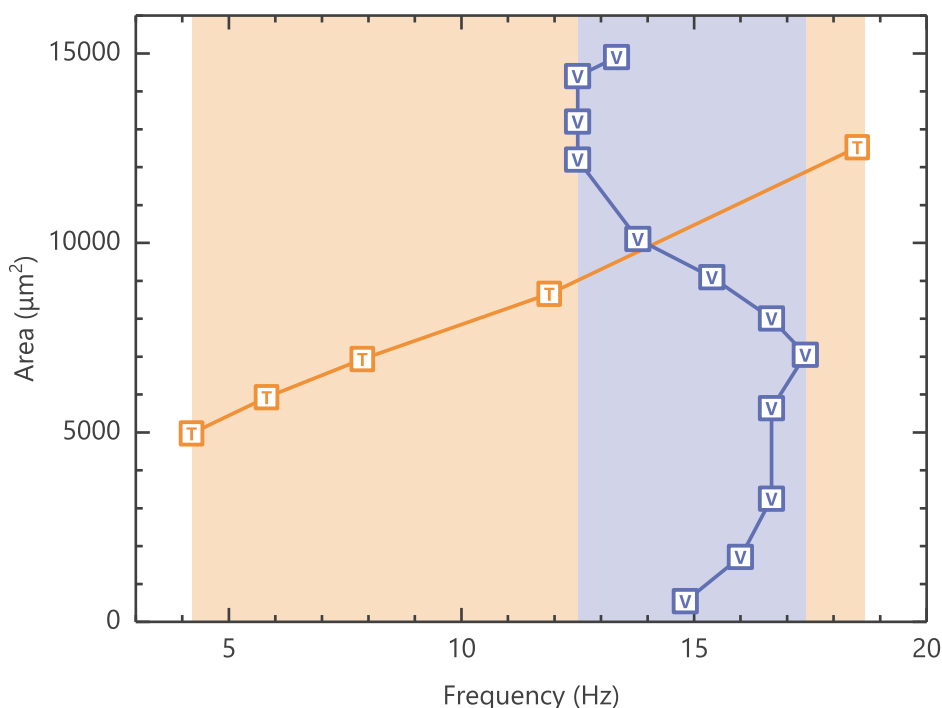


Figure 2:8 Plot for relationship between droplet generation frequency and size for V and T when oil flow rates both are $2 \mu\text{l}/\text{min}$. Detail measurement is available in Appendix A.3.2.

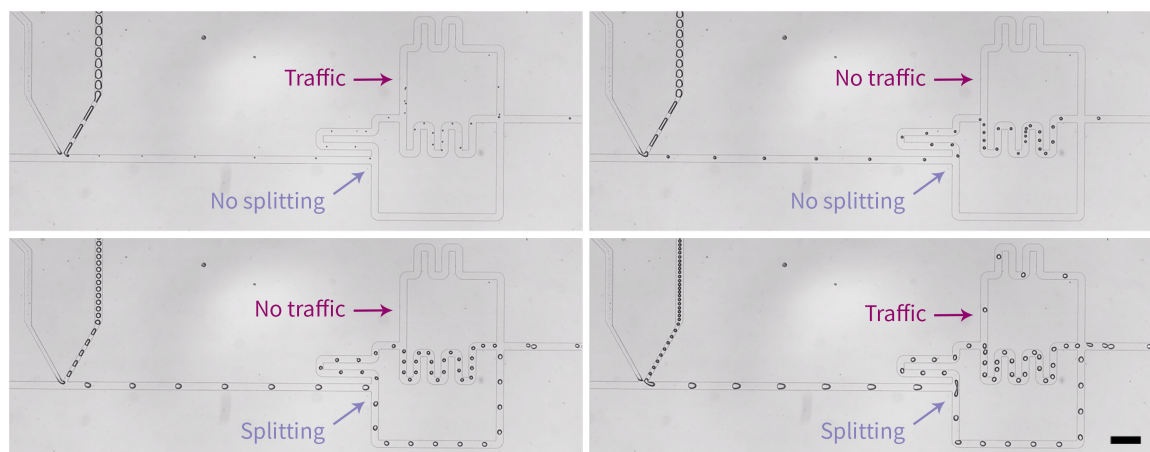


Figure 2:9 Four size series of droplets are generated at a V-junction and pass through a microfluidic network. The scale bar is 300 μm . The corresponding video is shown in VideoS 5.

It is also interesting to note that the current design allows for the generation of femtoliter-volume droplets. Using the same V-junction (50 μm cross-section), droplet diameters as small as $4.0 \pm 0.6 \mu\text{m}$ (33.5 fl in volume) can be generated along the control channel (which now acts as the “main” channel) in a controllable manner (Figure 2:10 and VideoS 6). Further geometric optimization and adjustments in surfactant concentration (such as those performed by Yang and co-workers)[110] should permit the direct formation of sub-femto-liter droplets. The V-junction can, therefore, access a larger experimental space for any given droplet-based assay than traditional T-junction formats, which suggests its potential as a truly universal droplet generator. Furthermore, adoption of the V-junction simplifies design factors by eliminating the need to consider the size of the droplet generator, and thus allowing researchers to focus only on ‘downstream’ functions.

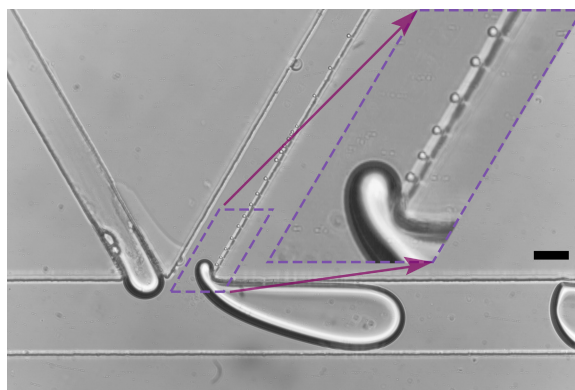


Figure 2:10 Image showing the formation of small droplets by application of a slight negative pressure in the control channel. Such droplets are obtained by splitting the forming droplet into two unequal daughter droplets. Smaller droplets, with a size of $4.0 \pm 0.6 \mu\text{m}$ in diameter, are conveyed along the control channel. The area marked with a purple dashed box is magnified to highlight these small droplets. The scale bar is 50 μm . The corresponding video is shown in VideoS 6.

2.3.3 The return of droplets: temporal gradient formation

Reagent incubation and temporal control of a given assay are essential steps in most chemical and biological experiments[51, 118], and cell-based screens[56]. Common incubating strategies implemented in microdroplet platforms have traditionally used long winding channels[96], large open reservoirs[53], droplet-trapping arrays for on-chip incubation[119] or off-chip storage (*e.g.* in Eppendorf tubes)[56, 120]. The temporal control of droplets (*i.e.* residence times) is traditionally achieved by simply assaying the droplets at different positions along the channel length and in the direction of flow. This is advantageous if a large number of droplets is available (meaning that many can be overlooked whilst the system is moved to a new measurement position). However, for small numbers of droplets (such as those obtained from small sample volumes), it is beneficial to assay all available droplets, which requires that each unit is associated with a specific residence time.

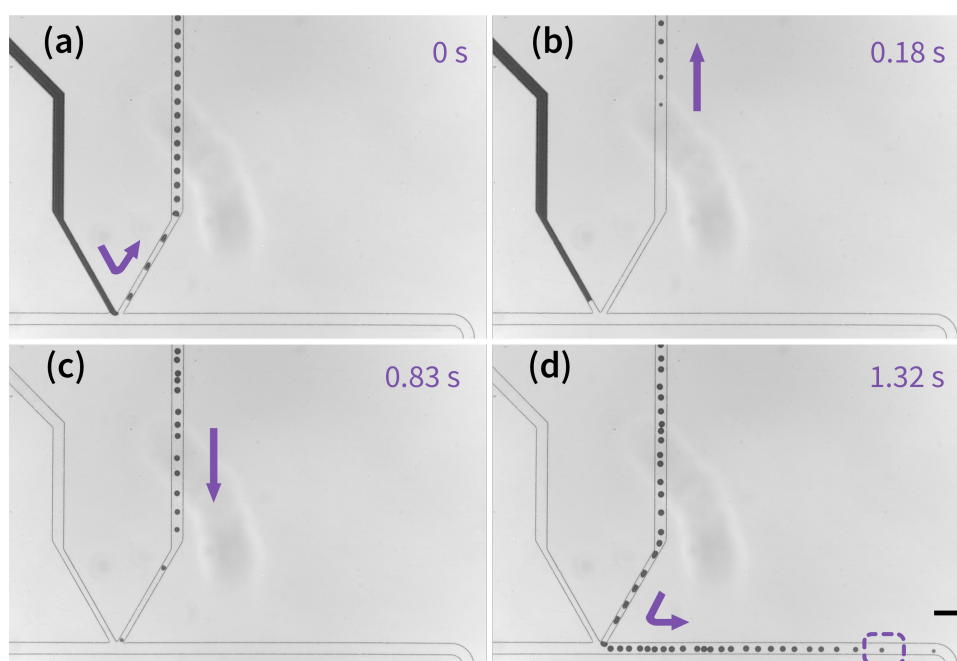


Figure 2:11 Generation of residence time gradients. (a) Droplets are generated in the control channel under negative pressure. (b) Water infusion is stopped. (c-d) Subsequently, a positive pressure is applied on the control channel: droplets come back and enter the main channel in a reversed sequence. The scale bar is 200 μm . The associated VideoS 7 is available.

In this context, the V-junction can conveniently perform such tasks without the need for any additional steps or control architectures, as illustrated in Figure 2:11 and VideoS 7. First, droplets are generated in the control channel to form a droplet sequence (Figure 2:11a). The flow of the discrete phase is then stopped (Figure 2:11b) and droplets in the

control channel are pushed back into the main channel (Figure 2:11c), effectively reversing the droplet sequence. If a fixed detection window is established in the main channel (marked by a purple dashed box in Figure 2:11d), droplets crossing this section will display a gradient of increasing incubation or residence time (Figure 2:12). This simple method allows performance of experiments where incubation or temporal gradients of the droplet-processed sample (which are much more complex to achieve) constitute analytical dimensions of interest.

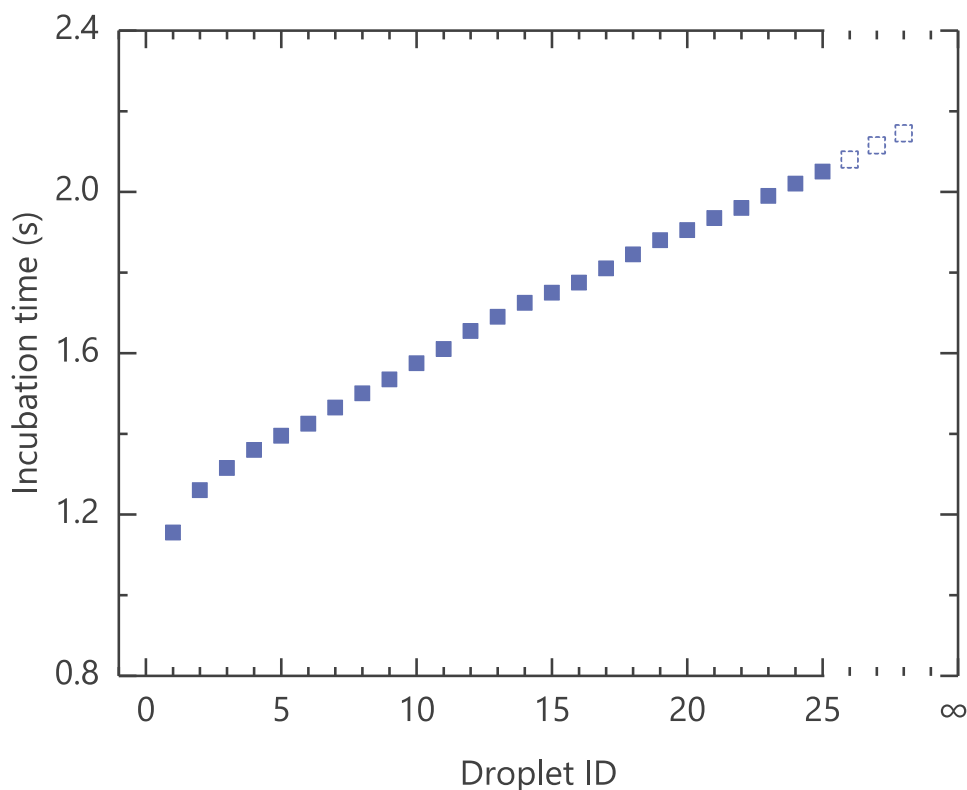


Figure 2:12 Variation of residence time of droplets in the sequence (*i.e.* temporal gradient) is measured at the area marked with the dashed box in Figure 2:11d.

2.4 Conclusions

We have presented a novel component for microdroplet generation, which we term the V-junction. The V-junction matches the simplicity of operation of regular T-junction formats whilst enabling a wider range of functionalities that are normally only attainable when using robotic, droplet-on-demand systems. Manufacturing of the V-junction does not add extra complexity to the fabrication process, and only requires the use of an additional pumping source. The V-junction can complete additional tasks such as the formation of

monodisperse droplets of a given size from the very first one, clean switching of samples and the production of a large range of droplet sizes. It is capable of creating a stable droplet sequence containing a wide range of sizes, spacings and frequencies, providing for a universal generation method that accommodates a broad range of downstream experiments. Furthermore, the system allows the creation of femtoliter-volume droplets and the performance of complex tasks such as on-chip incubation and the formation of droplets with temporal gradients. It is expected that such a component will be readily transferrable³ to any biology and chemistry laboratory wanting to implement droplet-based experimentation.

³ After publication of this study, we are encouraged to see that the V-junction format has been applied to droplet sample processing in a versatile and multifunctional fashion[39].

Chapter 3 Microfluidic-based droplet and cell manipulations using artificial bacterial flagella^ψ

Herein, we assess the functionality of magnetic helical microswimmers as basic tools for the manipulation of soft materials, including microdroplets and single cells. Their ability to perform a range of unit operations is evaluated and the operational challenges associated with their use established. In addition, we also report on interactions observed between the head of such helical swimmers and the boundaries of droplets and cells and discuss the possibilities of assembling an artificial swimming microorganism or a motorized cell.

3.1 Introduction

Helical microswimmers represent a category of microrobotic tools recognized as highly promising solutions for biomedical applications including minimally invasive surgery and targeted drug delivery[121–123]. Indeed, their implementation and controlled actuation within *in vivo* systems has recently been reported for deep tissue analysis[124]. The basic structure of a helical microswimmer is inspired by flagellated bacteria, where thin, whip like appendages protruding from the cell body are used to move the bacteria towards nutrients and other chemo-attractants. Accordingly such microswimmers are often termed artificial bacterial flagella (ABFs), and have been used to address the challenging issue of

^ψ This chapter was published in part in: Yun Ding, Famin Qiu, Xavier Casadevall i Solvas, Flora Wing Yin Chiu, Bradley J. Nelson, and Andrew deMello, *Microfluidic-Based Droplet and Cell Manipulations Using Artificial Bacterial Flagella*, *Micromachines* 7, 25 (doi:10.3390/mi7020025).

swimming within the low Reynolds number regimes typical on the microscale[125–127]. In contrast to chemically-propelled microswimmers[128, 129] and artificial cilia constructed from electroactive polymers[130, 131], magnetically actuated helical microswimmers rely on the application of magnetic fields for motion[132, 133]. Put simply, ABFs move in fluid environments by translating rotational motion to translational motion under the application of low-strength rotating magnetic fields. Such an approach is especially advantageous since the swimmer can be powered remotely (without the need for an on-board fuel source) and manoeuvred in a controllable and dynamic fashion (Figure 3:1a). Unsurprisingly, the development of control methods for ABF manipulations[127] and the characterization of their swimming properties[133–135] has been an active area of research, with recent efforts being focused on the addition of supplementary functional units (such as a “micro-holders”, “micro-bars” and a “micro-rings”) for the manipulation and transport of microscale objects[136–138], developing magnetic composites exhibiting superior biocompatibility[139, 140] and the functionalization of ABF surfaces to furnish them with novel properties[141–143]. Although, the fabrication of ABFs has been described in detail elsewhere[136, 144], it should be noted that adoption of two-photon polymerization (2PP) techniques for micro-/nanoscale fabrication[145–147] has allowed the rapid realization of three-dimensional micro-/nanoscale structures in a variety of materials[148–150].

In principle, ABFs can be used for manipulating microscopic objects to realize specific chemical and biological operations in both *in vitro* and *in vivo* environments. Nevertheless, to date, ABFs (with dimensions below 100 μm) have only been used to manipulate “hard” objects under idealized experimental environments, such as deionized water[136, 137]. Accordingly, their potential utility in many real biological systems remains an unresolved issue. Over the past two decades, microfluidic systems (commonly termed Lab-on-a-Chip devices) have become increasingly popular platforms in which to perform a wide range of chemical and biological assays and process a diversity “soft” biological entities (*e.g.* microdroplets, gel microparticles and cells)[151–154]. The ability to produce, manipulate and process soft objects in a high-throughput manner is an important feature of microfluidic systems, and their utility in applications such as digital PCR[53, 155] drug delivery systems[156], single cell analysis[157, 158], nanomaterial synthesis[159, 160] and the generation of artificial tissues[161, 162] is well documented. To demonstrate the feasibility of using ABFs to manipulate soft materials in the context of wide range of chemical and biological applications, we herein explore three highly relevant scenarios incorporating soft microdroplets and cells. Specifically, we assess the ability of ABFs to perform a range of unit operations on soft objects within microfluidic environments and evaluate the operational challenges associated with their use.

3.2 Equipment and Methods

3.2.1 ABF fabrication and suspension preparation

A 3D laser lithography system (Photonic Professional, Nanoscribe GmbH, Germany) was used to print all artificial bacterial flagella used in the current work. A negative-tone photoresist (IP-L 780, Nanoscribe GmbH, Germany) optimized for two-photon polymerization was used to ensure the creation of high resolution features. Briefly, processing consisted of writing, developing and drying the photoresist, followed by deposition of two metal layers (50 nm Ni and 5 nm Ti) by physical vapour deposition (Evaporation Plassys II, PLASSYS, France). A detailed description of the complete process can be found elsewhere[136]. To form a fluid suspension of microswimmers, the formed arrays were detached from a glass substrate via sonication. This involved removal of excess regions of glass substrate and insertion of the remaining substrate into a 1.5 ml centrifuge tube (Eppendorf LoBind, Sigma Aldrich, Switzerland). This was followed by addition of 0.2 ml of deionized water. Sonication at 40 kHz for 15 minutes resulted in the detachment of more than 95% of the microswimmers. Microswimmers intended for use in fluorinated oil (Fluorinert FC-40, Sigma Aldrich, Switzerland) were dehydrated under vacuum overnight before being suspended in FC-40 (containing surfactant).

3.2.2 PDMS chip fabrication and ABF encapsulation

PDMS (Sylgard 184, Dow Corning, USA) microdevices were fabricated using standard soft lithographic methods. Details of the entire procedure are provided elsewhere[104]. The top structured PDMS layer was subsequently bonded to a flat bottom PDMS layer by treatment in an oxygen plasma. Finally the whole assembly was contacted with a glass microscope slide to provide mechanical strength.

To create water-in-oil droplets, an oil phase FC-40 containing 3% (w/w) of a PFPE-PEG surfactant (EA-Surfactant, RainDance Technologies) was combined with a deionized water stream at a standard flow focussing geometry, with hydrodynamic motivation being provided by syringe pumps (neMESYS Low Pressure Dosing Module, Cetoni, Germany). To encapsulate single microswimmers within such droplets, microchannels were initially filled with the oil phase to expel gas bubbles and prevent wetting of the discrete phase. 20 μ l of the ABF suspension was then added through the chip-to-world connector. After delivering oil (20 μ l/min) and water (10 μ l /min) for a period of 90 seconds, a stable segmented flow of droplets (which were either empty or containing a single microswimmer) was achieved.

3.2.3 Magnetic control system

The primary part of the magnetic control system consists of three pairs of electromagnetic coils oriented along the Cartesian coordinate systems of three-dimensional space. Operational variables include magnetic intensity (up to 10 mT), rotation frequency (up to 200 Hz), pitch angle and yaw angle. A detailed description of the complete system can be found elsewhere[127, 136].

3.2.4 Treatment of biological cells

Human B lymphocyte cells were handled and processed according to the following protocol. Prior to experimentation, cells were cultured in RPMI 1640 growth medium (Invitrogen, UK) supplemented with 10% (v/v) heat-inactivated fetal bovine serum (Invitrogen, UK), 2 mM L-glutamine (Invitrogen, UK), 50 U/ml penicillin and 50 µg/ml streptomycin (Invitrogen, UK). For experiments, cells were washed once in calcium- and magnesium-free phosphate-buffered saline (Invitrogen, UK) and counted with a haemocytometer. Cells were then re-suspended in calcium- and magnesium-free phosphate-buffered saline with 2% (v/v) heat-inactivated fetal bovine serum in the desired concentration and volume.

To ensure that microswimmers did not stick to exposed microchannel surfaces, a thin layer of PDMS (100 µm in height) was deposited on a microscope glass slide (76 × 26 × 1 mm; Menzel-Glaser, Germany) via spin-coating and followed by the curing at 70 °C in oven for 1 hour. Subsequently a sheet of SA8S-0.5-SecureSeal (Grace Bio-Labs, USA) was placed over the PDMS layer to form 8 chambers, (7 mm wide, 7 mm long and 0.5 mm deep).

3.3 Experiment, Results and Discussion

3.3.1 Operation of an ABF inside a microfluidic droplet

To begin, we encapsulated ABFs within water-in-oil droplets generated using a microfluidic flow-focusing geometry and assayed the capacity for ABFs to swim within an isolated nL-volume compartment. Droplets (or segmented flows) produced within microfluidic systems offer significant advantages when performing high-throughput biological and chemical experimentation[56, 84, 163]. Briefly, fL–nL volume droplets can be generated at kilohertz frequencies, where each droplet acts as an isolated assay volume. Since droplet volumes are extremely small, a wide range of assays can be performed using reagent volumes 6-9

orders of magnitude less than typically used in macroscale platforms. Additionally, the use of an immiscible continuous phase to encapsulate each droplet ensures minimal reagent interaction with channel walls and the removal of residence time distributions.

Various types of sample (down to the single molecule or cell level) can be encapsulated or dosed into microdroplets for a range of applications[164, 165]. Interestingly, Brouzes *et al.* recently encapsulated micron-sized super-paramagnetic beads to extract desired molecules from droplets in a segmented flow[166]. Although the motion of such magnetic beads can be controlled to some degree, locomotion at small scales (*c.f.* the scallop theorem) cannot easily be achieved with these systems[167]. This shortcoming can however be readily overcome through the use of robotic ABFs.

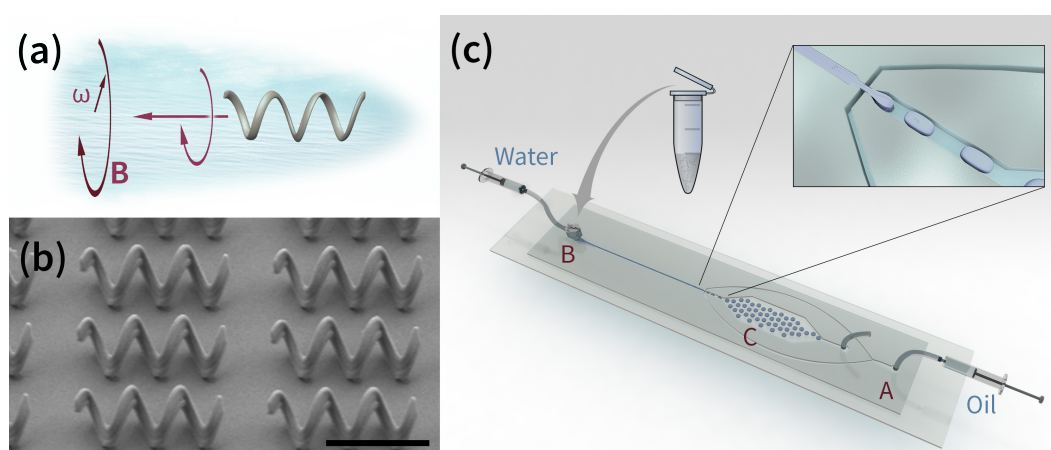


Figure 3:1 (a) Illustration of a helical ABF propelled by a rotating weak magnetic field B ; (b) SEM image of a printed (and uncoated) MS array on a glass substrate (scale bar is $10\ \mu\text{m}$); (c) Schematic of the PDMS microdevice that contains a flow focusing structure for encapsulating ABFs in droplets. Port A serves as the oil inlet and port B is coupled to a chip-to-world connector, from which the aqueous suspension of ABFs is introduced.

For the current experiments, ABFs ($16\ \mu\text{m}$ in length and $5\ \mu\text{m}$ in diameter) were fabricated via 2PP-based 3D laser lithography. The surface of the formed ABFs was then coated with a $50\ \text{nm}$ Ni film and a $5\ \text{nm}$ Ti film. The Ni layer provides the ABF with its magnetic properties and the Ti layer (autoxidized to titanium dioxide) increases biocompatibility[168]. Figure 3:1b presents an SEM image of a printed ABF array on a glass substrate. ABFs were harvested by ultrasonic detachment from the substrate and prepared as a suspension for subsequent use. A polydimethylsiloxane (PDMS) chip incorporating a flow focusing droplet generator was used to encapsulate single ABFs inside aqueous droplets (of nL volumes). Figure 3:1c illustrates the fluid connections and generic chip structure used to form aqueous droplets and encapsulate ABFs. Specifically, regions A and B define

the oil (FC-40) and water inlets, respectively, and region C contains a storage chamber for droplet incubation and observation. To ensure that ABF losses within the connecting tubing (via adhesion of ABFs onto the plastic surfaces) are minimized, a chip-to-world connector[169] is used in region B to allow direct injection of a small but defined volume of the ABF suspension. After encapsulation, ABFs were controlled using an in-house electromagnetic control system that generates a rotational magnetic field, which can be monitored and varied in real-time.

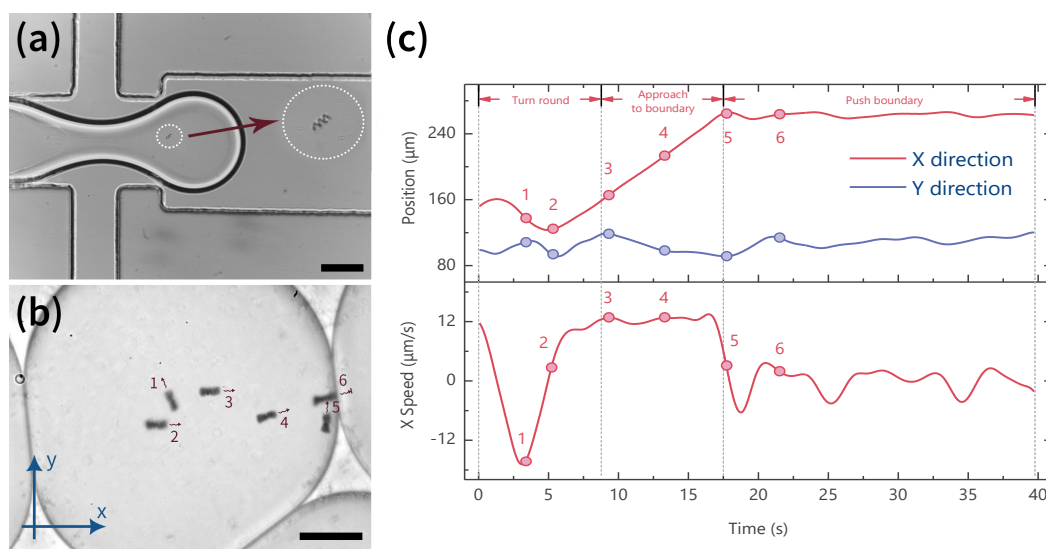


Figure 3:2 (a) Image showing the formation of an ABF-containing droplet. The ABF is shown within the white dotted circle; (b) A time-lapse image showing controlled locomotion of an ABF within a droplet. The magnetic field is 90 Hz and 9 mT; (c) Variation of ABF position and speed for experiment shown in (b). The upper plot illustrates the x,y position as a function of time and the lower plot shows the variation of velocity in the x direction. It is noted that when the ABF reaches the droplet boundary (at 17.5s), the net displacement and average speed in x are both zero. Scale bars correspond to 100 μm .

Figure 3:2a illustrates the encapsulation of an ABF inside an aqueous droplet at a microfluidic flow focusing geometry. Without additional modification of the droplet generation process, ABFs could be loaded into droplets in a high-speed and direct manner[170, 171], with droplet occupancies following a Poisson distribution[53, 172]. After formation, droplets were motivated to the storage chamber, where ABF swimming performance could be evaluated. Figure 3:2b and VideoS 8 (in Appendix D.2) show a pair of ABFs (in a “chain configuration”[173]) swimming within the confines of a 5 nL droplet in response to a dynamically varying electromagnetic field. An analysis of both the position and speed of the swimmer is presented in Figure 3:2c. It is observed that the swimmer can be steered in any desired direction through variation of the applied electromagnetic field, and moreover remains within the confines of the droplet, even when forced to swim against the droplet

boundary (for example at 17.5 seconds). In this regard, the interfacial tension associated with the curved droplet boundary generates a pressure difference between the inside and the outside of the droplet (the so-called Laplace pressure)[80, 115], which is given by,

$$\Delta P = \gamma \left(\frac{1}{R_1} + \frac{1}{R_2} \right) \quad (3:1)$$

where, γ is the surface tension and R_1 and R_2 are two principal radii of curvature. Since droplets are squeezed between the bottom and top chip layers, R_1 and R_2 can be considered to be half the channel height and the radius of a droplet can be extracted from the brightfield image. Using the surface tension values for FC-40 with 3% (w/w) PFPE-PEG surfactant and a typical pushing pressure of 200 pN[60, 137, 174], we can estimate the equivalent radius for the push effect by an ABF to be larger than 1000 μm . Accordingly, for the current system (where the average droplet radius is 100 μm) the increased proportion of localized curvature will be less than 1/10, and thus droplet deformation by an ABF can be considered negligible. Indeed, as long as an ABF has no affinity for the droplet/continuous phase boundary, it will remain inside the droplet under all conditions. Accordingly, we expect that the integration of ABFs with such droplets offers new opportunities for the direct manipulation of droplet contents, such as cells, nanomaterials, bacteria and other microorganisms[52].

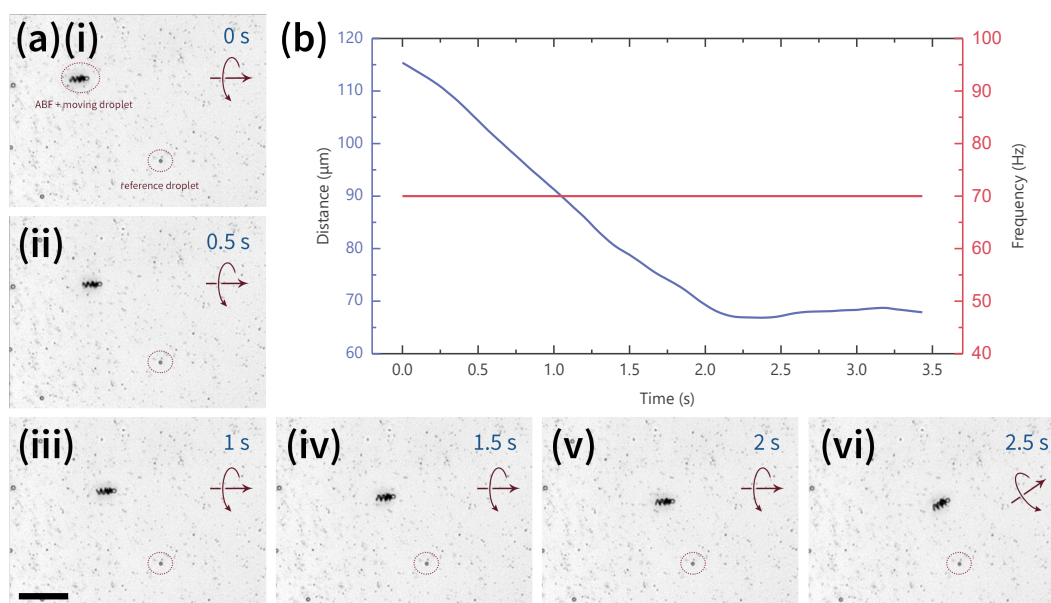


Figure 3:3 (a) Time lapse images of an ABF transporting a microdroplet within a 25 μm deep PDMS chamber, under the application of a 70 Hz, 7 mT magnetic field. The scale bar corresponds to 50 μm ; (b) Assessment of the relative distance between the transported droplet and a reference droplet as a function of time.

3.3.2 Manipulation of microdroplets

The ability to controllably propel and manipulate individual droplets is an additional and potentially important unit operation[175–178]. Indeed, such operations have been used to fabricate artificial tissues[162] and are indispensable in digital microfluidic applications[179]. However, it is noted that, to date, digital microfluidic platforms have been unsuccessful in robustly manipulating sub-nL droplets[180]. Accordingly, we assessed the ability of ABFs to individually transport picoliter-sized droplets. Water droplets of a size comparable to our ABFs were generated using a 5 μm wide flow-focusing geometry and transferred to a reservoir containing ABFs.

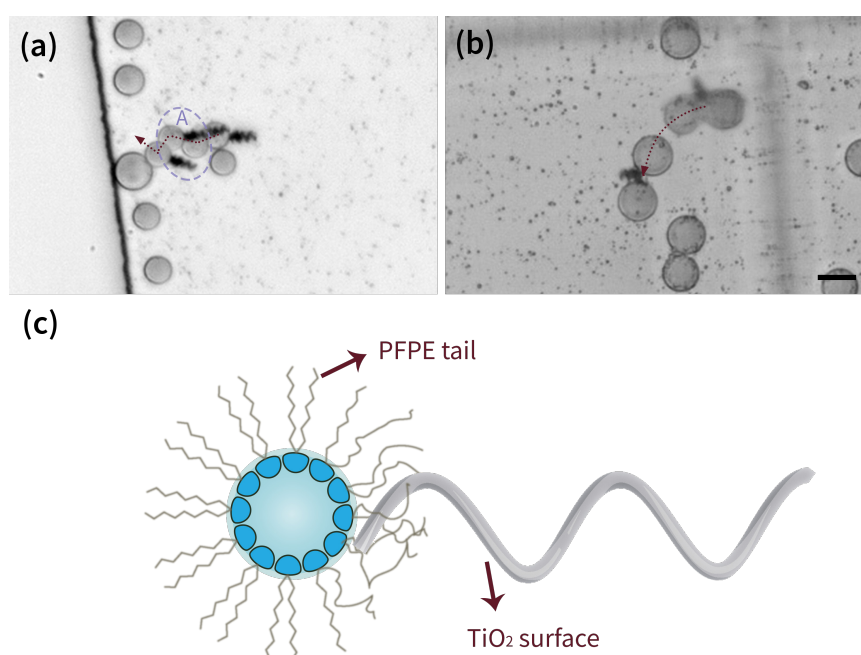


Figure 3:4 (a) A time-lapse image showing the transportation of a large droplet by an ABF across a 25 μm deep PDMS chamber, under the application of a 70 Hz, 7 mT magnetic field. Note the “swinging” behaviour observed in region A; (b) A time-lapse image showing two large droplets being simultaneously transported along a 100 μm deep PDMS chamber; (c) Schematic explanation of the “soft” adhesion observed between surfactant coated droplets and the tip of an ABF. The scale bar corresponds to 20 μm and the straight black line defines the chamber wall.

Data presented in Figure 3:3 demonstrate that ABFs are efficient in transporting aqueous microdroplets. In addition to factors such as rotation frequency of the magnetic field, fluid viscosity[133] and payload size, propelling performance (*i.e.* speed) is largely controlled by the friction between the droplet and the reservoir walls. Indeed, three main situations could be identified. First, when operating within “open” reservoirs (*e.g.* a plastic tank, 2 cm long, 1 cm wide and 0.5 cm deep), both droplets and ABFs could freely float on the fluorinated continuous phase (of higher density) and droplet transport was facile. For example, VideoS

9 shows a droplet being propelled by an ABF less than half its size, even against the direction of a residual convective flow. Second, in fully enclosed (PDMS or PMMA) chambers, droplets that were large enough to be squeezed between the top and bottom walls, or droplets that displayed some degree of affinity for the chamber walls, could not be maneuvered (see VideoS 10). Finally, droplets with diameters less than the chamber height and no apparent affinity for the channel walls could also be smoothly transported within enclosed chambers. In this regard, Figure 3:3a shows a sequence of images of a small droplet being transported along a PDMS chamber 25 μm deep (also in VideoS 11). In addition, Figure 3:3b describes the relative position of a reference droplet over time. Droplet size (a proxy of payload) was also observed to affect the delivery rate. Figure 3:4a illustrates the propulsion of a larger droplet within an identical PDMS chamber and using the same operational field parameters (70 Hz and 7 mT). It was observed that the larger droplet could be maneuvered at a speed of 7.5 $\mu\text{m}/\text{s}$, which is approximately 4 times slower than the achievable velocity of the droplet described in Figure 3:3 (30.3 $\mu\text{m}/\text{s}$). This indicates that the payload (in this case volume) of the sample to be transported is an important factor in defining ABF-mediated delivery. It should also be noted that ABF swimming performance within the FC-40 fluorinated oil (dynamic viscosity = 4.1 cP) closely mirrored that within aqueous environments (*i.e.* deionized water; dynamic viscosity, 0.89 cP), although with reduced swimmer velocities[136, 141]. The characterization of ABF swimming capabilities in FC-40 is shown in Figure 3:5a and b.

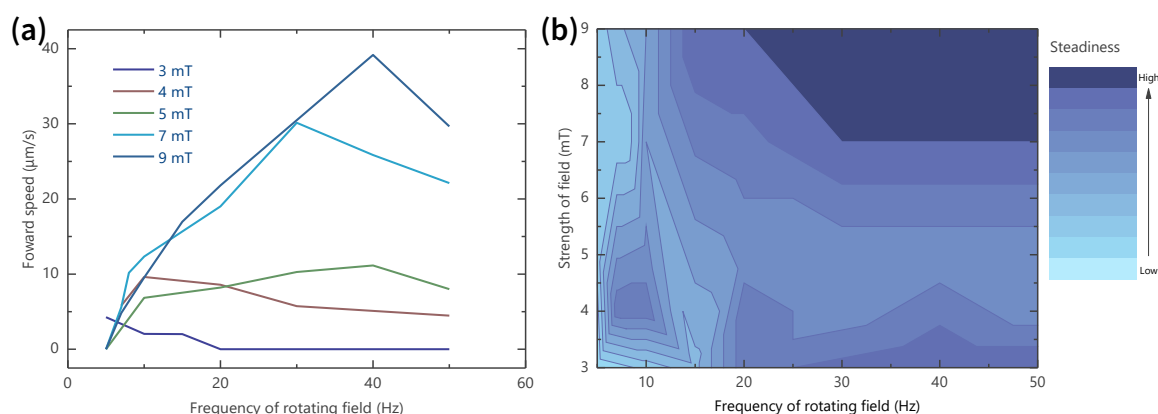


Figure 3:5 Swimming characterization in FC-40 oil (containing 3% w/w PFPE-PEG-PFPE tri-block surfactant) along a 100 μm deep PDMS chamber. (a) Forward swimming speed of ABFs as a function of magnetic field strength and rotation frequency; (b) Evaluation of the steadiness of swimming. Here, higher values represent reduced steadiness. The degree of “wobbling” and “shifts” in movement are two major (negative) factors used to assay the swimming performance of ABFs (the assay methodology is provided in Appendix B.1). The combination of these data provides the range of operational parameters that deliver stable swimming performance.

An interesting result was the observation of “soft” adhesion forces between the TiO₂-ABFs and the surface of both, droplets and cells. This unexpected interaction is instrumental in aiding reliable manipulation of soft particles. Figure 3:4a (area A) and VideoS 12 clearly illustrate the effect, where one droplet is successfully delivered to a larger one despite the ABF undergoing a brief period of destabilization. Adhesion also makes it possible for an ABF to transport two droplets simultaneously (Figure 3:4b and VideoS 13). We suspect that this phenomenon is caused by the adsorption and entanglement of the perfluoropolyether surfactant tails on the TiO₂ surface (Figure 3:4c), a mechanism similar to that reported and characterized by Walczak *et al.*[181]. In principle, such adhesion effects could be used to more closely associate ABFs with droplets (or cells), to create biosynthetic, propulsion assemblies, mimicking naturally swimming microorganisms such as *E. coli* and spermatozoa.

3.3.3 A motorized cell

Single cell manipulation via magnetic micro-robotics has previously been realized through the use of a U-shaped micro-transporter[182]. It is noted however, that this tool is limited to transport on surfaces since it lacks the 3D locomotion capabilities of ABFs. To this end, we assessed the feasibility of assembling ABFs on individual cells for propulsion purposes. Human B lymphocytes (that identify pathogens when surface antibodies bind to a foreign antigen) are key components within the human immune system, and thus interesting candidates for “motorization”.

We successfully assembled and disassembled B cells onto ABFs. Figure 3:6a and VideoS 14 show such a process. Here, it can be seen that an ABF is steered toward a Human B lymphocyte cell at a velocity of 8.7 $\mu\text{m/s}$ (accelerated from standing). On contact, the cell/ABF assembly continues towards the target cell at a velocity of 2.9 $\mu\text{m/s}$. After the ABF has delivered the cell to the desired location, it then disassembles and retreats at a velocity of 18.1 $\mu\text{m/s}$. Compared to data associated with droplet transport, assembly and motivation of Human B lymphocyte cells is associated with a stronger entanglement effect with the ABFs, which is likely to be due to the richness and complexity of the biological cell membrane (which will contain a wide variety of cell receptors and adhesion proteins). In some cases, this interaction was so strong that cells could be dragged by the ABF (Figure 3:6b and VideoS 15) to form tandem cluster configurations, such as those shown in Figure 3:6c (and VideoS 16). Observation of such motorized cells over a period of 1 hour of operation revealed no observable changes in morphology. Moreover, viability assays

of cells actuated by ABFs indicated no change in cell mortality when compared to control samples (details are provided in the Appendix B.2).

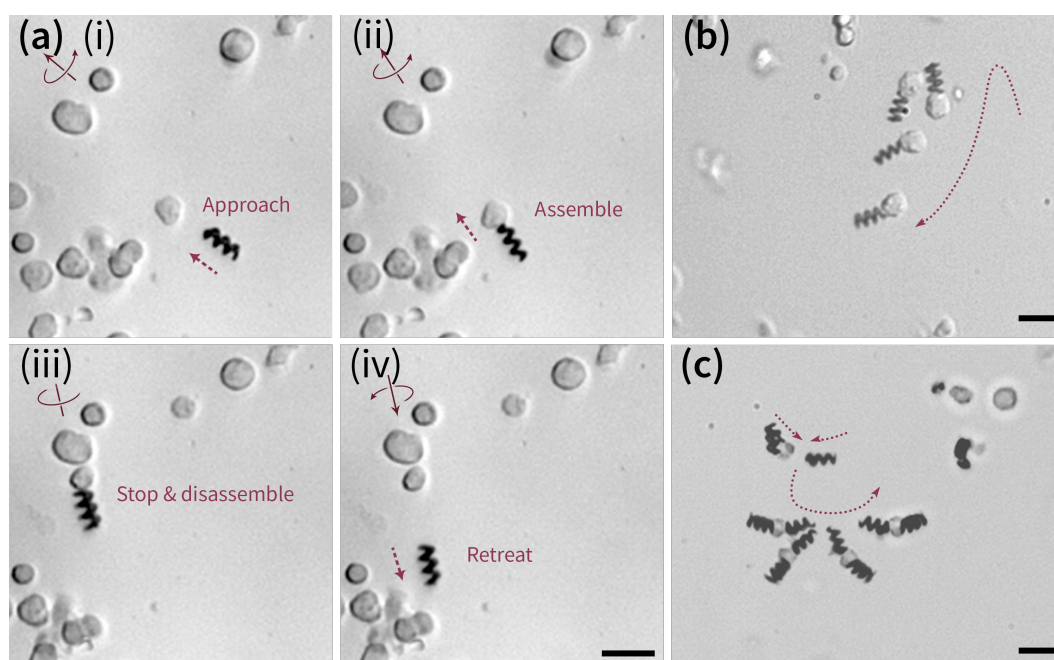


Figure 3:6 The process by which a motorized cell is assembled and disassembled. In (i) and (ii) an ABF approaches the desired cell, contacts it and assembles. The B-cell-ABF assembly then moves forward following the direction of the applied rotating magnetic field (iii and iv). To disassemble, the rotating direction of magnetic field is simply reversed, allowing the ABF to move back and detach from the cell; (b) A time-lapse image of a cell being dragged; (c) A time-lapse image of the process of forming an ABF-cell-ABF configuration. The scale bar corresponds to 20 μm .

3.4 Conclusions

In conclusion, we have explored and validated for the first time the manipulation of soft materials by magnetically actuated, helical microswimmers. Such swimmers were shown to exhibit uniform swimming performance in a variety of fluid environments (including deionized water, cell growth media and fluorinated oils). Significantly, precise and controlled ABF locomotion was demonstrated for the first time within confined fluid volumes (such as water-in-oil droplets). Furthermore, the intimate interaction between ABFs and both microdroplets and Human B lymphocyte cells was leveraged to allow controlled assembly and disassembly of objects with complex configurations. We recognize that such drop-

let/cell-ABF assemblies could be used to mimic biological microorganisms, whilst “motorized” B cells (not limited to B cells⁴) have the potential to enable targeted immunotherapies *in vivo*. Accordingly, we believe that ABFs represent a promising engineering tool for microfluidic droplet and cell-based experimentation at the single unit level.

⁴ Building on the work presented in this chapter, we note that ABFs have since been used to successfully motorize sperm cells and assist in fertilization[183].

Chapter 4 From single-molecule detection to next-generation sequencing: microfluidic droplets for high-throughput nucleic acid analysis^ψ

This chapter surveys recent developments in the use of droplet-based microfluidics for nucleic acid analysis, first elucidating principles and advantages of adopting droplets for this task and second highlighting key areas where such microfluidic tools have already made significant impact.

4.1 The role of droplets in next-generation sequencing

4.1.1 Next-generation sequencing: an introduction

Next-generation sequencing (NGS) is a commonly used umbrella term describing ultra-high-throughput methods for nucleic acid sequencing[184]. Such methods allow sequencing at rates of thousands of gigabases per week and at a cost of less than a dollar per gigabase, and have revolutionized genetic and genomic science.

^ψ This chapter was published in part in: Yun Ding, Jaebum Choo, and Andrew J. deMello, *From Single-Molecule Detection to next-Generation Sequencing: Microfluidic Droplets for High-Throughput Nucleic Acid Analysis*, *Microfluidics and Nanofluidics* 21, 58 (doi:10.1007/s10404-017-1889-4).

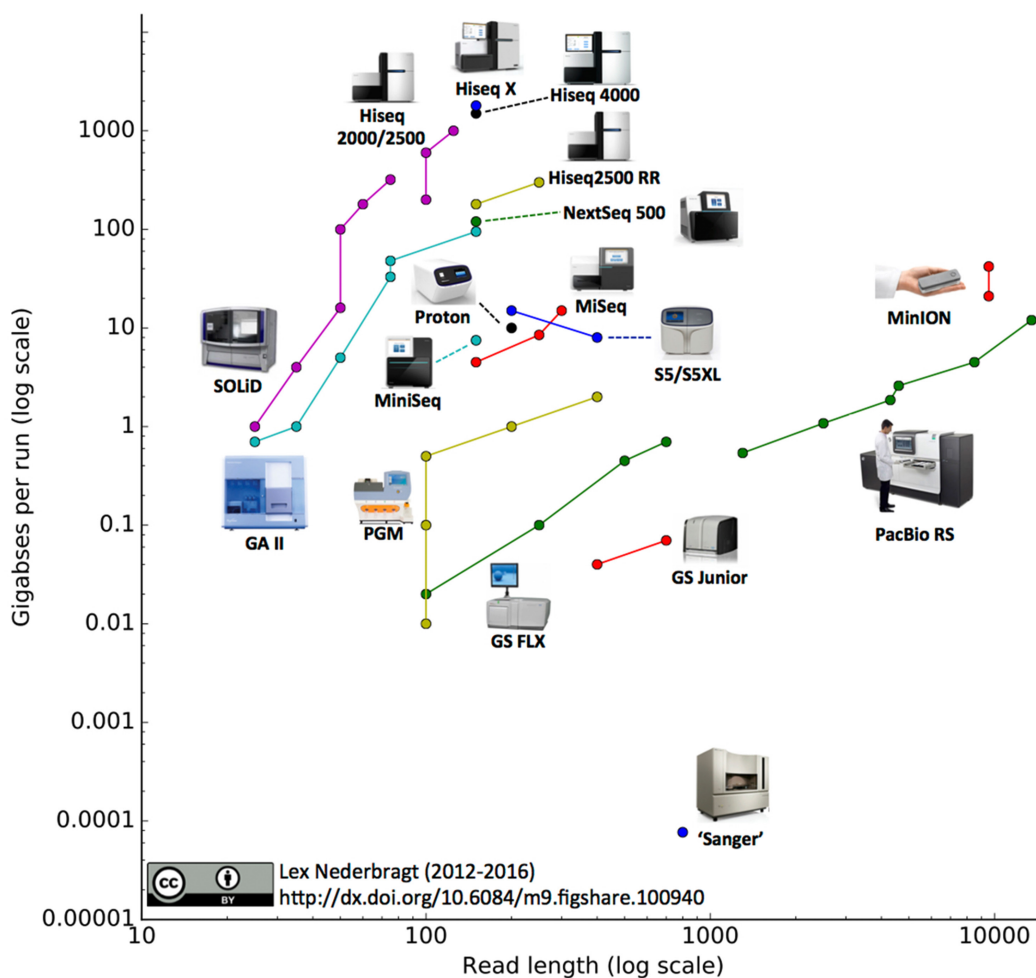


Figure 4:1 Classification of next-generation sequencing methods. Data are based on throughput metrics for different platforms since their introduction. Results are visualised by plotting throughput in raw bases per run versus read length. Adapted from reference [185] under a CC BY license.

A number of distinct NGS platforms are commercially available (most notably, those offered by Illumina, Roche and Life Technologies). Although metrics such as cost per run, cost per base, error rate, and throughput are important when evaluating performance, the read length and number of reads per run are perhaps most useful when judging sequencing capacity[186]. Since 2012, an annual comparison of available sequencing platforms (based on these two factors) has been presented by Lex Nederbragt at the University of Oslo, with cumulative data from July 2016 illustrated in Figure 4:1[185]. Currently, Illumina's *HiSeq* platforms lead the field in terms of throughput and unsurprisingly dominate the sequencer market share. That said, most mainstream NGS systems make use of short-read lengths, which yields limitations in the resolution of structural mutations and ability to perform *de novo* sequencing[187]. Accordingly, NGS technologies capable of long reads (such as those provided by Pacific Biosciences and Oxford Nanopore) are becoming increasingly important, although still in the early stages of development. Finally, it should be noted that

extended read lengths can be accessed indirectly via synthetic long-read (SLR) sequencing methods, which leverage short-read sequencing data to generate synthetic long reads via partitioning, label indexing and remapping techniques[188]. SLR methods are compatible with existing short-read sequencing platforms and have already shown utility in the recovery of missing sequences, haplotype phasing and transcriptome analysis[189–191].

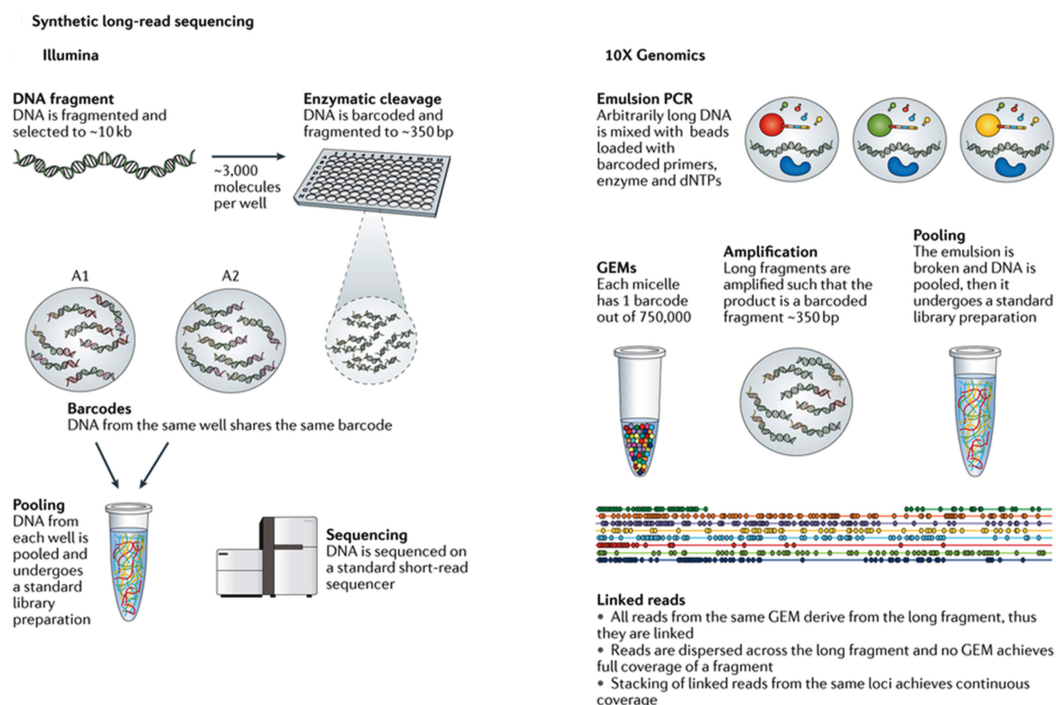


Figure 4:2 Workflow comparison between two commercial synthetic long-read sequencing platforms. Left: Illumina's *TruSeq* technology. Genomic DNA templates are fragmented into 8–10 kb pieces. They are then partitioned into a microtitre plate, such that there are around 3,000 templates in a single well. Within the plate, each fragment is sheared to around 350 bp and barcoded with a single barcode per well. The DNA is then be pooled and sent through standard short-read pipelines. Right: 10X Genomics' emulsion-based sequencing platform. With as little as 1 ng of starting material, the *GEMCode* can partition arbitrarily large DNA fragments, up to ~100 kb, into micelles (called 'GEMs') along with gel beads containing adapter and barcode sequences. GEMs typically contain ~0.3× copies of the genome and 1 unique barcode out of 750,000. Within each GEM, the gel bead dissolves and smaller fragments of DNA are amplified from the original large fragments, each with a barcode identifying the source GEM. After sequencing, the reads are aligned and linked together to form a series of anchored fragments across a span of ~50 kb. Unlike the Illumina system, this approach does not attempt to get full end-to-end coverage of a single DNA fragment. Instead, the reads from a single GEM are dispersed across the original DNA fragment and the cumulative coverage is derived from multiple GEMs with dispersed—but linked—reads. Adapted from reference [192] with permission.

4.1.2 Droplet partitioning

A number of NGS methods make use of microtiter plates to partition samples[190, 193]. For example, haplotype determination can be achieved by dilution of samples into 384-well

plates prior to sequencing library preparation (Figure 4:2)[188]. A key feature of “dilution haplotyping” is the fact that the low concentration of molecules per partition reduces the probability that a contained DNA molecule has an overlapping sequence with another. Unfortunately, dilution methods based on microtiter plates are instrumentally complex and limited in their partitioning capacity. To address these limitations, researchers from 10X Genomics and Stanford University have recently transformed haplotyping analysis (and many other applications) by using droplet-based microfluidics to achieve large-scale partitioning in a rapid and efficient manner[194]. Specifically, a double-cross junction was used to construct phased sequencing libraries from ng inputs of high molecular weight DNA. Hydrogel beads can then be used as barcode delivery reagents, to allow the controlled loading of individual barcodes into droplet partitions. This core technology platform has since been refined to enable the generation and analysis of more than one million droplet partitions using over four million barcodes and the integrated sequencing of up to 10^4 (single) cells (Figure 4:2).

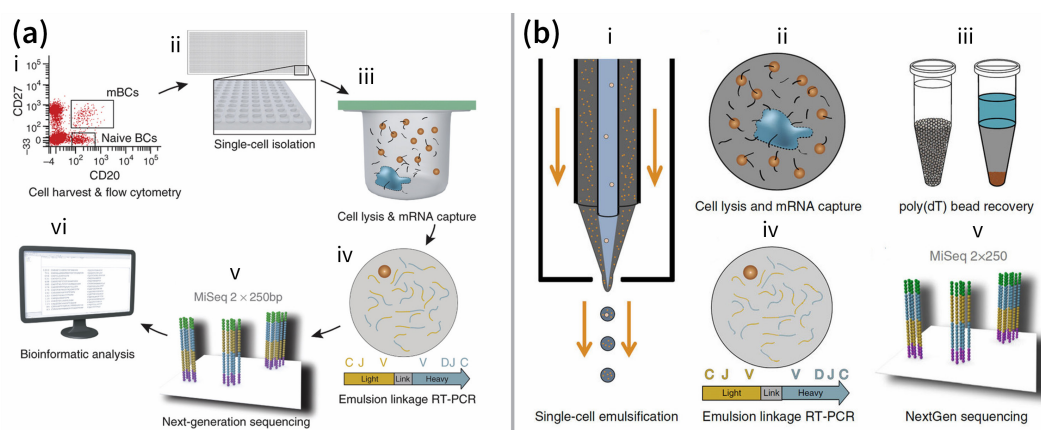


Figure 4:3 (a) Well-based high-throughput sequencing of an antibody repertoire. (i) B cell populations are sorted for desired phenotype. (ii) Single cells are isolated by random settling into wells (56 μm diameter) printed in PDMS slides (170,000 wells/slide); 2.8 μm poly(dT) microbeads are also added to the wells (average 55 beads/well). (iii) Wells are sealed with a dialysis membrane and equilibrated with lysis buffer to lyse cells and anneal VH and VL mRNAs to poly(dT) beads. (iv) Beads are recovered and emulsified for cDNA synthesis and linkage PCR to generate an ~850-base pair VH-VL cDNA product. (v) Next-generation sequencing is performed to sequence the linked strands. (vi) Bioinformatic processing is used to analyse the paired VH:VL repertoire. Adapted from reference [195] with permission. (b) Droplet-based high-throughput sequencing of an antibody repertoire. (i) An axisymmetric flow-focusing nozzle isolated single cells and poly(dT) magnetic beads into emulsions of predictable size distributions. (ii) Single-cell VH and VL mRNAs annealed to poly(dT) beads within emulsion droplets. (iii) poly(dT) beads with annealed mRNA were recovered by emulsion centrifugation to concentrate the aqueous phase (left) followed by diethyl ether destabilization (right). (iv) Recovered beads were emulsified for cDNA synthesis and linkage PCR to generate an ~850-base pair VH-VL cDNA product. (v) Next-generation sequencing analysis. Adapted from reference [196] with permission.

The transition from microtiter plate to droplet-based formats has also impacted high-throughput cellular assays. For example, DeKosky *et al.* recently developed a method able to preserve heavy-chain (VH) and light-chain (VL) antibody pairing information when performing high-throughput immune repertoire sequencing[195]. The authors were able to partition single B cells into spatially isolated compartments, whilst at the same time inserting poly(dT) magnetic beads as barcodes. Cells could be lysed, with mRNA captured on the magnetic beads and then reverse transcription and emulsion VH-VL linkage PCR performed. After this complex sequence of operations, linked transcripts were finally subjected to NGS. Initially, four PDMS slides each containing 170,000 wells (with each well having a volume of 125 pL) were designed to concurrently accommodate and process 68,000 B cells (with a 95% probability of there being only one cell per well). In each experimental run, over 50,000 single B cells could be deposited and analysed. Subsequently, the same team replaced the well-based strategy with a droplet-based microfluidic system[196]. This direct upgrade enabled the high-throughput processing of over one million single B cells per experiment. The schematic procedures for both workflows are shown in Figure 4:3.

4.1.3 Droplet-based nucleic acid amplification

Amplification is a prerequisite for the vast majority of nucleic acid assays. The polymerase chain reaction (PCR), the first *in vitro* nucleic acid amplification technique, was introduced by Kary Mullis over three decades ago[197], and is still to this day the preferred approach for most amplification-involved procedures. Conventional PCR is performed using bulk thermal cyclers, where Peltier effect thermoelectric heating is used convert electrical energy into a temperature gradient[198]. Almost all conventional thermal cyclers possess large thermal masses, which result in high power requirements and relatively slow heating and cooling rates. Unsurprisingly, a large number of microfluidic approaches have been developed for PCR over past twenty years to address these limitations. Although, highly successful in allowing amplification to be performed in a rapid and efficient manner[89, 199, 200], batch and continuous flow approaches do not drastically change how PCR is used by experimentalists to generate biological information. Conversely, the adoption of droplet-based formats for PCR over the recent years has begun to transform the application and utility of PCR in complex biological experiments[61, 201]. In addition to obvious advantages, such as reduced reaction times, minimal sample consumption and contamination-free operation, other intriguing features such as massively parallel operation, high amplification sensitivities and reduced amplification bias have begun to fundamentally change how biologists view and use the reaction[202–204].

Droplet-based PCR can be carried out in various microfluidic formats, which are broadly categorized as being either on-chip or off-chip[205]. For example, early studies by Schaerli *et al.*[96] used a radial microfluidic device, containing concentric temperature zones, to perform single-copy amplification in 160 pL-volume droplets (Figure 4:4a). Batch on-chip microfluidic systems can be created by fabricating integrated chambers that trap or hold large numbers of droplets subsequent to their production. As previously described, Hatch *et al.* showed an elegant example of such a format[53], where over a million droplets containing PCR mix were packed into a microfluidic chamber for both thermal cycling and real time product detection. Interestingly, the majority of droplet-based PCR assays have incorporated off-chip amplification, whereby PCR droplets are generated on-chip using standard protocols and then collected and amplified in standard PCR reaction tubes. Such an approach is interesting since it leverages the ability of microfluidics to generate large numbers of defined droplets on short timescales and also the convenience of commercial formats or instruments for thermal cycling (rather than more involved approaches to thermal control[206, 207]). The interested reader is directed to Table 4:1, which summarises representative droplet-based PCR studies over the past decade.

It should be remembered that nucleic acid amplification is not limited to PCR, with a large number of alternative amplification methods being developed in the intervening years[208]. These include the ligase chain reaction (LCR) and isothermal amplification methods such as rolling circle amplification (RCA), loop-mediated isothermal amplification (LAMP), recombinase polymerase amplification (RPA), helicase-dependent amplification (HDA), ramification amplification method (RAM), multiple displacement amplification (MDA) and nucleic acid sequence-based amplification (NASBA). Almost all of these basic techniques have been successfully transferred to droplet-based microfluidic formats[209]. Isothermal amplifications are particularly attractive since they are characterised by short reaction times and require only simple thermal control architectures. These features suggest significant potential for use in point-of-care diagnostic applications. For example, LAMP has been shown to be rapid, accurate, and cost-effective in the diagnosis of infectious diseases such as severe acute respiratory syndrome (SARS), malaria and African trypanosomiasis[210–213]. Critically, LAMP analysis can be performed simply by visual inspection or through the use of a smartphone camera[214, 215]. Recently, Rane *et al.*[216] demonstrated an integrated device for digital LAMP, combining droplet generation, incubation (amplification) and real-time detection. Using such an approach, more than one million droplets could be processed in less than two hours in a continuous manner.

Table 4:1 Emulsion PCR summary

PI	Mineral oil used	Polymerase system used	PCR MIX	Template	Droplet generation	Cycles	PCR length	Droplet break-age	Comments
Griffiths, Andrew (Cambridge, UK)[61]	4.5 % Span 80 0.4 % Tween 80 0.05 % Triton X-100 95.05 % mineral oil	Pfu Turbo DNA polymerase 5.2 µl PM in 260 µl	1x Cloned Pfu buffer 1 µg/ml BSA 0.3 µM primer 0.2 mM dNTPs ≤109 molecules template	DNA fragments	Stirring	25	~1.3 kbp	Diethyl ether Precipitation/PCR clean up	No BSA no amplification!
Glökler, Jörn (MPI, Berlin)[62]	73 % Tegosoft DEC 20 % mineral oil 7 % ABIL WE 09	1x Encyclo Polymerase MIX 0.025 U/µl Taq	0.2 mM dNTPs 0.4 µM primer 1x Encyclo buffer PM 1 µg/ml BSA template	~500 ng cDNA	Vortex	15–20	100–200 bp	Isobutanol PCR clean up kit	
Chudakov, Dmitriy (RAS, Moscow)[217]	2 % ABIL EM90 0.05 % Triton X-100 97.95 % mineral oil	Encyclo polymerase	7.5 U PM 1x buffer 5 U MMLV RT 3.5 mM MgCl ₂ 1.4 mM DTT 0.5 mg/ml BSA 30 U RNasin 2.4 mM dNTPs 0.2 µM primer	106 PBMCs	Microfluidics	27	~400 bp	1 mM EDTA Diethyl ether Ethyl acetate Diethylether PCR clean up	cDNA and 1.PCR same step nested PCR with blocking primer (no droplets) emulsion like Griffiths
Kirschner, Mark (Harvard, US)[218]	3 M HFE-7500 fluorinated fluid 0.75 % EA surfactant	Only cDNA production	1x FS buffer 0.6 % IGEPAL CA-630 1 mM dNTPs 6.7 mM DTT 0.1 M Tris-HCl [pH8] 20 U/µl SSRTIII 150 µl volume	20'000 cells in 160 µl PBS 16 % Opti-Prep 0.05 % BSA	Microfluidics	2h 50 °C 15 min 70 °C 1 min on ice	cDNA only	1 volume PFO solution (20% perfluorooctanol, 80 % HFE-7500)	cDNA synthesis only
Zhao, Jianlong (CAS, Shanghai)[63]	3% ABIL EM 90 0.1% Triton X-100 96.9 % mineral oil	FASTSTA RT Taq polymerase	qPCR MIX: 1x LightCycler 480 Probe Master 0.5µM primer 0.15 µM FAM probe 0.1 µM VIC probe	<i>E. coli</i> genomic DNA	Microfluidics	35		No breakage	qPCR fluorescent detection

PI	Mineral oil used	Polymerase system used	PCR MIX	Tem-plate	Droplet generation	Cycles	PCR length	Droplet break-age	Comments
Weitz, DA (Cam-bridge, UK)[219]	Fluorinated oil: HFE-7500 (3M) 1% Krytox-PEG di-block co-polymer surfactant	0.5 µL of SuperScript III RT/Platinum Taq High Fidelity Enzyme	1x reaction buffer (Invitrogen, NY) 200 µM dNTPs 0.2 µM primers, 0.08x EvaGreen, 0.2 µg/µL BSA 0.2% Tween 20.	1 µL of purified RNA	Micro-fluidics	55 °C 30 min 94 °C 2 min 40 cycles	~1.5 kbp	No breakage	Sorted fluorescent PCR
Georgiou, George (UT Austin, US)[220]	4.5 % Span 80 0.4 % Tween 80 0.05 % Triton X-100 95.05 % mineral oil	qScript Fast One-Step RT-PCR Master Mix	Lysis buffer: 100 mM Tris pH 7.5 500 mM LiCl 10 mM EDTA 1 % Lithium dodecyl sulfate 5 mM DTT RT-PCR MIX: 0.4 µM primer 0.5 µg/ml BSA 1x qSCRIPT ONE-STEP RT-PCR Mix 0.8 U/ml RNase inhibitor 1x qScript RT	100'000 cells/ml PBS 45 µl poly(dT)/100'000 cells (wash and put in equal volume)	Micro-fluidics	30 min 55 °C 4x 50 °C 4x 55 °C 32x 60 °C	850 bp	Hydrated ether	The first step only capture mRNA Nested PCR with pool

4.2 One drop at a time: high-throughput nucleic acid assays

4.2.1 Single-molecule genomic screening

Droplet digital PCR (ddPCR) is almost certainly the most important microfluidic technology to have been commercialised in recent years (Figure 4:4b)[155], and refines the concept of digital PCR (dPCR) proposed in the late 1990s[221]. Unlike conventional quantitative PCR (qPCR) methods, dPCR achieves quantitation by portioning a large sample volume into many smaller volumes that statistically contain no more than one copy of target DNA. dPCR is particularly robust for the detection of rare nucleic acid samples, the investigation of rare mutations in complex backgrounds and the identification of small differences in expression levels.

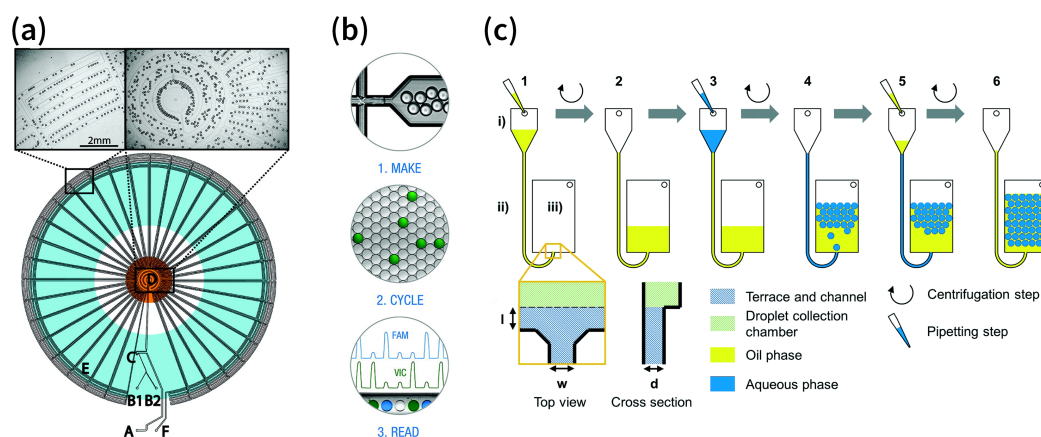


Figure 4:4 (a) Design of a radial PCR device. The device contains an oil inlet A that joins two aqueous inlet channels B1 and B2 to form droplets at a T-junction C. The droplets pass through the inner circles (500 μm wide channels) in the hot zone D to ensure initial denaturation of the template and travel on to the periphery in 200 μm wide channels where primer annealing and template extension occur E. The droplets then flow back to the center, where the DNA is denatured and a new cycle begins. Finally, the droplets exit the device after 34 cycles F. Adapted from reference [96] with permission. (b) ddPCR enables the absolute quantitation of nucleic acids from a sample in a high-throughput. The process includes three steps: on-chip droplet generation, off-chip droplet incubation and on-chip detection of fluorescence. Adapted from reference [155] with permission. (c) Workflow of centrifugal step emulsification without associated dead volumes. The system is located on a spinning disk and consists of an inlet chamber (i), a channel (ii) which connects the inlet to a nozzle, and a droplet collection chamber (iii). The inlet chamber is located closer to the centre of rotation than the droplet collection chamber and both chambers are equipped with an air vent. *Step 1*: the inlet chamber is filled with oil. *Step 2*: during centrifugation, the oil flows to the radial outer droplet collection chamber. *Step 3*: a sample is introduced to the inlet. *Step 4*: the sample is emulsified during centrifugation by step emulsification, and some sample remains in the inlet channel. *Step 5*: oil is filled into the inlet. *Step 6*: during centrifugation, the oil flows to the droplet collection chamber pushing the remaining sample through the nozzle which enables the production of droplets with zero dead volume. Adapted from reference [222] with permission.

That said, early embodiments of dPCR were limited by the method of sample partitioning, which often involved the use of microtiter plates[221], bulk emulsions (using beads, emulsion, amplification and magnetics—BEAMing)[223] or microfluidic chamber arrays[224]. Hindson and co-workers have compared ddPCR with qPCR in the microRNA quantification[225], with results indicating that ddPCR yields significantly greater precision and improved “day-to-day reproducibility” over qPCR. Such superior metrics suggest that ddPCR will continue to play an important role in molecular diagnostics of genetic diseases[226], cancers[227, 228], infectious diseases[63, 229] and prenatal diagnosis[230]. For example, epidermal growth factor receptor (EGFR) mutation is an important target for many cancer therapies, with the status of the EGFR mutation being closely related to the therapeutic effect of EGFR inhibitors, such as monoclonal antibodies and tyrosine kinase inhibitor[231,

232]. Siravegna *et al.* comprehensively combined BEAMing, ddPCR, NGS and bioinformatics analyses to genotype colorectal cancers and dynamically monitor clonal evolution during treatment with the EGFR-specific antibodies Cetuximab and Panitumumab[233]. Results revealed the colorectal tumour genome adapts dynamically to intermittent drug schedules, and provides a molecular explanation for the efficacy of “rechallenge therapies” based on the EGFR blockade. Such a methodology has significant implications for the development of personalised cancer treatments and the dynamic monitoring of disease progression and response to therapy. Put simply, it eliminates the difficulties associated with repeated sample acquisition, and removes temporal and spatial bias in sample selection.

ddPCR allows for the simultaneous detection of multiple targets through the use of multi-colour detection schemes, with further expansion of target numbers being achieved by varying parameters that control PCR efficiency[234]. Accordingly, in multiplex ddPCR, multiple mutations can be detected in a single experiment; a feature particularly valuable when assaying clinical samples[235]. Much work has recently focused on improving ddPCR, in terms of detection sensitivity[236] and sample volume limitations[237], but there is little doubt that ddPCR is rapidly becoming a “standard” component in highly sensitive genomic screening.

4.2.2 Single-cell genomic and transcriptomic investigations

Cells are the elementary structural, functional, and biological units in living organisms, with the physiological functions of multicellular organisms being realized through individual cells. It is widely acknowledged that a seemingly homogeneous cell population will differ significantly in terms of size, genetic variants and expression patterns at the single-cell level, resulting from the inherent stochasticity of biological processes[238] and stimulation by the external microenvironment[239]. Accordingly, the ability to identify cell-to-cell variations within a given population is critical in understanding clonal evolution in cancer[240], immune dysfunction[241] and somatic mutations[242]. In this respect, single-cell genomics aims to enrich our understanding of genetics by engendering the study of genomes at the cellular level.

A technical prerequisite for DNA or RNA sequencing of single cells is the efficient physical isolation of large numbers ($>10^3$) of discrete cells, in a manner that allows each cell to be interrogated on an individual basis[243]. Normally, cells obtained from blood or solid tissues are processed (via methods such as enzymatic dissociation, density gradient centrifugation

and fluorescence-activated cell sorting) to yield a single-cell suspension, which is then delivered into the microfluidic system. Cell isolation in microfluidic systems can be most easily achieved using traps, droplets or micromechanical valves. For example, the commercially available *Fluidigm C1* platform provides an integrated and automated solution for single-cell genomics, leveraging control of pneumatic valves (that deflect under pressure to disrupt fluid flow within a microchannel) to perform single-cell capture, lysis, mRNA release, RT-PCR and cDNA amplification. Such an approach allows the parallel analyse up to 800 cells in an automated fashion.

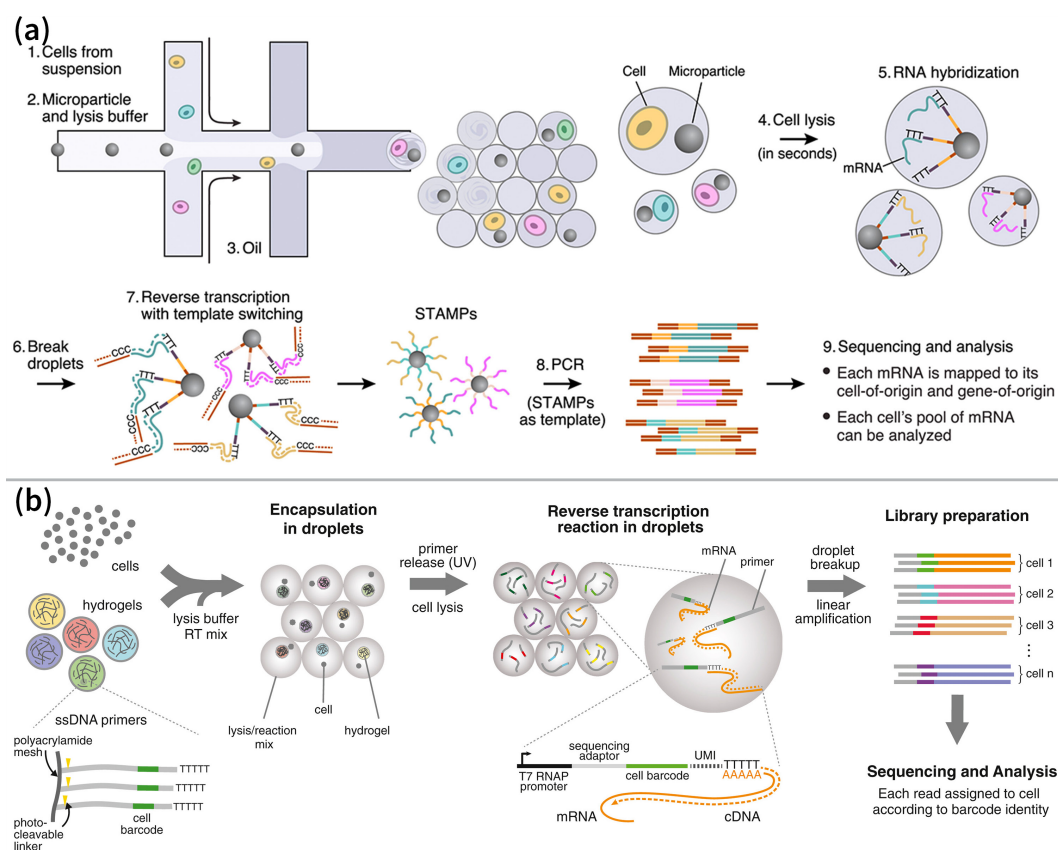


Figure 4:5 (a) *Drop-seq*. A custom-designed microfluidic device joins two aqueous flows before their compartmentalization into discrete droplets. One flow contains cells, and the other flow contains barcoded primer beads suspended in a lysis buffer. Immediately following droplet formation, the cell is lysed and releases its mRNAs, which then hybridize with primers on the microparticle surface. The droplets are broken by adding a reagent to destabilize the oil-water interface, and the microparticles collected and washed. The mRNAs are then reverse-transcribed in bulk, forming STAMPs (single-cell transcriptomes attached to microparticles), and template switching is used to introduce a PCR handle downstream of the synthesized cDNA. Adapted from reference [244] with permission. (b) *In-Drops*. Cells are encapsulated into droplets with lysis buffer, reverse-transcription mix, and hydrogel microspheres carrying barcoded primers. After encapsulation primers are released. cDNA in each droplet is tagged with a barcode during reverse transcription. Droplets are then broken and material from all cells is linearly amplified before sequencing. UMI = unique molecular identifier. Adapted from reference [218] with permission.

Two recent studies describing single-cell RNA sequencing methods using droplet-based microfluidics (termed *Drop-seq*[244] and *In-Drop*[218]) have attracted significant attention in the biological community due to their ability to barcode RNA and analyse mRNA transcripts in an efficient, cost-effective and high-throughput fashion (Figure 4:5). Unsurprisingly, these two approaches share much similarity in methodology, since they exploit droplet-based tools developed in the Weitz laboratory at Harvard University. Both utilise microfluidics to load single cells and single microbeads (containing a unique barcode) together with lysis buffer into droplets. Subsequently, released mRNAs from a given cell are labelled with a unique code prior to droplet breakup and pool amplification. mRNAs are converted to cDNAs by RT-PCR, followed by library preparation, sequencing and data analysis. Critically, all sequencing data, though carried out in batch, can be traced back to its “cell-of-origin” and “gene-of-origin”. The *Drop-seq* method uses solid microparticles, with oligonucleotide codes covalently linked to the particle surface, whilst *In-Drop* technology uses hydrogel beads, with code release being driven by UV activation. For the interested reader, a more detailed comparison of the biochemical procedures (including transcript coverage) can be found elsewhere[245]. That said, from a technical perspective, some comment on co-encapsulation efficiencies is worthwhile. Random (passive) loading of beads, cells and DNA molecules into droplets obeys Poisson statistics under normal circumstances[246]. To ensure a >95% probability that a given droplet contains no more than one cell, the average occupancy should not be larger than 0.1 cells per droplets. Under such conditions, most droplets (90.5%) will be empty, with 9% containing a single cell. Accordingly, both *Drop-seq* and *In-Drop* utilise dilute cell suspensions to ensure single-cell encapsulation, whilst leveraging the ability of microfluidic droplet generators to make droplets at high speed. Interestingly, the *In-Drop* method utilises close-packed ordering[171] to beat Poisson constraints, with almost 100% droplets receiving gel beads, and over 90% of cell-loaded droplets containing exactly one cell and one bead. This approach involves the use of close packed, deformable particles to allow insertion of a controllable number of particles into every droplet. It should also be noted that the basic *Drop-seq* methodology could in future make use of inertial focusing and ordering to drastically increase the number of droplets containing a single cell and bead[247]. Considering current co-encapsulation efficiencies, the *In-Drop* methodology should be well-suited for clinical applications, where cell availability is often limited. Interestingly, 10X Genomics have recently tested single-cell RNA-seq on their *GemCode* platform using similar workflows, and reported a cell capture efficiency of ~50% and the analysis of 8 samples in parallel[248].

Besides global single-cell RNA-seq, the principle of bead-barcoding and droplet-isolation has also been used for targeted transcriptomic sequencing. As noted, DeKosky *et al.* sequenced

immune receptor repertoires with the preservation of pairing information (between heavy and light chain antibodies)[195, 196]. These chains contain variable domains and their pairing relationship controls cellular functionality. Compared to *Drop-seq*, an additional step of re-emulsifying mRNA-captured beads to perform RT-PCR and linkage PCR is necessary. In this respect, the authors have recently published a detailed protocol of the entire workflow[220].

The encapsulation and isolation of single cells in a drop-by-drop fashion has opened up new opportunities for cost-effective and ultra-high-throughput single-cell genetic studies in applications such as whole-genome amplification[249], chromatin profiling[250] and PCR-activated cell sorting[251], with microfluidically-produced droplets playing a key role. Finally, it is worth noting that thermosensitive hydrogel droplets are interesting vehicles for novel experimentation[252, 253]. For example, hydrogel droplets can be generated in oil at elevated temperatures and cooled to form gel particles downstream. These gel particles can then be washed and handled in aqueous buffer, allowing molecular exchange of substances through diffusion. Hence, unlike conventional aqueous droplets that require sophisticated operations to dose or remove reagents, gel droplets may be processed by immersion in appropriate media or dialysate. This innovation has opened up new possibilities for designing highly complex biological workflows in genetic analysis[254–256].

Chapter 5 High-throughput profiling of antigen-specific T cell receptors using droplet-based microfluidics

The rapid and low-cost identification of tumour-specific T cell receptors (TCRs) from individual patients is an important yet demanding challenge, requiring the analysis of tens of thousands of single cells to preserve the linkage relationship between TCR sub-chains. Importantly, if successful, the identified tumour-reactive TCRs can be grafted onto autologous T cells for a range of immunotherapy applications. Herein, we propose and describe a droplet-based workflow for the high-throughput extraction of TCR pairs and identification of the entire TCR repertoire of hepatocellular carcinoma patients.

5.1 Introduction

Cancer, a cellular disease, is one of the most significant health issues facing mankind. For example, in 2012, there were 14.1 million new cases of cancer and 8.2 million deaths due to cancer. The World Health Organization (WHO) projects that by 2035, these numbers will increase to 24 million new cases and 14.6 million deaths worldwide. Cancer originates from gene mutations in a small number of regular cells in the body. Normal regulations of gene expression fail in cancer cells, resulting in an uncontrollable growth. Cancer cells can escape from the immune surveillance, and ultimately, invade and spread to other locations (via metastasis). Tumours are commonly classified according to the site of occurrence, *e.g.* lung cancer, hepatic carcinoma. Such classification is convenient, but does obscure the enormous diversity of tumour cells. Tumour cells can be derived from almost any type of normal cell. with the status of a single tumour cell within a tissue being distinguished through levels of gene expression and molecular immunology[257, 258]. For this reason,

the development of a general therapy to effectively and specifically suppress the growth of tumour cells is extremely difficult.

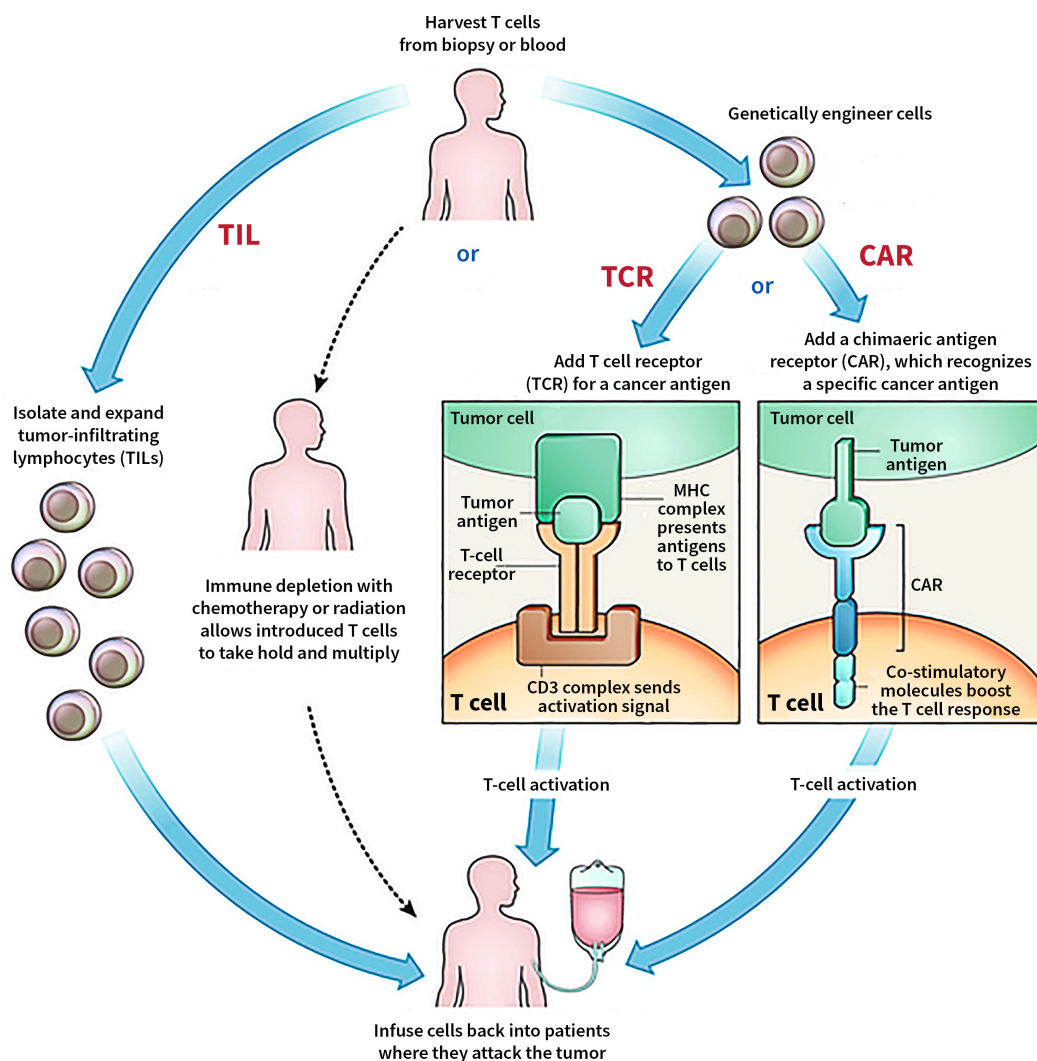


Figure 5:1 Three general approaches of adoptive cell transfer therapy. Adapted from reference [259] with permission.

That said, recent clinical studies have demonstrated a significant potential of adoptive cell transfer (ACT) therapy in the treatment of melanoma[260, 261]. ACT therapy leverages the power of the immune system by enhancing the autologous T cells. To date, there are three main approaches for engineering T cells (Figure 5:1)[259]. These are tumour-infiltrating lymphocytes (TIL) therapy, T-cell receptor (TCR) therapy and chimeric antigen receptor (CAR) therapy. The latter two (TCR and CAR) improve the specificity of tumour recognition by T cells through genetic modification. Such “engineered” T cells form a new configuration that expresses TCRs or CARs able to recognise cancer cells.

Though highly promising with many iterations and refinements of the technique made in recent years, ACT therapies are not yet efficient in identifying TCRs able to recognise tumour-specific mutations. Accordingly, in this chapter, we aim to establish an improved strategy for the rapid and low-cost identification of tumour-specific TCRs from TILs, with a specific focus on hepatocellular carcinoma (HCC), the second leading cause of cancer deaths worldwide[262]. If successful, the impact of such a platform technology will be significant. Indeed, identified TCRs from a patient could be grafted to autologous, non-exhausted T cells (TILs are often exhausted and lose their ability to attack tumour cells), massively expanded *in vitro* and then reintroduced into the patient's body. Although the therapeutic effect of ACT is currently limited to the treatment of solid tumours (*e.g.* sarcomas, carcinomas and HCC) due to physical and metabolic barriers (*i.e.* tumour vasculature and stromal barriers)[263], patients will still immediately benefit through the prevention of tumour recurrence after resection. In this context, HCC is amenable for immunotherapy, with clinical studies demonstrating that the infusion of *ex vivo* expanded autologous T cells decreased post-surgical recurrence of HCC by at least 18%[264].

5.2 Workflow and Methods

5.2.1 Design of the microfluidic workflow

TCR is a protein that exists in the membrane of T cells and is responsible for recognising antigens[265]. It is a heterodimer, consisting of two different transmembrane protein chains (α - and β -chain in most cases, with a small portion of $\gamma\delta$ chains) as shown in Figure 5:2a. In a similar manner to other proteins, TCRs are encoded and expressed by mRNAs and can be indirectly profiled at a transcriptome level. The polyadenylated (poly(A)) tail, allows mRNAs to be universally captured and primed by a complementary oligo(dT) based structure, such as those found on oligo(dT) surface-modified beads (Figure 5:2b). The linkage relationship between TCR chain pairs is critical for TCR functionality and its immune response to antigens[266]. Accordingly, the task of profiling the TCR repertoire requires the development of high-efficiency tools for performing large numbers of experiments at the single cell level.

α - and β -chains of TCRs are encoded by TRA (T-cell receptor alpha) and TRB (T-cell receptor beta) respectively with both TRA and TRB containing two domains, *i.e.* a variable (*V*) and a constant (*C*) domain. Amplification-based strategies allow the conversion of mRNAs associated with TRA and TRB to the corresponding complementary DNAs (cDNAs)

through reverse transcription (RT). Subsequently, the two fragments of a cDNA can be linked together (using linker PCR) by the rational design of a set of (overlapping-) primers for the *V* and *C* regions.

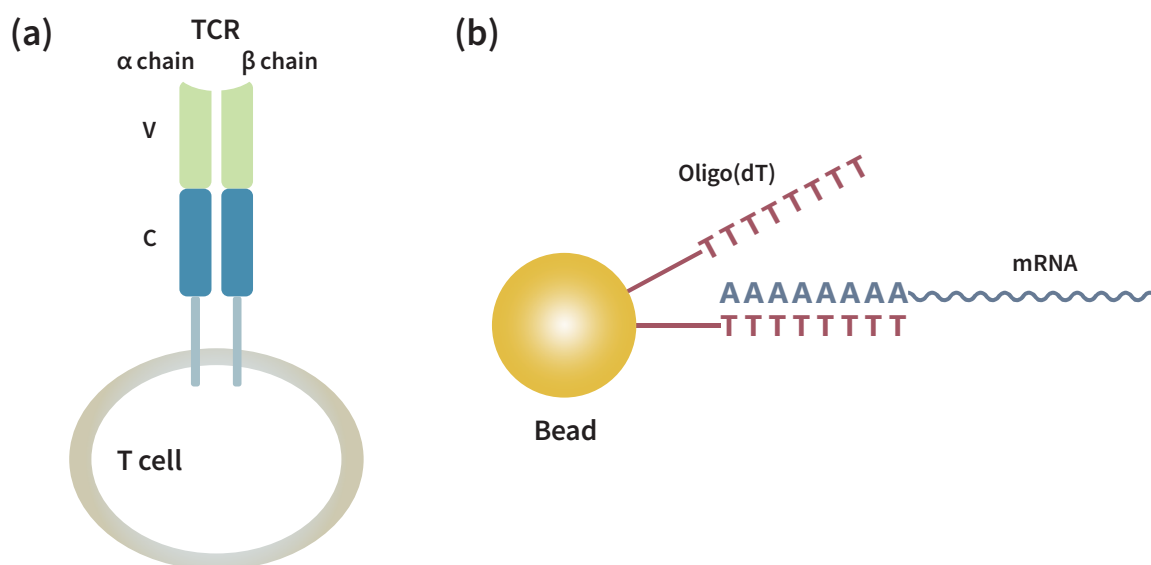


Figure 5:2 (a) The structure of a T-cell receptor (TCR). The TCR consists of two chains with each chain having a *V* domain and a *C* domain. (b) Universal mRNA capture by an oligo(dT) modified bead. mRNA has a poly(A) tail which is conjugated to oligo(dT).

The general process for obtaining linkage TCRs is well defined, *i.e.* mRNA is captured and converted to cDNA. TRA and TRB are then selectively amplified and linked. Importantly, each step can be completed via several well-established routes. The critical challenge throughout the workflow is to preserve information originating from single cells. In this regard, key questions include how to establish reliable boundaries (partitions) for single cells, how to coordinate the partition strategy with the biochemical process and how to make the whole process both efficient and fast. As discussed in Chapter 4, droplet-based microfluidic systems are powerful tools for high-throughput single cell experimentation. Accordingly, we designed a workflow integrating droplet-based microfluidic and bead-based technologies (Figure 5:3). In the first step, T cells are co-encapsulated with oligo(dT) beads. The cells are lysed, with mRNA being released and then captured on the beads. In the second step, cDNA is synthesised. Specifically, droplets are broken, and beads are collected. RT is then used to convert mRNAs to cDNAs. In the final step, linker PCR is performed. This involves re-encapsulation of single beads into droplets, and amplification and linkage of TRAs and TRBs.

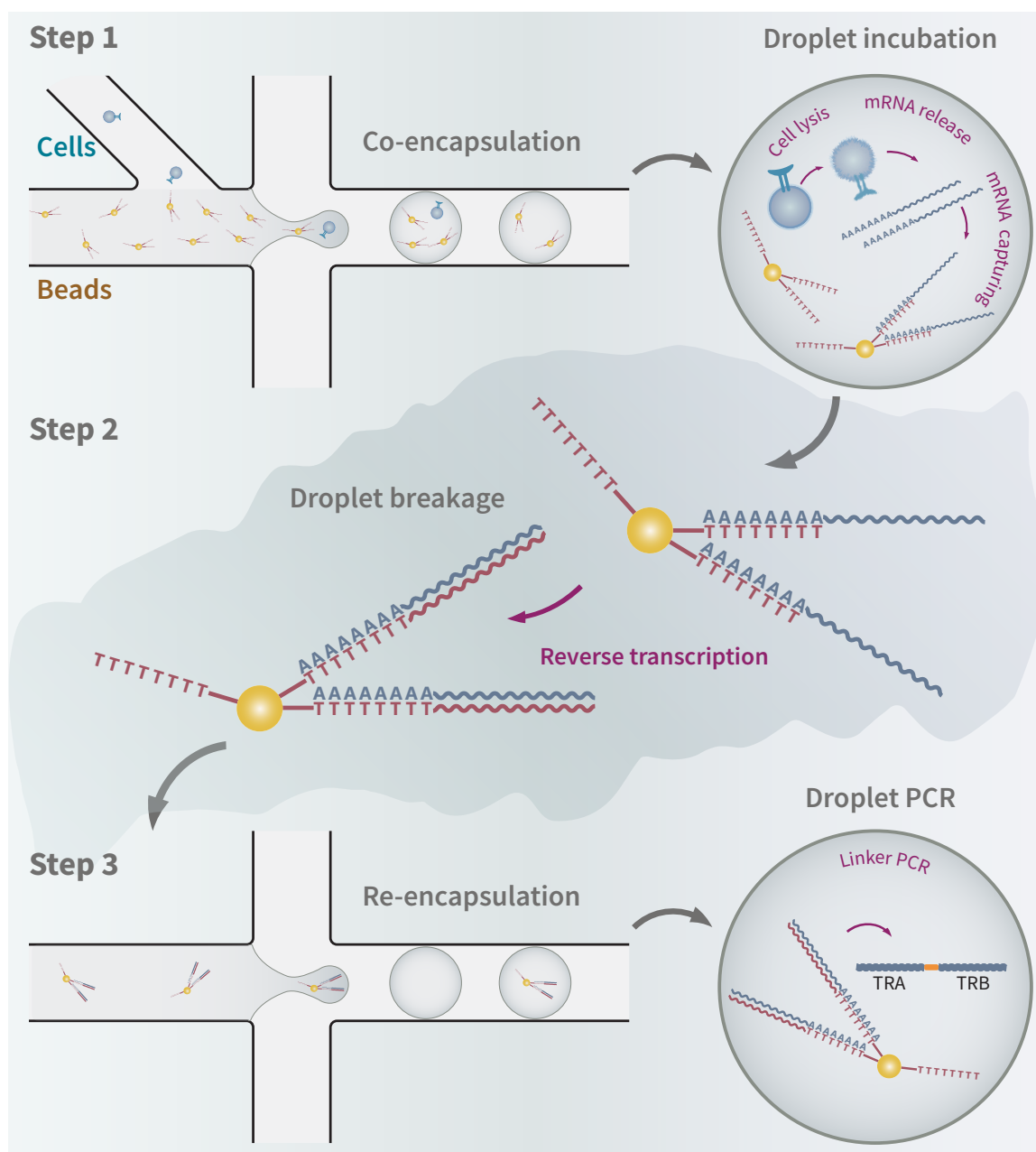


Figure 5:3 Microfluidic workflow for extracting linkage TCR receptors. *Step 1*, T cells and beads (with a lysis buffer) are co-encapsulated within microfluidic droplets. The concentrations of cells and beads are adjusted so that each droplet contains at least one bead, but no more than one cell, assuming Poisson statistics (see Section 1.4 in Chapter 1). Cells are then lysed in droplets, mRNAs released and subsequently captured on beads. *Step 2*, involves the breakage of droplets, collection of beads and performance of RT to convert the captured mRNAs into cDNAs. *Step 3*, re-encapsulation of single beads into droplets together with linker PCR reagents. TRAs and TRBs can then be amplified and linked within droplets.

5.2.2 Microfluidic device and fabrication

Step 1 and *step 3* within the above workflow define microfluidic procedures able to share a microfluidic chip design for a given bead size (1 μm , 10 μm and 30 μm in the current experiments). Whilst the dimensions of the microfluidic channels are slightly different depending on the size of beads used, all have the same key elements. Each device comprises two aqueous inlets (for cells and beads respectively), an oil inlet and a droplet outlet. Droplets are formed at a flow-focusing geometry. In *step 1*, both inlets are used, whilst in *step 3*, the “cell” inlet is blocked, with the aqueous phase containing only beads. The specific microfluidic design used for experiments with 10 μm diameter beads is shown in Figure 5:4. Microfluidic devices were made in PDMS and manufactured by standard soft lithography, as described in Chapter 2. Additionally, and to enhance the fluorophilicity of the channel surface, all the channels were treated with 20 % perfluorooctanol/isopropanol (w/w) before use.

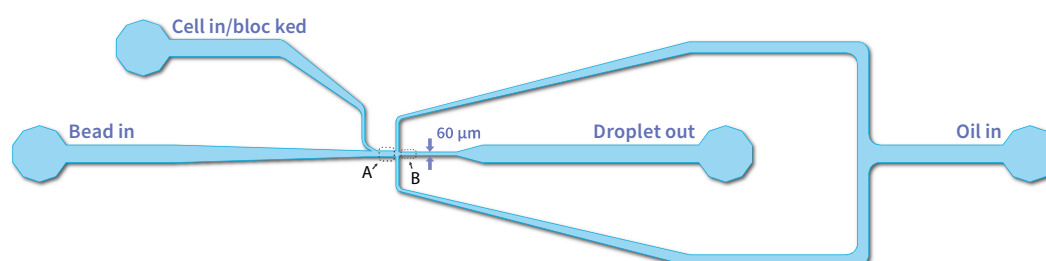


Figure 5:4 Microfluidic device design for experiments with 10 μm diameter beads. The height of all microfluidic channels is 70 μm . The structure comprises an oil inlet, a bead inlet, a cell inlet (not used in *step 3*). The width of channel in area A is larger than that in area B. The wider channel in area A facilitates a uniform and smooth loading of beads. The channel width in area B is a crucial factor for the size of droplets.

5.2.3 Cell cloning

A mixed population of T cell clones were used to establish and develop the experimental workflow. The population included three sub-groups of human T cells, namely memory CD4^+ T cells with unknown TCR-sequences, native CD4^+ T cells with known TCR-sequences but unknown specificity, and influenza-specific Tfh CD4^+ T cells with known TCR-sequences. Additionally, the proportion of each cell clone in a mixture is measured to aid in the assessment of the accuracy of TCR linkage afterwards by sequencing. The role of known TCR-sequences with known proportion are similar to internal standard in analytical chemistry.

5.2.4 Reagents and materials

For all droplet-based experiments, the continuous phase consisted of HFE-7500 fluorinated oil (3M Novec, USA) with 2% (w/w) surfactant (008-FluoroSurfactant, RAN Biotechnologies, USA). This composition provided for both efficient droplet generation and droplet stabilization. The reagent used for droplet breakage consisted of a 20% (v/v) 1H,1H,2H,2H-Perfluoro-1-octanol (Sigma-Aldrich, Switzerland) solution in HFE-7500.

All the beads tested (average diameter 1 μm , 10 μm and 30 μm respectively, ordered from Sigma-Aldrich, Switzerland) were polymer-based with oligo d(T)₂₅ coated on the surface. Specifically, the support material of 10 μm beads is carboxyl-polystyrene with 30 μm beads being hydroxylated methacrylic polymer. The data of specific type of polymer for 1 μm beads is not found.

The bead buffer (for cell lysis, pH 7.5) used in *step 1* contained 5 mM DTT (dithiothreitol), 10 mM EDTA (ethylenediaminetetraacetic acid), 100 mM Tris (tris(hydroxymethyl)aminomethane), 500 mM LiCl (lithium chloride) and 1 % (w/v) IGEPAL CA-630 in nuclease-free water. All the components of lysis buffer were purchased from Sigma-Aldrich, Switzerland.

The reagent for cDNA synthesis was prepared in nuclease-free water and contained 1 \times First-Strand buffer, 900 nM dNTPs (deoxynucleotide triphosphates), 1 \times NP-40, 10 mM DTT, 0.84 U RNasin and 2 U/ μl SuperScriptIII RT. This was subsequently used at ~1 million beads/100 μl reagent. The reagent for linker PCR was similarly prepared in nuclease-free water and contained 250 nM dNTPs, 200 nM TRA primer mix, 200 nM TRB primer mix, 200 nM TCR primer mix, 0.1 U/ μl PfuUltra II, 1 \times PfuUltra II buffer and 0.1 mg/ml BSA (bovine serum albumin, ordered from Sigma-Aldrich, Switzerland). This was used at ~100,000 beads/100 μl reagent. Unless otherwise specified, all the bioreagents were purchased from Invitrogen, Thermo Fisher Scientific, USA.

5.3 Results and Discussion

5.3.1 Co-encapsulation

Initial experiments were focused on elucidating experimental parameters that would allow the reliable and efficient co-encapsulation of T cells and beads. To maximise the number of encapsulated cells that are able to access beads for mRNA capture, conditions should

be established in which at least one bead is present in a droplet containing a single cell. This requirement is of particular importance when analysing clinical samples, since the number of available sample cells from patients is often severely limited. For example, in one of our sample collections from 11 HCC patients, an average of 1.02 g tumour tissue per patient was obtained through resection surgery, yielding an average of 363,600 CD4 cells, 198,400 CD8 cells and 85,900 B cells isolated for analysis. Additionally, the average number of beads per droplet should be kept to a minimum so as to prevent mRNAs distributing over too many beads. As discussed in Section 1.4, this strategy assumes that droplet occupancies can be described using Poisson statistics. Put simply, the average number of beads per droplet should be maintained between 4 and 6, whilst the average number of cell per droplet should be kept below 0.1.

In practice, besides ensuring that appropriate numbers of beads and cells are loaded into droplets, successful co-encapsulation relies on other key factors. The first, relates to density matching of media and particles. Because the cells and beads used are denser than the surrounding fluid (buffer), they will tend to sink and precipitate in the both syringe and tubing before entering droplets. Such behaviour not only results in unpredictable and irreproducible encapsulation, but also increases the likelihood of channel blockage and terminal flow disruption. This issue can be addressed through the addition of appropriate amounts of OptiPrep™ density gradient medium (a sterile, endotoxin tested solution of 60% iodixanol in water having a density of 1.32 g/ml).

The second, relates to the size of channels, since a bottleneck (the smallest dimension within the microfluidic circuit) exists in the vicinity of the orifice where droplets are formed. Initial experiments (data not shown) suggested that the upstream side of the orifice (marked “A” in Figure 5:4) should have a channel width and height at least three times larger than the average diameter of the beads (10 μm and 30 μm in the current study). If not, channels become prone to blockage via bead accumulation at the orifice. That said, the downstream side of the orifice (marked “B” in Figure 5:4) may have narrower dimensions, which in turn aids generation of smaller droplets under given flow conditions. This is important, since smaller droplets are more stable and provide for enhanced mRNA captured on beads inside the droplet compartment. It should also be noted that in the case of 1 μm diameter beads, channel blockage is rarely observed, with the channel width and height being chosen based on the average cell size ($\sim 10 \mu\text{m}$).

The final issue is related to flow velocities. In simple terms, a large flow velocity assists avoidance of bead sedimentation and channel blockage, and also reduces experimental

timescales. However, high flow velocities enhance the possibilities of jetting[267], an unstable mode of droplet generation resulting the creation of non-uniform droplet volumes. To this end, calibration experiments (data not shown) indicated that such effects could be excluded if the flow velocity of the bead stream is kept between 1 and 10 cm/s.

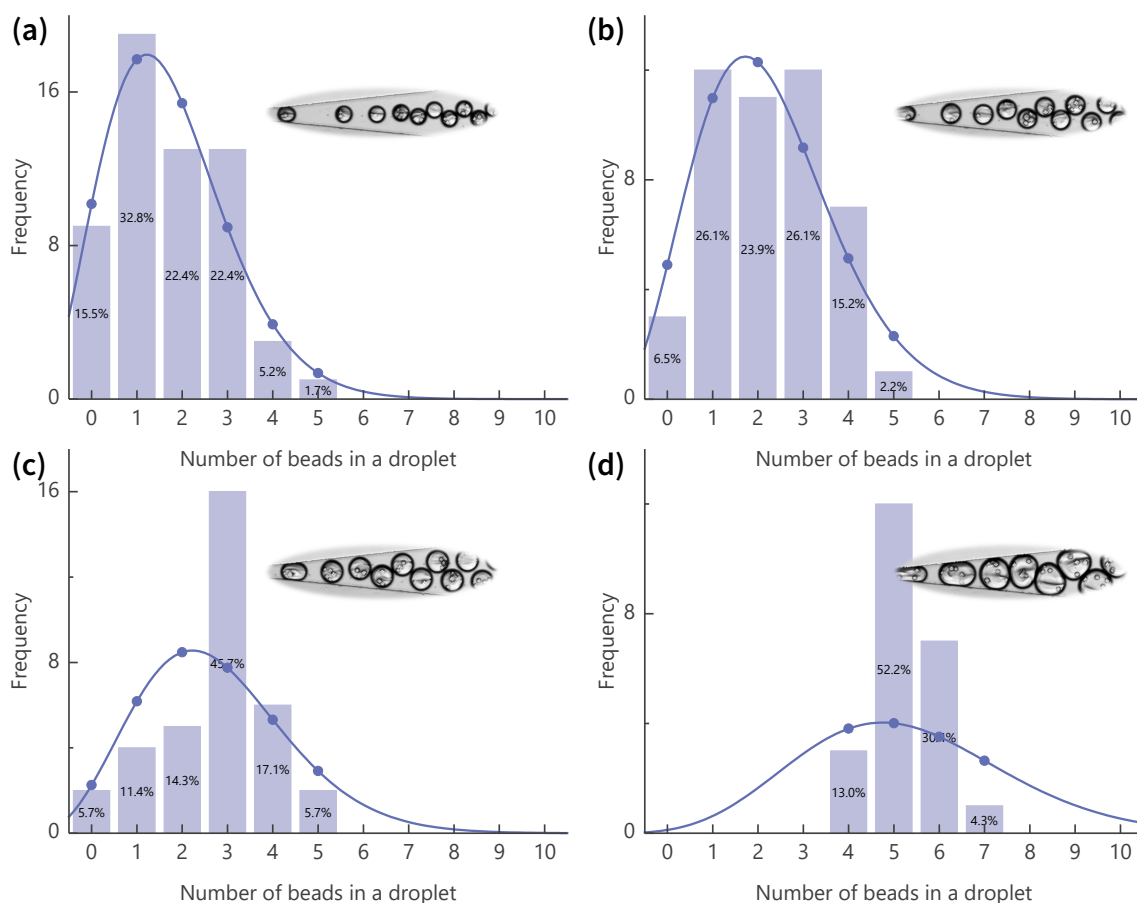


Figure 5:5 Bead occupancies are adjusted by controlling the relative flow rates of the aqueous and oil phases. From (a) to (d), the flow rate ratios between the aqueous and oil are 5, 2.5, 1.25 and 0.5 respectively. In (d), 100% observed droplets contain beads with $N = 5.26$. The curves are theoretical Poisson fitting according to the observed N .

Once the optimal microfluidic conditions were determined, *i.e.* channel size (controlling droplet size) and flow velocity (controlling the droplet generation frequency) and bead/cell concentrations) encapsulation can be further tuned through adjustment of the flow rate ratio between the aqueous and oil streams. In the current scenario, such a variation of the flow rate ratio has little impact on cellular occupancies, but does influence bead occupancies. The reason for this is that because the cell suspension ($N < 0.1$) is dilute with respect to the bead suspension ($N > 1$) Figure 5:5 shows the effects of flow rate ratio adjustments for the case of 30 μm beads. In each of the four experiments, the total flow rate of aqueous phase (*i.e.* the sum of the flow rates of the bead flow and cell buffer flow) was fixed, with

component flow rates being equal (providing for a superior hydrodynamic balance) and only the oil flow rate being varied. Under such circumstances, the average number of beads per droplet size increases as the oil-to-aqueous flow rate ratio decreases and at a flow rate ratio of 0.5, almost all droplets contain beads. It should also be noted that bead occupancy can be directly increased by simply using bead suspensions of higher concentration. Demonstration of such a strategy when using 10 μm diameter beads is described in Appendix C.1. That said, this approach is not especially convenient since it requires preparation of a new sample for each experiment, however, it is the only option to adjust encapsulation occupancy for a given droplet size in the current context. Based on these dependencies, co-encapsulation of both beads and cells was achieved and reported in Figure 5:6 (for 30 μm beads) and Figure 5:7 (for 1 μm beads), and representing a combination of both droplet size and sample concentration variations.

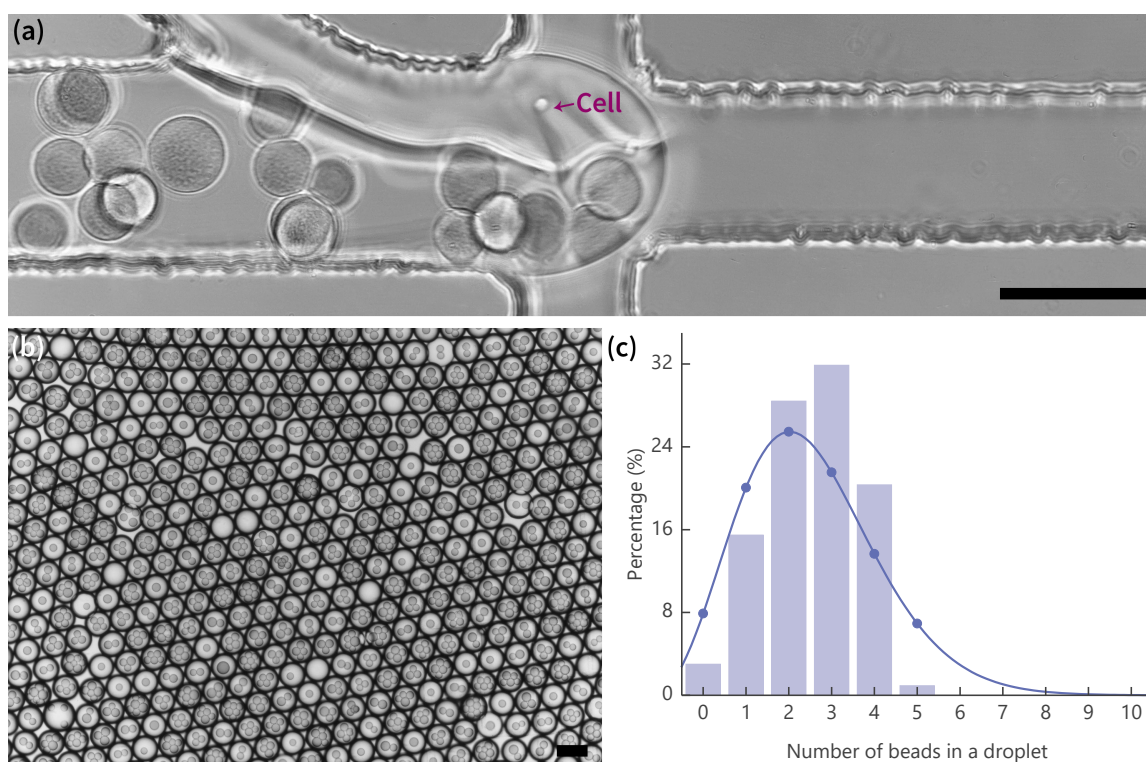


Figure 5:6 Co-encapsulation of cells and 30 μm beads. (a) The image shows single cells and beads at the point of co-encapsulation. (b) Image of a formed droplet population. Bead size distribution is 20 – 40 μm (>80% within range). The corresponding bead number distribution is shown in panel (c). The percentage of empty droplets is below 1.7%, with the average number of beads per droplet being 2.5. The solid curve represents the expected distribution based on Poisson statistics. Scale bars are 100 μm .

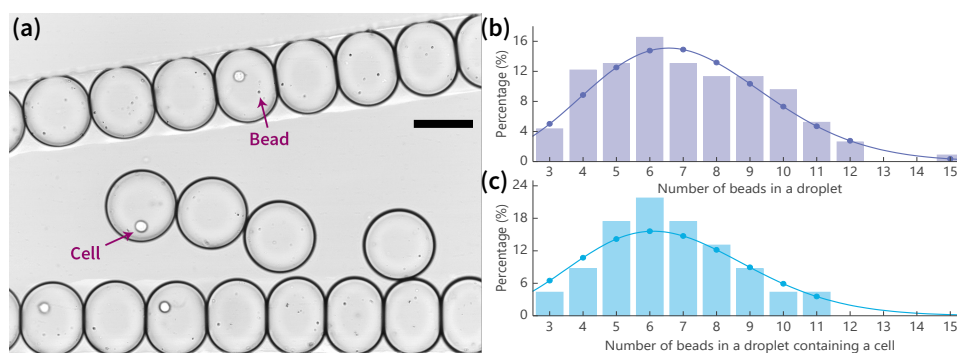


Figure 5:7 Co-encapsulation of cells and 1 μm beads. (a) The microscope image shows droplets containing both beads and single cells moving through a microfluidic device. White artefacts near the top and bottom of droplet trains are a consequence of image processing of background subtraction. The scale bar is 50 μm in length. (b) Frequency distribution of beads (columns). The solid curve represents the expected distribution based on Poisson statistics, $N = 7.0$. (c) Bead distribution for droplets containing a cell, with the solid curve representing the expected distribution based on Poisson statistics, $N = 6.6$.

5.3.2 mRNA capture and cDNA synthesis

After the establishment of an efficient co-encapsulation procedure, we attempted to verify the entire workflow using 1 μm beads. The first part of this process involves the capture of mRNAs on beads and subsequent conversion to cDNAs. As shown in Figure 5:8a, a mixture of T cell clones was co-encapsulated with 1 μm oligo(dT) beads in the microfluidic flow focusing junction. Specifically, cells were suspended in PBS buffer and density-balanced with additional OptiPrep™ density gradient medium, whilst beads were prepared in lysis buffer. Such an approach generated a population of droplets having an average diameter of 40 μm , with 12% of droplets containing a single cell and multiple beads (Figure 5:8b). Droplets were subsequently collected in a Falcon tube and incubated at 42 °C for 10 minutes to enhance both cell lysis and mRNA release, and then at 25 °C for 10 minutes to allow mRNA capture. The emulsion was then broken and the released beads washed, collected and stored at 4 °C until cDNA synthesis is performed (always within in 6 hours). Capture of mRNAs was verified by PCR, with details of the complete process being provided in Appendix C.2.

For proof-of-principle experiments, cDNA synthesis was performed in bulk. Beads were added with reagents into standard PCR tubes. The reaction mixture was subsequently subjected to the following thermal process: 10 minutes at 42 °C for denaturing, 10 minutes at 25 °C for annealing, 60 minutes at 50 °C for extending (cDNA synthesis) and an extended time period at 4 °C to finish. After conversion of mRNAs to cDNAs all beads were washed and then stored at 4 °C for a period of up to one week.

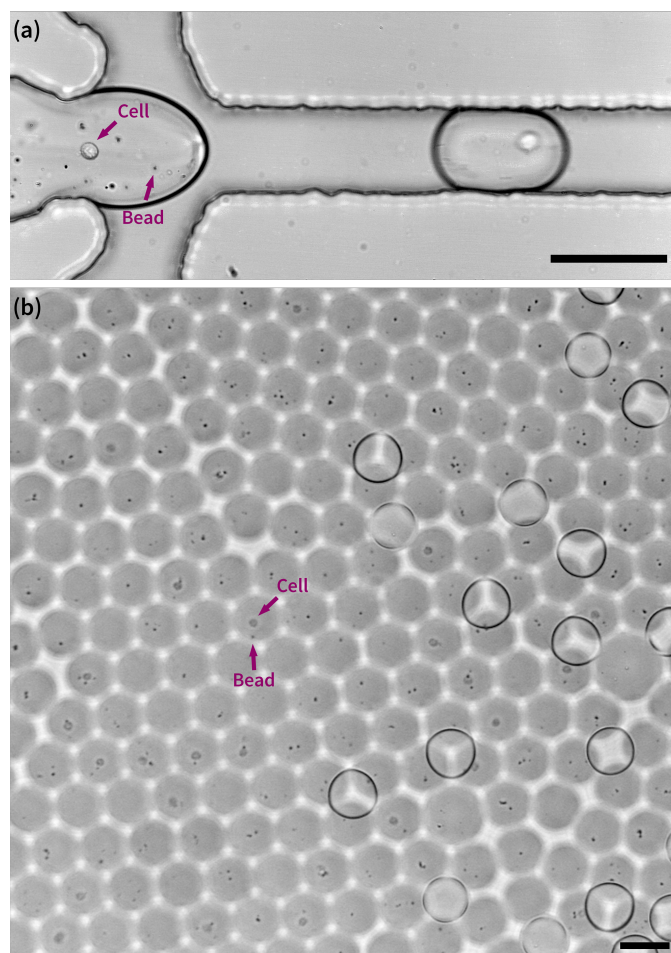


Figure 5:8 Co-encapsulation of T cells and 1 μm oligo(dT) beads within 35 pL volume droplets containing lysis buffer. (a) Image illustrating the process of droplet formation and co-encapsulation. Lysis buffer is introduced through the bead stream. It should be noted that the generated droplet in the image does contain beads. These are difficult to see due to the fact that the droplet is moving at high speed along the channel ($5.5 \text{ cm}\cdot\text{s}^{-1}$). (b) Image of droplets subsequent to production and collected in an off-chip reservoir for observation. For the population shown, 12% of droplets contain a single cell. Scale bars are 50 μm .

Additionally, we assessed the efficiency that beads are able to capture mRNAs, through both FACS (fluorescence-activated cell sorting) and fluorescence imaging. Approximately 40,000 beads (having an average diameter of 10 μm size, and oligo(dT)₂₅-coated) were washed with Tris buffer (0.1M, pH 8.0). These beads were evenly distributed into three samples containing different concentrations of Atto 647 linked d(A)₂₅ (0.01 ng/ml, 0.1 ng/ml and 1 ng/ml) and one sample only containing water. Samples were incubated at 42 °C for 15 minutes and then, beads were washed twice before analysis with FACS (Figure 5:9a). Results of detected fluorescence signal on beads confirm the capacity of beads for capturing mRNAs. Based on an analysis of the median fluorescence intensity (MFI) from the FACS data, bead sites are still unsaturated for Atto 647 linked d(A)₂₅ concentrations of 0.01 ng/ml (MFI value of beads increased from 1935 to 2037 when applying elevated

0.1 ng/ml). This capacity is more than sufficient for capturing mRNAs from single cells in the current experiments. In addition, two streams of bead suspension and 0.01 ng/ml ATTO 647 d(A)₂₅ were co-flowed at 1:1 ratio to form co-encapsulated droplets within a microfluidic channel. Imaging of the produced droplets allowed for indirect observation of mRNAs capture within in droplets (Figure 5:9b), confirming that beads can efficiently capture mRNAs within nL-volume droplets. Droplets containing beads had overall less fluorescence signal in background than that containing no beads. Meanwhile, beads showed stronger signal than background, which indicated fluorescence molecules (mRNAs) were concentrated on beads within droplets.

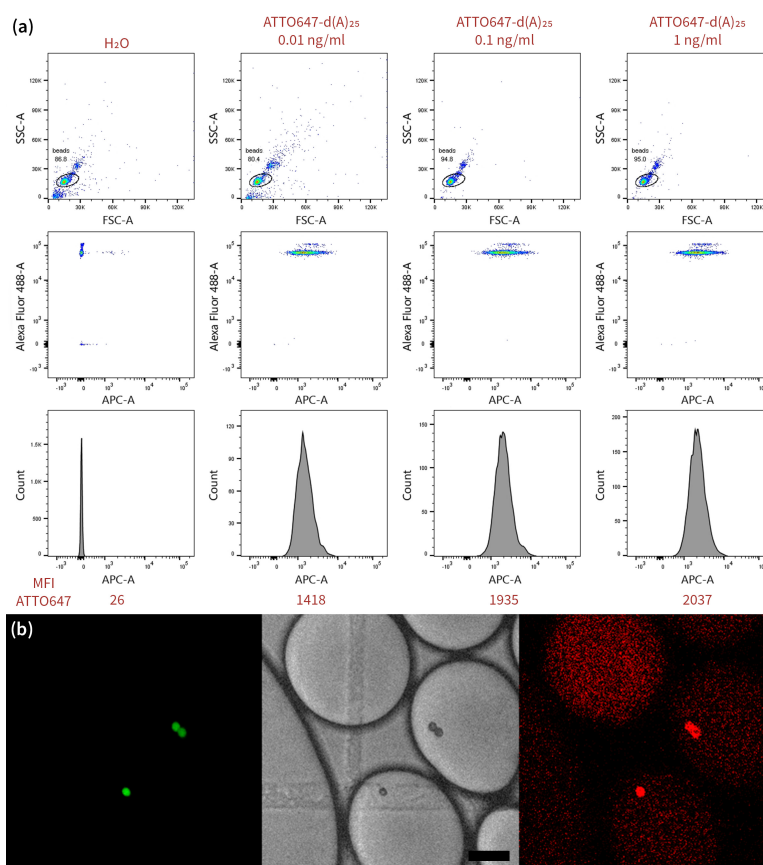


Figure 5:9 (a) Representative data assaying mRNA capture in bulk. Beads are flow-cytometry detected by BD FACSAria III. Figures in each column represent the results of a case using a specific concentration of ATTO647 d(A)₂₅ plus a water control. Figures in the first row are the distinction of beads from other impurity particles using parameters of SSC-A (side scatter pulse area, indicating the surface information, *i.e.* granularity, for the particle) and FSC-A (forward scatter pulse area, giving a relative size for the particle). Figures in the second row are further distinguishing beads by looking at green (note that beads are coated with FITC) and red (due to the captured ATTO 647) fluorescence signals. Figures in the third row are the number distribution of beads according to the detected intensity of red fluorescence signal (b) Fluorescence images reporting mRNA capture within droplets. Left panel shows a fluorescence image captured using a FITC fluorescein optical filter. The middle panel shows the corresponding bright-field image. The left panel shows the corresponding fluorescence image using an optical filter for ATTO 647. The scale bar is 50 μm .

5.3.3 TCR linkage

Once cDNAs (converted from mRNAs originating from a single cell) are universally captured on beads, the selective amplification and linkage of TRAs and TRBs from isolated beads becomes possible. Individual beads can be re-emulsified, and subsequently, millions of parallel TCR linkage PCR reactions can be performed within droplets.

To this end, beads were initially centrifuged to remove storage buffer and added to the linkage PCR reaction mixture. Importantly, the average number of beads per droplet was controlled to be approximately 0.1 based on Poisson statistics. The reaction mixture was then delivered into the microfluidic device (Figure 5:10a). As can be seen, highly monodisperse droplets ($\sigma < 1.8\%$) were formed with a 12% proportion of the droplets encapsulating a single bead (Figure 5:10b).

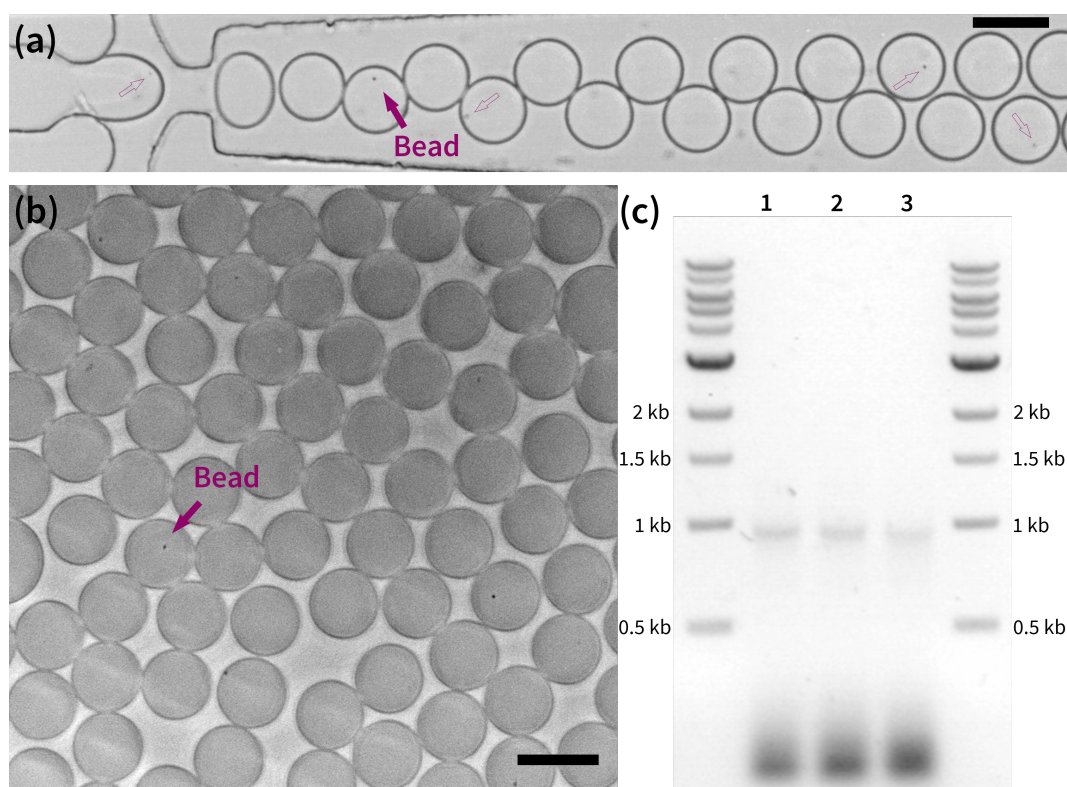


Figure 5:10 Droplet-based TCR linkage PCR. (a) cDNA-linked beads were encapsulated in 35 pL droplets at a flow focusing geometry. (b) Image of a droplet population collected in an off-chip reservoir, with approximately 12% droplets containing a single bead. Scale bars in panels (a) and (b) are 50 μm . (c) Gel electrophoresis of PCR products. Lanes 1 and 2 represent an analysis of products from droplet-based PCR, and with lane 3 representing the bulk PCR control. Expected bands for linker TCR PCR should occur at approximately 1 kb for single chains and between 1.5 and 2 kb for linked products. No bands were observed for the negative control (data not shown).

Droplets were subsequently collected in PCR tubes and thermally cycled. Specifically, droplets were subjected to 45 cycles of 95 $^{\circ}\text{C}$ for 20 seconds, 55 $^{\circ}\text{C}$ for 20 seconds and 72 $^{\circ}\text{C}$

for 90 seconds. It should be noted that in the current experiments the reaction buffer (PfuUltra II buffer) negatively impacted droplet stability. To counteract this and more generally Ostwald ripening[64], care should be taken (during the droplet generation process) to ensure that droplets exhibit narrow size distributions and an average diameter less than 100 μm . A more detailed analysis of this issue can be found in Appendix C.3. After PCR, the emulsion was broken and the reaction products collected. Gel electrophoresis was used to verify the target DNA products (Figure 5:10b). In these proof-of-principle experiments, TCR PCR can be seen to provide with good efficiency, since the single chain bands are clearly evident in both samples. However, the band reporting linkage chains is current too faint to see. Additional strategies are essential to improve the efficiency of TCR linkage.

5.4 Further improvements and next steps

Based on the experiments described in this chapter, we are currently developing two approaches that will allow the generation of sufficient linkage products. The first, recognises that the initial co-encapsulation strategy is inefficient. The majority of beads that are processed through the microfluidic device (over 90%) are redundant, since they are located in droplets that do not contain a cell. Besides, mRNAs of TCRs from a single cell spread to multiple beads (occurs in droplets containing a cell). This dramatically reduces the chance that a TRA and TRB will be simultaneously captured on a bead, since the abundance of TCR mRNAs within a cell is typically low; on average ~ 10 per cell[268]. To solve this issue, additional microfluidic tools can be used to obtain droplets containing exactly one bead and one cell. Such procedures are schematically shown in Figure 5:11. Here, diluted samples of cells and beads (both of which are fluorescently labelled, with the bead sample containing a lysis buffer) are initially and separately encapsulated into droplets according to Poisson statistics. These procedures generate two droplet streams; the first made up of droplets which are either empty or contain one cell, and the second made up of droplets which are either empty or contain one bead. A fluorescence-activated droplet sorting module[165] can be used to manipulate and collect only droplets containing a cell or bead. Subsequently, droplets in the two synchronized streams can be paired and merged (using a variety of strategies developed by deMello and co-workers[31]) to form a larger droplet that contains exactly one cell and one bead[59]. Once merged, cells are immersed in the lysis buffer (coming from the bead droplet), and subsequently released mRNAs will be captured on a single bead. Another potential option to achieve 1:1 pairing of single cells and beads is using technology of inertial microfluidics[247, 269]. This method is in a direct

fashion. However, preliminary tests shows intermittent jetting occurs during the generation of droplets as the flow required to run at a significant higher rate.

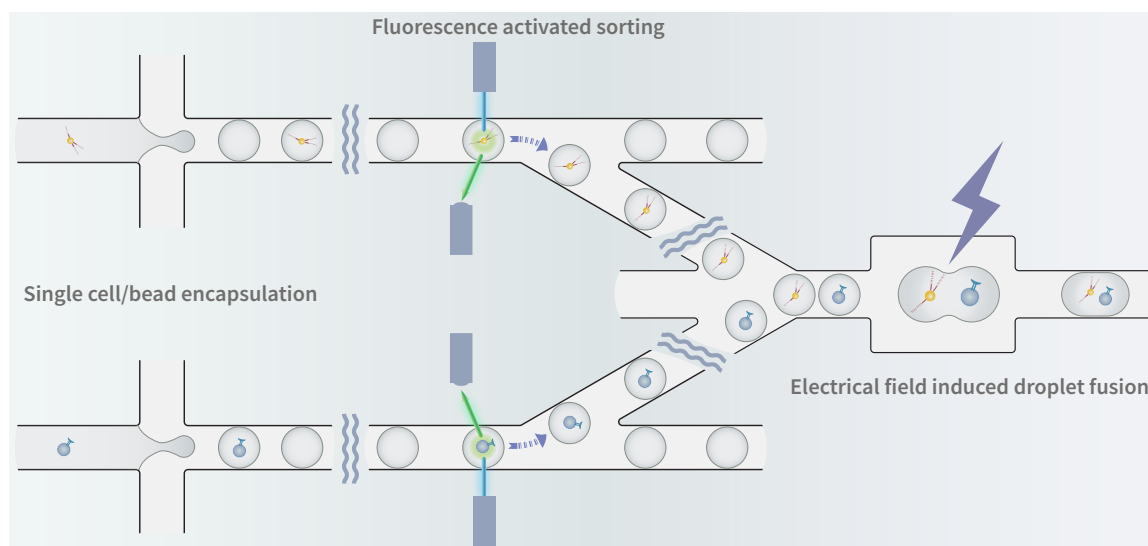


Figure 5:11 Schematic of pairing one cell and one bead in a droplet.

The second proposed improvement currently under development involves injection of an additional enzyme to droplets after PCR (Figure 5:12). This enzyme can efficiently join overlapping DNA fragments of PCR products (introduced by overlapping primers). Furthermore, this enzyme is heat sensitive (with an optimal working temperature of 50 °C) and thus cannot be loaded together with the reaction mixture at the start of the PCR reaction, and must be added after droplet PCR is complete. Preliminary tests indicate a significant increase in linkage efficiency (data not shown).

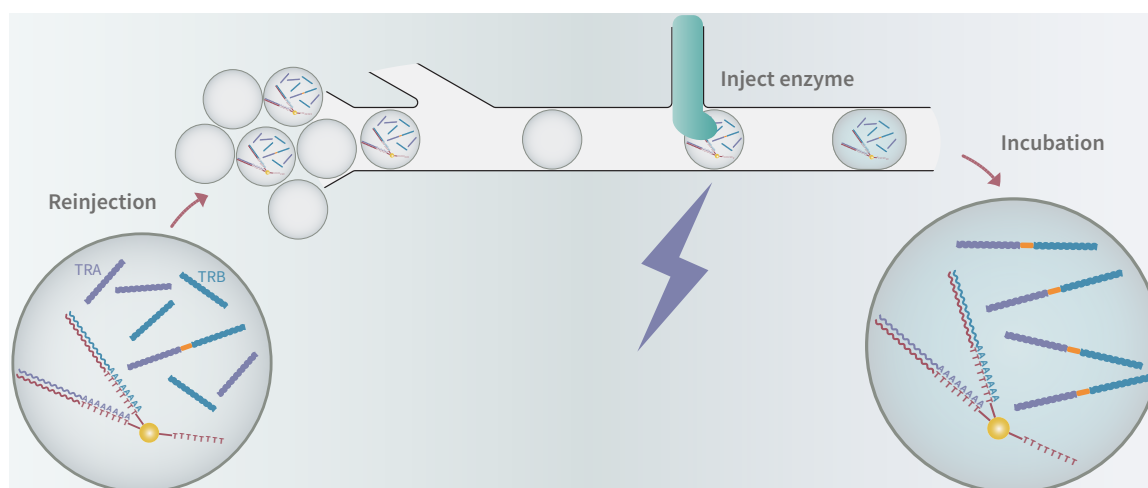


Figure 5:12 Schematic of injecting an enzyme into droplets to increase the efficiency of linkage PCR. The principle of this method can be referred to elsewhere[37, 55].

5.5 Conclusions

To date, we have constructed a droplet-based microfluidic platform able to rapidly and extract paired TCRs from tens of thousands of single T cells. Whilst technological refinements are still needed to increase the yield of linkage products, the results are exceptionally promising, with the method proving both robust and versatile. This microfluidic platform is tremendously valuable to study the TCR repertoire of tumour-infiltrating T cells which were revealed to be the ones able to recognise cancer antigens. As the immunological ACT therapies appear more and more convincing on a right track of overcoming human cancers⁵, we believe our efforts may greatly improve the identification of tumour-reactive TCRs, which a key for ACT therapies. Ultimately, our microfluidic platform will be adopted for identifying tumour antigens-specific TCRs for HCC patients. We expect that developments in this area will lead to a significant increase in the success rate of ACT therapies in near future.

⁵ In the process of ending this thesis, we were excited to hear on August 30, 2017, declared as “a historic action”, the first gene therapy (CAR T cell therapy, also the first ACT therapy) was approved by the U.S. Food and Drug Administration to treat B cell acute lymphoblastic leukemia[270].

Chapter 6 Conclusions and Outlook

Over the past decade, the development of droplet-based microfluidic technologies has occurred at a startling pace, with a clear focus on establishing functional components (for the processing and manipulation of droplet) and discovering applications where the features of such systems may be used to the best effect. Indeed, the studies described in this thesis were motivated by the need to create new tools for droplet manipulations and opportunities to use such systems in complex biological experiments. The first chapter summarized contemporary developments in building basic operational components and highlighted some of the most important features of droplet-based microfluidic systems. Developments described in Chapter 2 and 3 introduced two novel tools for generating user-defined droplets and manipulating droplets in a bespoke manner. Specifically, the V-junction is successful in matching the operational simplicity of regular T-junction formats, whilst enabling a wider range of functionalities that are normally only attainable when using robotic, droplet-on-demand systems. In addition, the manipulation of soft materials (cells and droplets) by magnetically actuated, helical microswimmers allowed the controlled assembly and disassembly of objects with complex configurations and represent a promising engineering tool for microfluidic droplet and cell-based experimentation. Chapter 4 then provided an analysis of how such systems can be used to good effect in genetic research at the scale of single molecule and single cell experiments. Finally, Chapter 5 described novel studies in which the integration of functional microfluidic components was used to define and develop a novel analytical platform for high-throughput profiling of antigen-specific T cell receptors at the single cell level. Such a base microfluidic platform is likely to be tremendously valuable in the study of the TCR repertoire of tumour-infiltrating T cells able to recognise cancer antigens. Such a platform has the potential to significantly improve the identification of tumour-reactive TCRs, which are key for ACT therapies.

More generally, the past decade has seen significant development in droplet-based microfluidic tools, with contemporary systems being able to address complex experimental workflows in a robust fashion. The next decade will undoubtedly see the continued commercialization of many platforms for defined biological applications, delivering microfluidics not

only to research laboratories, but also to hospitals, clinics and health NGOs. New functions and opportunities will continue to emerge, but research efforts will also continue to focus on improving and integrating existing modules to deliver reliable solutions. In this respect, we finish by making two predictions regarding developments that may occur over the short-medium term within the field.

6.1 Portable droplet-based microfluidics for point-of-care diagnostics

The demand for rapid, accurate, inexpensive and convenient point-of-care (PoC) systems for infectious disease diagnostics and wellness monitoring is significant. Ideal diagnostics should be both simple in their structure and portable, whilst ensuring that predefined questions can be answered in a quantitative, low-cost and rapid manner. Whilst droplet-based microfluidic systems offer a direct route to such quantitative diagnostics, their implementation for PoC nucleic acid analysis is far from simple. For example, fluid manipulation is a key concern, and should be cheap, robust and small. In this respect, syringe pump-free systems (which utilise manual droplet generation[16] or centrifugal microfluidics[222]) are particularly interesting. Moreover, isothermal amplification methods will be preferable to more traditional thermocycling techniques[209]. To this end, Schuler *et al.* recently demonstrated a system that utilises centrifugal step droplet generation, and is thus pump- and tubing-free (see Figure 4:4c)[222]. Using such an approach, the authors were able to perform isothermal ddPRA on-chip and quantify *L. monocytogene* DNA in food samples, reducing the time-to-result by four-fold when compared to the gold-standard tests. Moreover, Cao *et al.* showed a significant enhancement of fluid control in centrifugal microfluidics by introducing a novel two degrees of freedom (2-DoF) centrifugal microfluidic platform[271], which allows complex fluidic control in a direct manner, requiring no external components. These advances suggest new possibilities for the use of (droplet-based) centrifugal microfluidics in PoC applications.

6.2 Large scale integration to answer complex or unknown questions

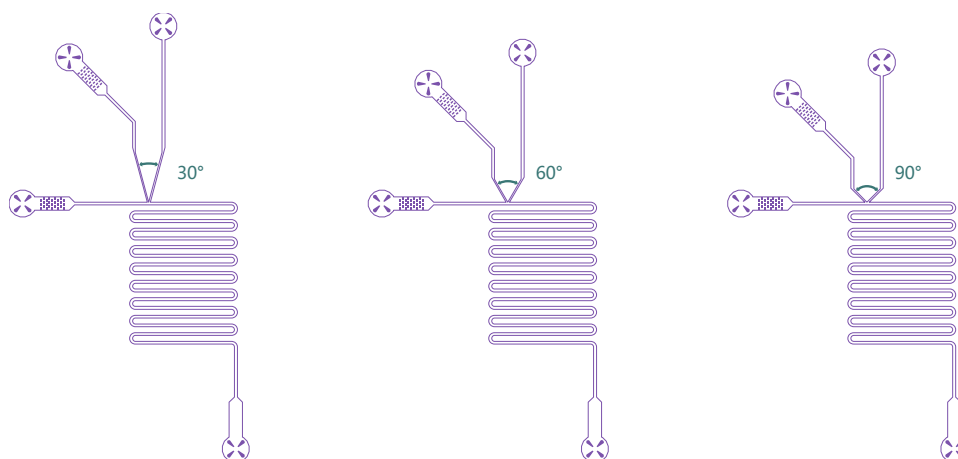
Whilst PoC devices provide maximum accessibility to the end-user, droplet-based microfluidic technologies have shown their true mettle in addressing comprehensive and complex biological questions. Although, and as we have seen, such systems have allowed experiments inaccessible on the macroscale to be performed in an automated and integrated

manner, we have only scratched the surface in terms of their ultimate potential. For example, droplet-based platforms have already been integrated with “machine learning” algorithms to allow the intelligent synthesis of a range of high quality nanomaterials for application in display and photovoltaic technologies[272, 273]. Such approaches leverage the ability of microfluidic systems to perform the chemistry/biology in an efficient manner and real-time detection to extract information on ms timescales. Machine learning methods will almost certainly impact biology in a similar way within the short term. As control architecture is refined, the sophisticated operations, shown for example in Figure 1:6, will no longer be the privilege of a few expert microfluidic laboratories, and droplet-based microfluidics will then become a basic tool used by any experimental scientist. Even though significant successes in system automation have been made (such as the *Fluidigm C1* platform), the automated and large-scale control of droplet networks integrating multiple functional components remains a daunting challenge, requiring the robust understanding and harnessing of non-linear and multi-phase fluid dynamics. In this respect, valuable progress has already been made in areas such as bubble logic[111], control logic[274] and electric circuit analogy[108]. Moreover, a recent study describing the “random design” of microfluidic systems is of particular interest[275]. In this approach, a library of thousands of random microfluidic chip designs was synthesized. The behaviour of each design was then simulated using finite element analysis, with users able to access structures suited to given tasks. We anticipate this type of interaction could form the basis of future microfluidic platform development. Indeed, through the collection and assimilation of user-generated data, machine-learning algorithms will allow the creation of entirely new microfluidic tools. Unsurprisingly, we feel that the future of droplet-based microfluidics is an exciting one.

Appendix A Supplementary information for Chapter 2

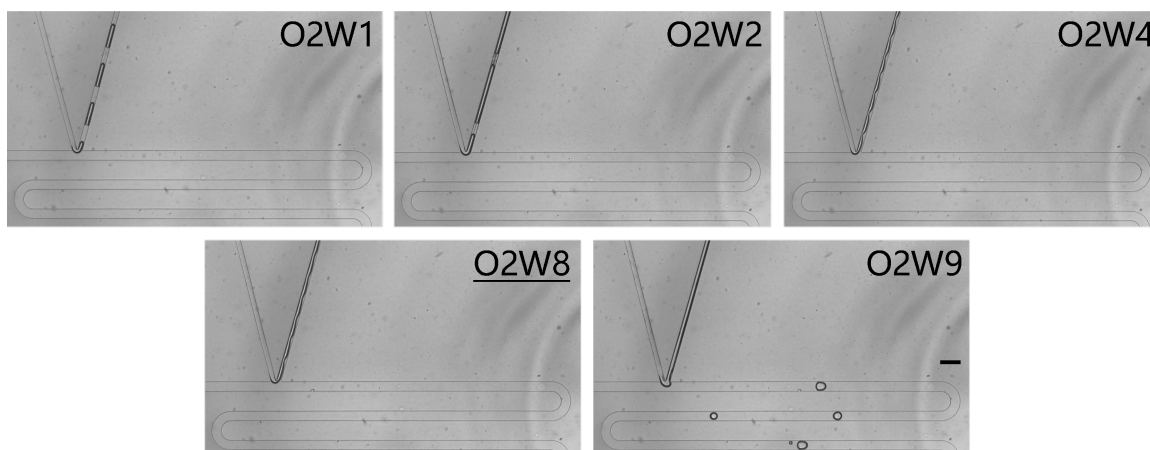
A.1 Operational upper flow rate limits in open-mode for varying V-junction angles

One of the fundamental characteristics of the V-junction is its ability to eliminate all the dispersed phase through the control channel when operating in open-mode. This feature is key to the success of important functions, such as the generation of target-sized droplets from the first one, clean switching of samples and the interruption and resumption of a running experiment. Three types of V-junction geometries possessing angles of 30°, 60° and 90° were fabricated (FigureS 1), and their operational upper limit (defined as the maximum water/oil flow rate ratio that still prevents the dispersed phase from entering the main channel) in open-mode tested.



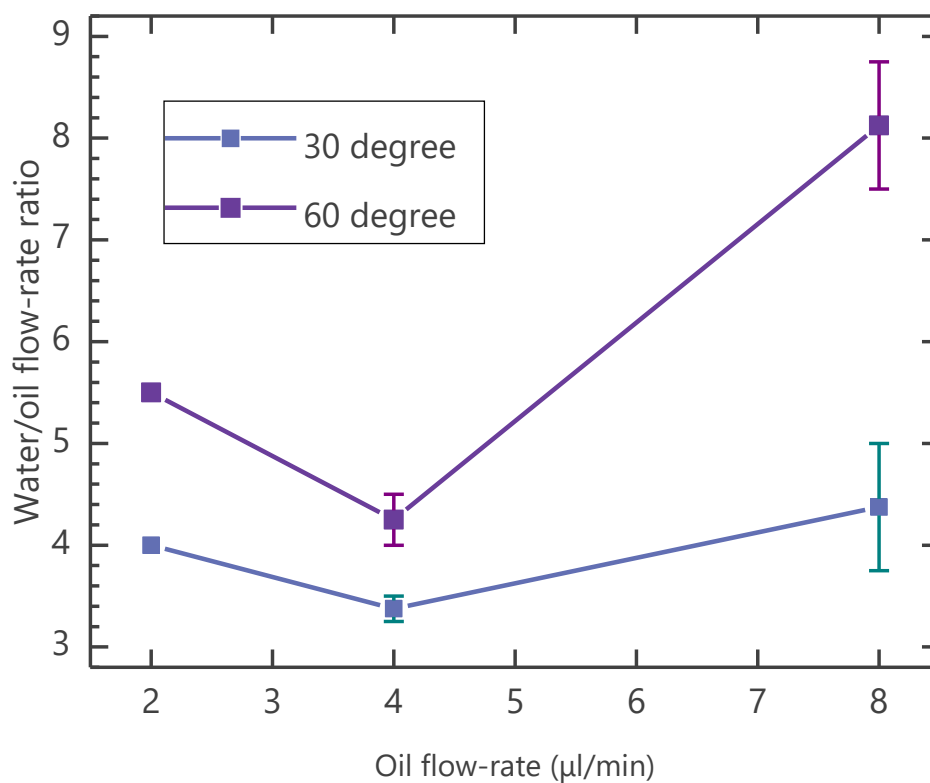
FigureS 1 Chip design of V-junction with three types of angles.

FigureS 2 illustrates a typical upper limit test for the 30° angle configuration. The oil flow rate was fixed at 2 $\mu\text{l}/\text{min}$ and the water flow rate was adjusted at 1, 2, 4, 8 and 9 $\mu\text{l}/\text{min}$ respectively. In this case droplets were injected in the main channel at a water flow rate of 9 $\mu\text{l}/\text{min}$. Therefore, the upper limit (water to oil flow rate ratio for an oil flow rate of 2 $\mu\text{l}/\text{min}$) in open-mode for this chip was determined to be 4.



FigureS 2 Determination of the upper bound of water/oil flow rate ratio in open-mode. O(2)W(1,2,4,8,9) defines the flow rates of each phase in $\mu\text{l}/\text{min}$. The scale bar is $200\ \mu\text{m}$.

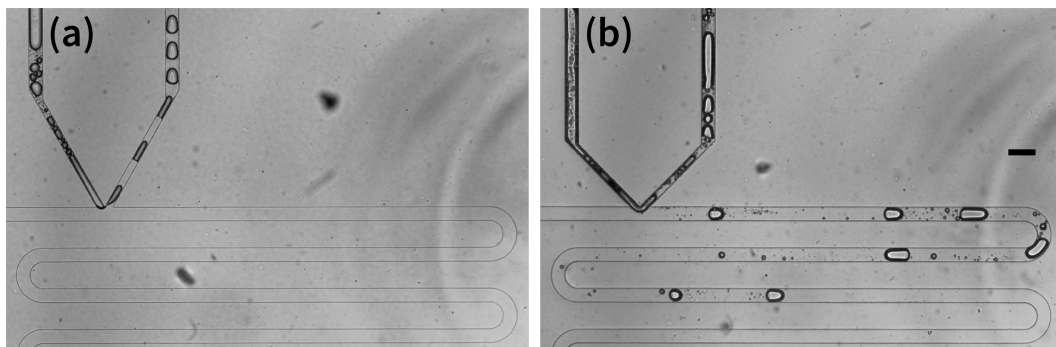
TableS 1 summarizes the operational upper limits for chip configurations of 30° and 60° , with a graphical representation provided in FigureS 3. The 90° chip was found to be inefficient in totally eliminating the water flux through the control channel, *i.e.* part of the aqueous phase always enters the main channel (see FigureS 4 and VideoS 1). Results indicate that the 60° chip design had the best operational characteristics.



FigureS 3 Graphical representation of data presented in TableS 1.

TableS 1 Summary of operational upper limit of water/oil flow rate ratios for 30° and 60° chips.

Chip type	Oil flow rate (μl/min)	Max water flow rate (μl/min)	Ratio
30°	2	8	4
	4	13–14	3.25–3.5
	8	30–40	3.75–5
60°	2	11	5.5
	4	16–18	4–4.5
	8	60–70	7.5–8.75



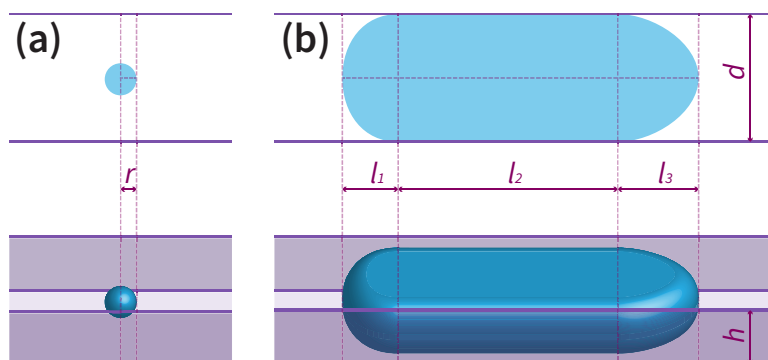
FigureS 4 Comparison of open-mode reliability for the 60° and 90° V-junction designs. The 90° chip (b) already fails at flow rates of 2 μl/min oil and 1 μl/min water (0.5 ratio) whilst 60° chip (a) is competent in the same condition. The scale bar is 200 μm.

A.2 Measurement of droplet volumes

The volume of droplets was estimated as follows:

$$V = \left\{ \begin{array}{ll} \frac{4}{3} \pi r^3 & \text{small droplet} \\ \{0.6(l_1 + l_3) + l_2\} dh & \text{large droplet} \end{array} \right\} \quad (\text{S:1})$$

For a small droplet (FigureS 5a) whose radius is smaller than half the height of the channel, the spherical volume can be directly calculated. For a large droplet (FigureS 5b) that contacts the sidewalls of the channel, the droplet is treated as an equivalent rectangular prism of width d (100 μm), height h (50 μm) and estimated equivalent length l ($0.6(l_1 + l_3) + l_2$).

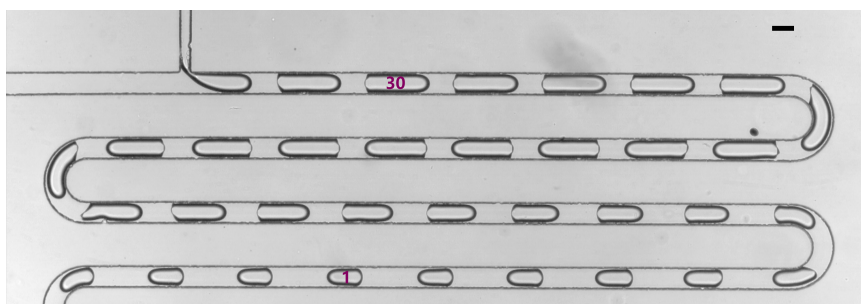


FigureS 5 Illustration of droplet volume calculation and feature sizes.

A.3 Comparison of the V-junction and T-junction

A.3.1 Size gradients

A periodic droplet train with an inherent size gradient was created in a T-junction under similar conditions to those used for the V-junction (a fixed oil flow rate of $2 \mu\text{l}/\text{min}$, but with a ramping flow rate profile directly applied to the water inlet). The results of such an experiment are displayed in FigureS 6, with extracted size information for both the T-junction and V-junction formats being displayed in TableS 2.



FigureS 6 Droplet size gradient using a T-junction. The smallest droplet is marked as (1) and the largest as (30). The scale bar is $100 \mu\text{m}$.

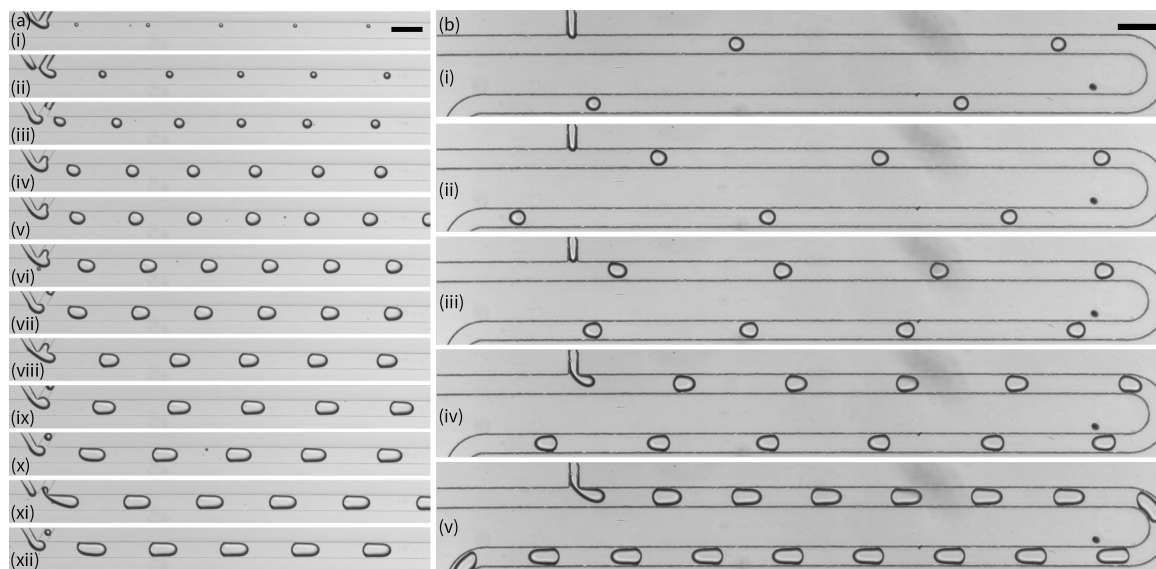
TableS 2 Volume of smallest and largest droplets for a V-junction (Figure 2:7 in Chapter 2) and a T-junction (FigureS 6).

Junction	Droplet ID	r (μm)	l_2 (μm)	$l_1 + l_3$ (μm)	V (pl)	Volume ratio
V	No.1 (largest)		141.1	66.1	903.8	110.2
	No.72 (smallest)	12.5			8.2	

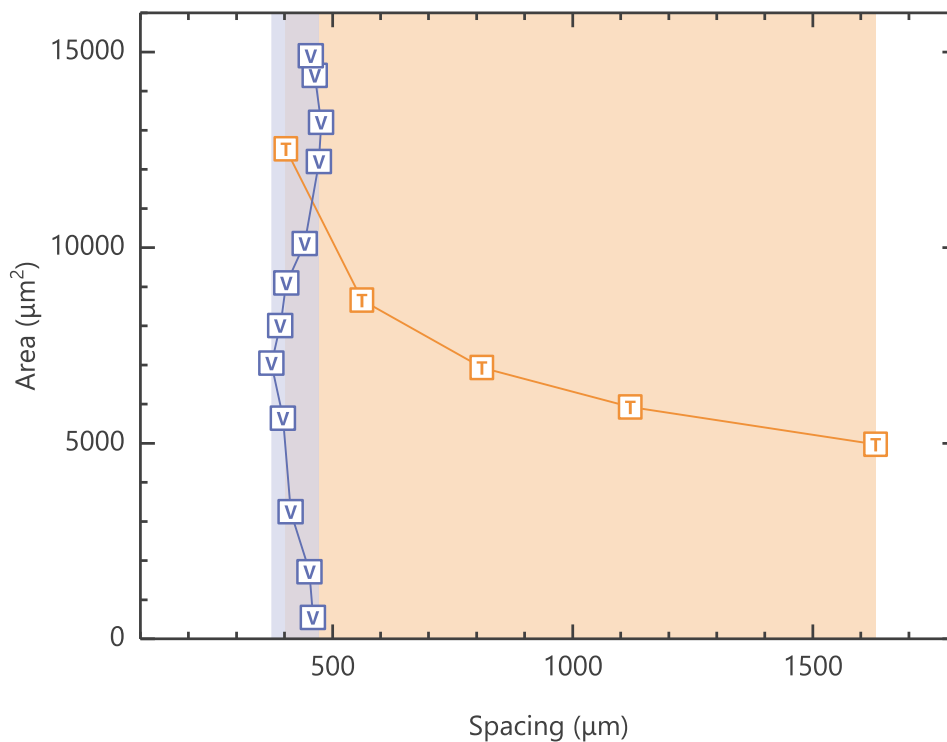
T	No.1 (smallest)	107.1	66.1	733.8	1.9
	No.30 (largest)	232.1	82.1	1406.8	

A.3.2 Relationship between size and frequency/spacing

Two series of experiments for creating several kinds of different sized droplets were performed in both V- and T-junctions (FigureS 7). In both cases the oil flow rate was fixed at $2 \mu\text{l}/\text{min}$. Droplet sizes were tuned by adjusting the water flow rate in the T-junction and adjusting the withdrawal flow rate in the V-junction (whilst keeping the water flow rate constant at $2 \mu\text{l}/\text{min}$). The smallest stable droplets obtained in the T-junction (FigureS 7a-i) occurred for water flow rates lower than $0.05 \mu\text{l}/\text{min}$. The results for droplet size (area) and generation frequency and spacing (defined here as the distance between centres of two neighbouring droplets) are summarized in TableS 3. These results indicate that both, the frequency and spacing are independent of size for droplets generated in the V-junction. This is not the case for those generated in the T-junction. The relationship between droplet size and spacing is shown graphically in FigureS 8.



FigureS 7 Comparison of frequency and spacing between droplets produced in (a) V-junction and (b) T-junction. The scale bars are $200 \mu\text{m}$.



FigureS 8 Plot of droplet spacing versus droplet area for V- and T- junctions.

TableS 3 Summary for measurements of size, frequency, and spacing for tests showing in FigureS 7.

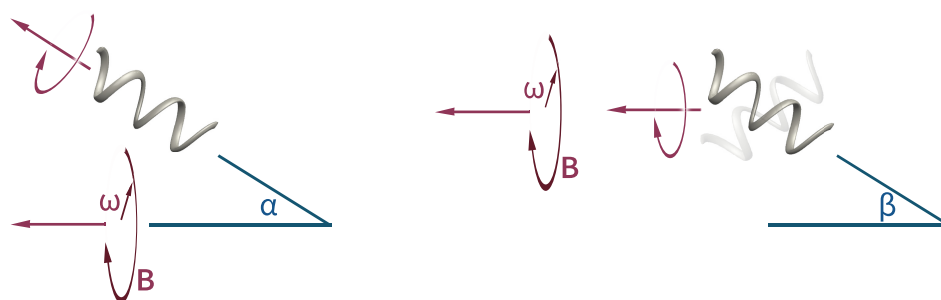
Chip	Related image	Area (μm^2)	Frequency (Hz)	Spacing (μm)
V	a-i	545	14.8	459
	a-ii	1711	16.0	452
	a-iii	3247	16.7	413
	a-iv	5640	16.7	397
	a-v	7045	17.4	373
	a-vi	8006	16.7	391
	a-vii	9092	15.4	404
	a-viii	10100	13.8	442
	a-ix	12200	12.5	472
	a-x	13200	12.5	476
	a-xi	14400	12.5	463
	a-xii	14900	13.3	455

T	b-i	4970	4.2	1631
	b-ii	5924	5.8	1120
	b-iii	6931	7.9	811
	b-iv	8655	11.9	561
	b-v	12522	18.5	403

Appendix B Supplementary information for Chapter 3

B.1 Assessment of swimming steadiness

To quantitatively evaluate steadiness, we assign relative values to two undesirable phenomena that arise during ABF operation; shifting (when the ABF trajectory deviates from the direction induced by the magnetic field) and wobbling (when the ABF wobbles but preserves its axial direction). If neither shifting nor wobbling are present, a score 0 is given for each respective parameter; conversely, a score of 3 is given for the maximum shifting or wobbling angles observed. A final score quantifying steadiness for any ABF is calculated using the relationship shown in FigureS 9.

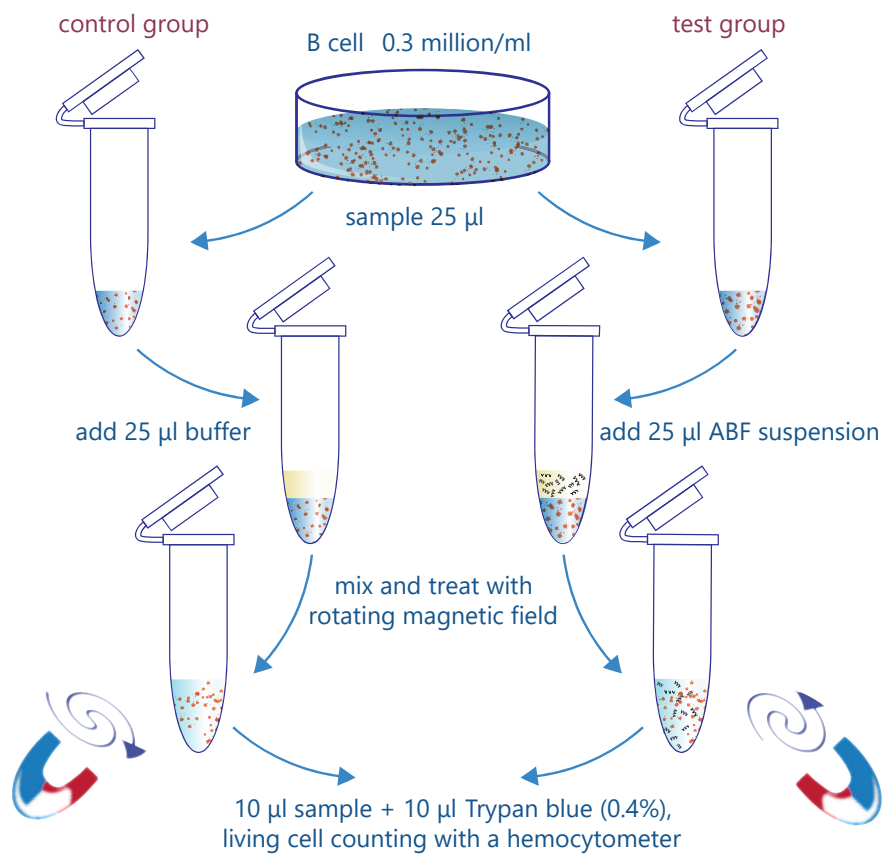


$$\text{Steadiness} = 3 \times (\alpha / \text{maximum shifting angle observed}) + 3 \times (\beta / \text{maximum wobbling angle observed})$$

FigureS 9 Calculation of the steadiness variable. The left image describes the shifting phenomenon and the right image the wobbling phenomenon.

B.2 Cell viability assessment

The cell viability assay follows the protocol described in FigureS 10, with only dead cells being stained. Results shown in TableS 4, indicating minimal variation in viability over a 2 hour timescale.



FigureS 10 Generic protocol for testing cell viability.

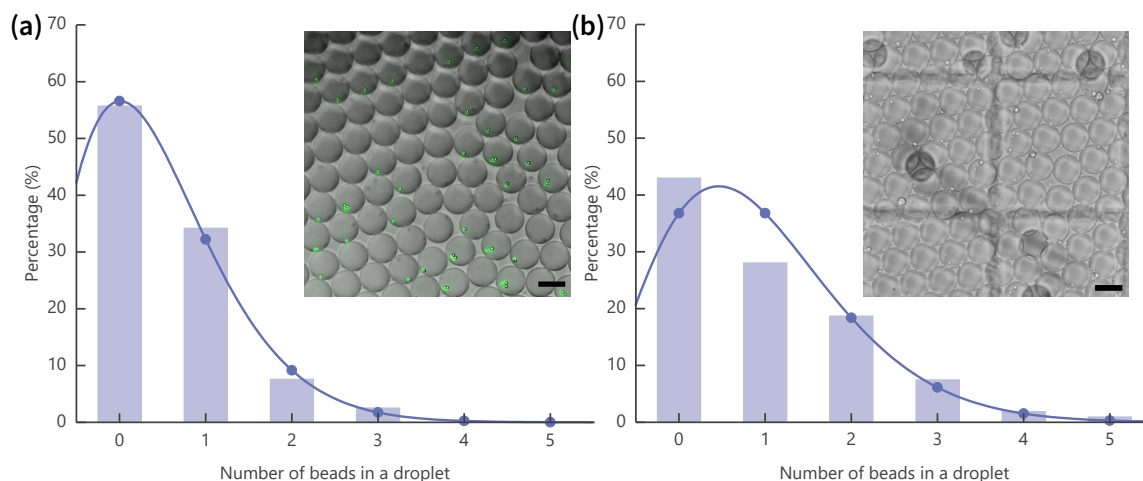
TableS 4 Cell viability assay results.

Time	Living cell proportion (control)	Living cell proportion (test)
15 min	97.3%	98.6%
30 min	96.2%	97.6%
60 min	96.1%	96.3%
120 min	94.0%	94.5%

Appendix C Supplementary information for Chapter 5

C.1 Directly increase average bead number

The average bead number per droplet can also be increased by using a higher concentration of beads. In the case shown in FigureS 11, 10 μm beads were tested with this approach. The conditions of flow rates for (a) and (b) were the same and thus resulted in droplets of the same sizes. The average number of beads is then directly determined by the inputted concentration of bead sample.



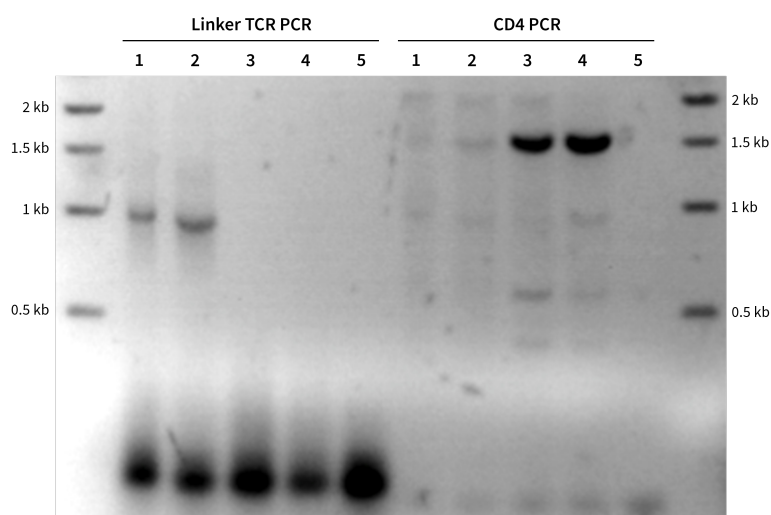
FigureS 11 Compare average number of beads per droplet by using different concentrations of bead suspensions. The beads used are fluorescent with the average diameter 10 μm . Case (a) has N equal to 0.57, whilst case (b) has N equal to 1. The image in (a) is a bright-field one with fluorescence overlay. The image in (b) is a normal bright-field one. The scale bars are 50 μm .

C.2 Verify mRNA capturing by PCR

The tests were set to four groups:

- #1 2,000,000 cells (200 μ l) + 2,000,000 beads (200 μ l) through microfluidic chip, mRNA capture in droplets, cDNA production in bulk
- #2 200,000 cells (200 μ l) + 2,000,000 beads (200 μ l) through microfluidic chip, mRNA capture in droplets, cDNA production in bulk
- #3 200,000 cells (200 μ l) + 200,000 beads (200 μ l) in bulk for mRNA capturing, cDNA production in bulk
- #4 200,000 cells (200 μ l) + 200,000 beads (200 μ l) in bulk, cDNA production in bulk, in the end, add 1,800,000 fresh beads (to mimic microfluidic condition)

Afterwards, beads were washed and added with PCR mix. Two types of PCR which target different amplification products were performed. One was for TCR. The other was for CD4. The bands are shown in FigureS 12.

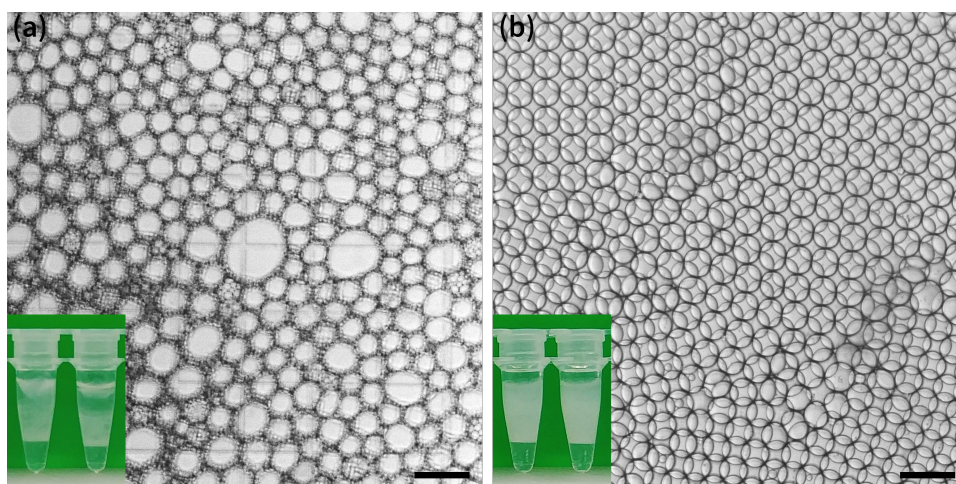


FigureS 12 PCR results for mRNA capturing. #5 is water control. Expected bands for linker TCR PCR is ~1 kb for single chains and 1.5 – 2 kb for linked products. Expected bands for CD4 PCR is ~1.4 kb.

C.3 Optimization of droplet stability for PCR

Two factors are the keys to droplets stability—monodispersity of droplet population and the dimension of droplet size. Put it simple, control these two factors is to settle droplets both in kinetically stable and thermodynamic stable[64]. The process of droplet PCR which is performed in elevated temperature increases the tendency of instability. We also find the specific buffer (containing detergents) used for linkage PCR has an additional impact on droplet stability. To successfully maintain the integrity for individual droplets, the requirements (monodispersity and size of droplets) are very demanding. In practice, based on our

tests, first, kick out any gas bubble in syringes and tubings before pumping liquid to the chip. Second, control the droplet sizes under $100\ \mu\text{m}$ in diameter; Thirdly, start to collect droplets only when the initial chaos of bubbles and is out. Finally, do not disturb the setup during the whole period of droplet generation. FigureS 13a shows the typical situation of stability-non-improved droplets after PCR. Some droplets shrink to tiny ones, whilst the others grow to giant ones, namely Ostwald Ripening. FigureS 14b shows, with the additional efforts made in droplet generation, droplets keep stable and monodispersity after PCR.

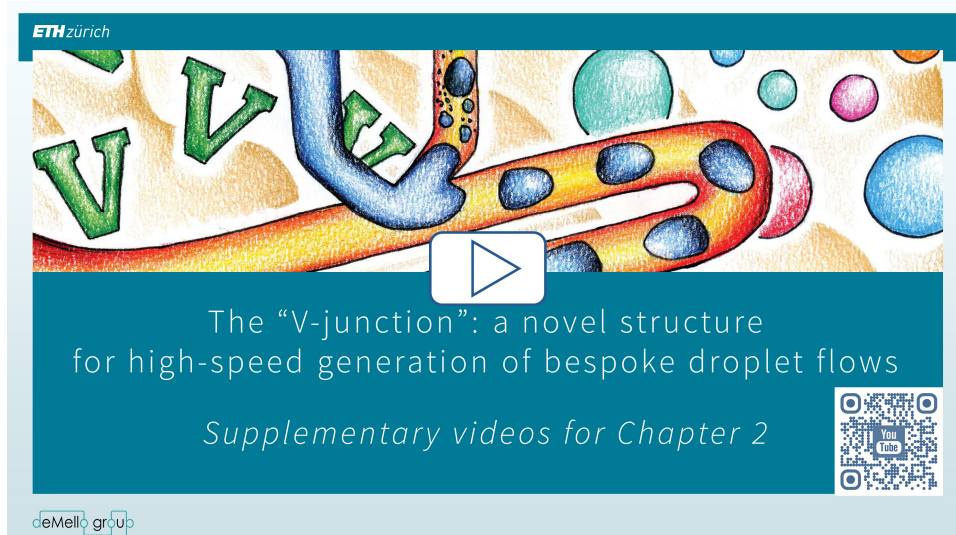


FigureS 13 (a) The look of droplets after PCR without stability improvement. (b) The look of droplets after PCR with stability improvement. The small images are photos of droplets in PCR tubes after the running of PCR. The big images are microscope images of samples taken from the corresponding tubes. The scale bars are $100\ \mu\text{m}$.

Appendix D Supplementary information of videos

Two supplementary collections of video clips are provided here for the project “V-junction” and “ABF” respectively. Readers with PDF electronic version can find them in attachments, or click the hyperlink in the screenshots below and watch them online. Readers with printed version can scan the QR code in the screenshots and watch them on mobile devices.

D.1 Supplementary videos for Chapter 2



This video collection includes 7 clips:

VideoS 1 Different performance for 60° and 90° chips at open-mode.

VideoS 2 Tracking and visualization of oil flow for open-mode and closed-mode.

VideoS 3 Steps to create stable and controlled-size water droplets from the first one.

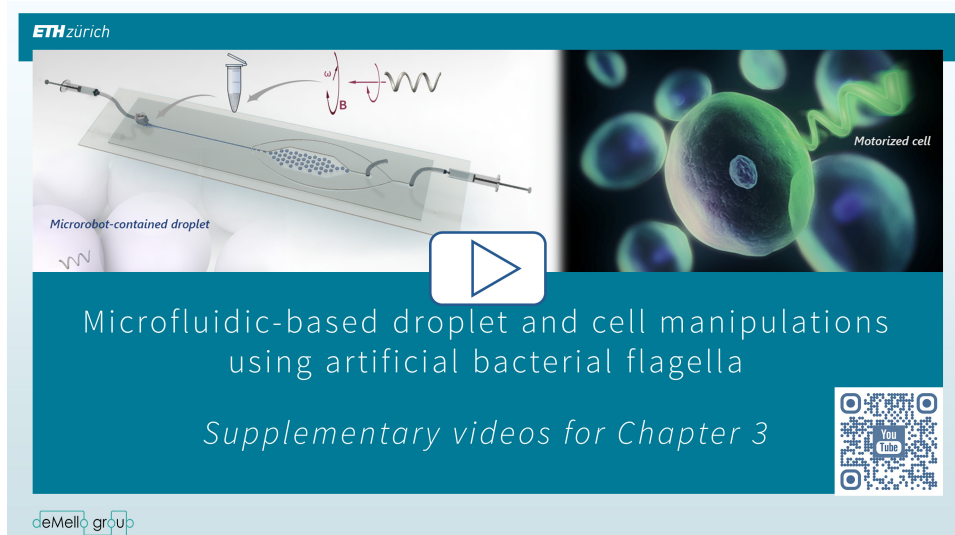
VideoS 4 A droplet size gradient generated by increasing the suction rate at the control channel.

VideoS 5 Study droplet behaviour in a microfluidic network.

VideoS 6 Formation of small droplets by applying a slight negative pressure at the control channel.

VideoS 7 Simple generation of residence time gradients.

D.2 Supplementary videos for Chapter 3



This video collection includes 9 clips:

VideoS 8 Manipulation of microswimmers within a droplet.

VideoS 9 Targeted delivery of a droplet in an uncapped tank.

VideoS 10 A droplet that wets the surface and cannot be moved.

VideoS 11 Transportation of a droplet within a PDMS chamber.

VideoS 12 Adhesion between a droplet and a microswimmer.

VideoS 13 Simultaneous movement of two droplets.

VideoS 14 Assembling and disassembling a motorized cell.

VideoS 15 A microswimmer dragging a cell.

VideoS 16 Formation of a microswimmer-cell-microswimmer assembly.

References

- [1] Griffiths AD, Tawfik DS. Miniaturising the laboratory in emulsion droplets. *Trends Biotechnol* 2006; 24: 395–402.
- [2] Huebner A, Srisa-Art M, Holt D, et al. Quantitative detection of protein expression in single cells using droplet microfluidics. *Chem Commun* 2007; 1218–1220.
- [3] Pekin D, Skhiri Y, Baret J-C, et al. Quantitative and sensitive detection of rare mutations using droplet-based microfluidics. *Lab Chip* 2011; 11: 2156–2166.
- [4] Juul S, Nielsen CJF, Labouriau R, et al. Droplet Microfluidics Platform for Highly Sensitive and Quantitative Detection of Malaria-Causing Plasmodium Parasites Based on Enzyme Activity Measurement. *ACS Nano* 2012; 6: 10676–10683.
- [5] Ugelstad J, El-Aasser MS, Vanderhoff JW. Emulsion polymerization: Initiation of polymerization in monomer droplets. *J Polym Sci Polym Lett Ed* 1973; 11: 503–513.
- [6] Linn EE, West MP. *Water-in-oil microemulsions for cosmetic uses*. US4797272 [Ahttp://www.google.com/patents/US4797272](http://www.google.com/patents/US4797272) (1989, accessed 3 October 2016).
- [7] Garti N. Progress in Stabilization and Transport Phenomena of Double Emulsions in Food Applications. *LWT - Food Sci Technol* 1997; 30: 222–235.
- [8] Shim J, Ranasinghe RT, Smith CA, et al. Ultrarapid Generation of Femtoliter Microfluidic Droplets for Single-Molecule-Counting Immunoassays. *ACS Nano* 2013; 7: 5955–5964.
- [9] Thorsen T, Roberts RW, Arnold FH, et al. Dynamic Pattern Formation in a Vesicle-Generating Microfluidic Device. *Phys Rev Lett* 2001; 86: 4163–4166.
- [10] Anna SL, Bontoux N, Stone HA. Formation of dispersions using 'flow focusing' in microchannels. *Appl Phys Lett* 2003; 82: 364–366.
- [11] Umbanhowar PB, Prasad V, Weitz DA. Monodisperse Emulsion Generation via Drop Break Off in a Coflowing Stream. *Langmuir* 2000; 16: 347–351.
- [12] Cramer C, Fischer P, Windhab EJ. Drop formation in a co-flowing ambient fluid. *Chem Eng Sci* 2004; 59: 3045–3058.

- [13] Sugiura S, Nakajima M, Iwamoto S, et al. Interfacial Tension Driven Monodispersed Droplet Formation from Microfabricated Channel Array. *Langmuir* 2001; 17: 5562–5566.
- [14] Kobayashi I, Mukataka S, Nakajima M. Novel Asymmetric Through-Hole Array Microfabricated on a Silicon Plate for Formulating Monodisperse Emulsions. *Langmuir* 2005; 21: 7629–7632.
- [15] Ding Y, Solvas XC i, deMello A. 'V-junction': a novel structure for high-speed generation of bespoke droplet flows. *Analyst* 2014; 140: 414–421.
- [16] Dangla R, Kayi SC, Baroud CN. Droplet microfluidics driven by gradients of confinement. *Proc Natl Acad Sci* 2013; 110: 853–858.
- [17] Ding Y, Stavrakis S, Casadevall i Solvas X, et al. A High Throughput Droplet-Based Microfluidic Barcode Generator. In: *Micro Total Analysis Systems 2013*. 2013.
- [18] Song H, Bringer MR, Tice JD, et al. Experimental test of scaling of mixing by chaotic advection in droplets moving through microfluidic channels. *Appl Phys Lett* 2003; 83: 4664–4666.
- [19] Guo F, Lapsley MI, Nawaz AA, et al. A Droplet-Based, Optofluidic Device for High-Throughput, Quantitative Bioanalysis. *Anal Chem* 2012; 84: 10745–10749.
- [20] Ji X-H, Cheng W, Guo F, et al. On-demand preparation of quantum dot-encoded microparticles using a droplet microfluidic system. *Lab Chip* 2011; 11: 2561–2568.
- [21] Gerver RE, Gómez-Sjöberg R, Baxter BC, et al. Programmable microfluidic synthesis of spectrally encoded microspheres. *Lab Chip* 2012; 12: 4716–4723.
- [22] Hess D, Rane A, deMello AJ, et al. High-Throughput, Quantitative Enzyme Kinetic Analysis in Microdroplets Using Stroboscopic Epifluorescence Imaging. *Anal Chem* 2015; 87: 4965–4972.
- [23] Unger MA, Chou H-P, Thorsen T, et al. Monolithic Microfabricated Valves and Pumps by Multilayer Soft Lithography. *Science* 2000; 288: 113–116.
- [24] Willaime H, Barbier V, Kloul L, et al. Arnold Tongues in a Microfluidic Drop Emitter. *Phys Rev Lett* 2006; 96: 054501.
- [25] Zeng S, Li B, Su X, et al. Microvalve-actuated precise control of individual droplets in microfluidic devices. *Lab Chip* 2009; 9: 1340–1343.
- [26] Link DR, Grasland-Mongrain E, Duri A, et al. Electric Control of Droplets in Microfluidic Devices. *Angew Chem Int Ed* 2006; 45: 2556–2560.

- [27] Collins DJ, Alan T, Helmerson K, et al. Surface acoustic waves for on-demand production of picoliter droplets and particle encapsulation. *Lab Chip* 2013; 13: 3225–3231.
- [28] Lorenz RM, Edgar JS, Jeffries GDM, et al. Microfluidic and Optical Systems for the On-Demand Generation and Manipulation of Single Femtoliter-Volume Aqueous Droplets. *Anal Chem* 2006; 78: 6433–6439.
- [29] Baroud CN, Delville J-P, Gallaire F, et al. Thermocapillary valve for droplet production and sorting. *Phys Rev E* 2007; 75: 046302.
- [30] Rane TD, Zec HC, Wang T-H. A Barcode-Free Combinatorial Screening Platform for Matrix Metalloproteinase Screening. *Anal Chem* 2015; 87: 1950–1956.
- [31] Niu X, Gulati S, Edel JB, et al. Pillar-induced droplet merging in microfluidic circuits. *Lab Chip* 2008; 8: 1837.
- [32] Deng N-N, Sun S-X, Wang W, et al. A novel surgery-like strategy for droplet coalescence in microchannels. *Lab Chip*. Epub ahead of print 22 July 2013. DOI: 10.1039/C3LC50533B.
- [33] Mazutis L, Griffiths AD. Selective droplet coalescence using microfluidic systems. *Lab Chip* 2012; 12: 1800–1806.
- [34] Akartuna I, Aubrecht DM, Kodger TE, et al. Chemically induced coalescence in droplet-based microfluidics. *Lab Chip* 2015; 15: 1140–1144.
- [35] Niu X, Gielen F, Edel JB, et al. A microdroplet dilutor for high-throughput screening. *Nat Chem* 2011; 3: 437–442.
- [36] Sun M, Vanapalli SA. Generation of Chemical Concentration Gradients in Mobile Droplet Arrays via Fragmentation of Long Immiscible Diluting Plugs. *Anal Chem* 2013; 85: 2044–2048.
- [37] Abate AR, Hung T, Mary P, et al. High-throughput injection with microfluidics using picoinjectors. *Proc Natl Acad Sci* 2010; 107: 19163–19166.
- [38] Chen D, Du W, Liu Y, et al. The chemistode: A droplet-based microfluidic device for stimulation and recording with high temporal, spatial, and chemical resolution. *Proc Natl Acad Sci* 2008; 105: 16843–16848.
- [39] Doonan SR, Bailey RC. K-Channel: A Multifunctional Architecture for Dynamically Reconfigurable Sample Processing in Droplet Microfluidics. *Anal Chem* 2017; 89: 4091–4099.

- [40] Link DR, Anna SL, Weitz DA, et al. Geometrically Mediated Breakup of Drops in Microfluidic Devices. *Phys Rev Lett* 2004; 92: 054503.
- [41] Gao R, Cheng Z, deMello AJ, et al. Wash-free magnetic immunoassay of the PSA cancer marker using SERS and droplet microfluidics. *Lab Chip* 2016; 16: 1022–1029.
- [42] Ahn B, Lee K, Lee H, et al. Parallel synchronization of two trains of droplets using a railroad-like channel network. *Lab Chip* 2011; 11: 3956–3962.
- [43] Bai Y, He X, Liu D, et al. A double droplet trap system for studying mass transport across a droplet-droplet interface. *Lab Chip* 2010; 10: 1281–1285.
- [44] Lee D-H, Lee W, Um E, et al. Microbridge structures for uniform interval control of flowing droplets in microfluidic networks. *Biomicrofluidics* 2011; 5: 034117.
- [45] Baret J-C, Miller OJ, Taly V, et al. Fluorescence-activated droplet sorting (FADS): efficient microfluidic cell sorting based on enzymatic activity. *Lab Chip* 2009; 9: 1850–1858.
- [46] Nam J, Lim H, Kim C, et al. Density-dependent separation of encapsulated cells in a microfluidic channel by using a standing surface acoustic wave. *Biomicrofluidics* 2012; 6: 024120.
- [47] Cao Z, Chen F, Bao N, et al. Droplet sorting based on the number of encapsulated particles using a solenoid valve. *Lab Chip*. Epub ahead of print 2013. DOI: 10.1039/c2lc40950j.
- [48] Korczyk PM, Derzsi L, Jakiela S, et al. Microfluidic traps for hard-wired operations on droplets. *Lab Chip*. Epub ahead of print 31 July 2013. DOI: 10.1039/C3LC50347J.
- [49] Wang W, Yang C, Liu Y, et al. On-demand droplet release for droplet-based microfluidic system. *Lab Chip* 2010; 10: 559–562.
- [50] Courtney M, Chen X, Chan S, et al. Droplet Microfluidic System with On-Demand Trapping and Releasing of Droplet for Drug Screening Applications. *Anal Chem* 2017; 89: 910–915.
- [51] Huebner A, Bratton D, Whyte G, et al. Static microdroplet arrays: a microfluidic device for droplet trapping, incubation and release for enzymatic and cell-based assays. *Lab Chip* 2009; 9: 692–698.
- [52] Wen H, Yu Y, Zhu G, et al. A droplet microchip with substance exchange capability for the developmental study of *C. elegans*. *Lab Chip* 2015; 15: 1905–1911.
- [53] Hatch AC, Fisher JS, Tovar AR, et al. 1-Million droplet array with wide-field fluorescence imaging for digital PCR. *Lab Chip* 2011; 11: 3838–3845.

- [54] Hatch AC, Fisher JS, Pentoney SL, et al. Tunable 3D droplet self-assembly for ultra-high-density digital micro-reactor arrays. *Lab Chip* 2011; 11: 2509–2517.
- [55] Eastburn DJ, Sciambi A, Abate AR. Picoinjection Enables Digital Detection of RNA with Droplet RT-PCR. *PLOS ONE* 2013; 8: e62961.
- [56] Brouzes E, Medkova M, Savenelli N, et al. Droplet microfluidic technology for single-cell high-throughput screening. *Proc Natl Acad Sci* 2009; 106: 14195–14200.
- [57] Pan X, Zeng S, Zhang Q, et al. Sequential microfluidic droplet processing for rapid DNA extraction. *ELECTROPHORESIS* 2011; 32: 3399–3405.
- [58] Cho S, Kang D-K, Sim S, et al. Droplet-Based Microfluidic Platform for High-Throughput, Multi-Parameter Screening of Photosensitizer Activity. *Anal Chem* 2013; 85: 8866–8872.
- [59] Lan F, Haliburton JR, Yuan A, et al. Droplet barcoding for massively parallel single-molecule deep sequencing. *Nat Commun* 2016; 7: 11784.
- [60] Baret J-C. Surfactants in droplet-based microfluidics. *Lab Chip* 2012; 12: 422–433.
- [61] Williams R, Peisajovich SG, Miller OJ, et al. Amplification of complex gene libraries by emulsion PCR. *Nat Methods* 2006; 3: 545–550.
- [62] Schütze T, Rubelt F, Repkow J, et al. A streamlined protocol for emulsion polymerase chain reaction and subsequent purification. *Anal Biochem* 2011; 410: 155–157.
- [63] Bian X, Jing F, Li G, et al. A microfluidic droplet digital PCR for simultaneous detection of pathogenic *Escherichia coli* O157 and *Listeria monocytogenes*. *Biosens Bioelectron* 2015; 74: 770–777.
- [64] Kabalnov A. Ostwald Ripening and Related Phenomena. *J Dispers Sci Technol* 2001; 22: 1–12.
- [65] Holtze C, Rowat AC, Agresti JJ, et al. Biocompatible surfactants for water-in-fluorocarbon emulsions. *Lab Chip* 2008; 8: 1632–1639.
- [66] Webster AJ, Cates ME. Stabilization of Emulsions by Trapped Species. *Langmuir* 1998; 14: 2068–2079.
- [67] Calderó G, García-Celma MJ, Solans C, et al. Diffusion from Hydrogenated and Fluorinated Gel–Emulsion Mixtures. *Langmuir* 1998; 14: 1580–1585.
- [68] Skhiri Y, Gruner P, Semin B, et al. Dynamics of molecular transport by surfactants in emulsions. *Soft Matter* 2012; 8: 10618–10627.

- [69] Chen Y, Gani AW, Tang SKY. Characterization of sensitivity and specificity in leaky droplet-based assays. *Lab Chip* 2012; 12: 5093–5103.
- [70] Gruner P, Riechers B, Chacòn Orellana LA, et al. Stabilisers for water-in-fluorinated-oil dispersions: Key properties for microfluidic applications. *Curr Opin Colloid Interface Sci* 2015; 20: 183–191.
- [71] Debon AP, Wootton RCR, Elvira KS. Droplet confinement and leakage: Causes, underlying effects, and amelioration strategies. *Biomicrofluidics* 2015; 9: 024119.
- [72] Gruner P, Riechers B, Semin B, et al. Controlling molecular transport in minimal emulsions. *Nat Commun* 2016; 7: 10392.
- [73] Courtois F, Olguin LF, Whyte G, et al. Controlling the Retention of Small Molecules in Emulsion Microdroplets for Use in Cell-Based Assays. *Anal Chem* 2009; 81: 3008–3016.
- [74] Zhang C, Xing D. Miniaturized PCR chips for nucleic acid amplification and analysis: latest advances and future trends. *Nucleic Acids Res* 2007; 35: 4223–4237.
- [75] Bashir S, Solvas XC i, Bashir M, et al. Dynamic wetting in microfluidic droplet formation. *BioChip J* 2014; 8: 122–128.
- [76] Köster S, Angilè FE, Duan H, et al. Drop-based microfluidic devices for encapsulation of single cells. *Lab Chip* 2008; 8: 1110–1115.
- [77] Gough KM. Theoretical analysis of molecular polarizabilities and polarizability derivatives in hydrocarbons. *J Chem Phys* 1989; 91: 2424–2432.
- [78] O'Hagan D. Understanding organofluorine chemistry. An introduction to the C–F bond. *Chem Soc Rev* 2008; 37: 308–319.
- [79] Lemal DM. Perspective on Fluorocarbon Chemistry. *J Org Chem* 2004; 69: 1–11.
- [80] Baroud CN, Gallaire F, Dangla R. Dynamics of microfluidic droplets. *Lab Chip* 2010; 10: 2032.
- [81] Haight FA. *Handbook of the Poisson distribution*. New York, NY: Wiley <http://cds.cern.ch/record/100759> (1967).
- [82] Absolute Quantification of PCR Targets | Applications & Technologies | Bio-Rad <http://www.bio-rad.com/en-us/applications-technologies/absolute-quantification-pcr-targets-with-droplet-digital-pcr-system> (accessed 22 June 2017).

- [83] Ramsey JD, Jacobson SC, Culbertson CT, et al. High-Efficiency, Two-Dimensional Separations of Protein Digests on Microfluidic Devices. *Anal Chem* 2003; 75: 3758–3764.
- [84] Guo MT, Rotem A, Heyman JA, et al. Droplet microfluidics for high-throughput biological assays. *Lab Chip* 2012; 12: 2146–2155.
- [85] Marcus JS, Anderson WF, Quake SR. Microfluidic Single-Cell mRNA Isolation and Analysis. *Anal Chem* 2006; 78: 3084–3089.
- [86] Song H, Tice JD, Ismagilov RF. A Microfluidic System for Controlling Reaction Networks in Time. *Angew Chem Int Ed* 2003; 42: 768–772.
- [87] Erickson D, Sinton D, Li D. Joule heating and heat transfer in poly(dimethylsiloxane) microfluidic systems. *Lab Chip* 2003; 3: 141–149.
- [88] Squires TM, Quake SR. Microfluidics: Fluid physics at the nanoliter scale. *Rev Mod Phys* 2005; 77: 977–1026.
- [89] Easley CJ, Karlinsey JM, Bienvenue JM, et al. A fully integrated microfluidic genetic analysis system with sample-in-answer-out capability. *Proc Natl Acad Sci* 2006; 103: 19272–19277.
- [90] Teh S-Y, Lin R, Hung L-H, et al. Droplet microfluidics. *Lab Chip* 2008; 8: 198–220.
- [91] Joensson HN, Andersson Svahn H. Droplet Microfluidics—A Tool for Single-Cell Analysis. *Angew Chem Int Ed* 2012; 51: 12176–12192.
- [92] Tice JD, Song H, Lyon AD, et al. Formation of Droplets and Mixing in Multiphase Microfluidics at Low Values of the Reynolds and the Capillary Numbers. *Langmuir* 2003; 19: 9127–9133.
- [93] Frenz L, Blank K, Brouzes E, et al. Reliable microfluidic on-chip incubation of droplets in delay-lines. *Lab Chip* 2009; 9: 1344–1348.
- [94] Cartas-Ayala MA, Raafat M, Karnik R. Self-Sorting of Deformable Particles in an Asynchronous Logic Microfluidic Circuit. *Small* 2013; 9: 375–381.
- [95] Wang Y, Tumarkin E, Velasco D, et al. Exploring a direct injection method for microfluidic generation of polymer microgels. *Lab Chip* 2013; 13: 2547–2553.
- [96] Schaerli Y, Wootton RC, Robinson T, et al. Continuous-Flow Polymerase Chain Reaction of Single-Copy DNA in Microfluidic Microdroplets. *Anal Chem* 2009; 81: 302–306.

- [97] Solvas XC i, Turek V, Prodromakis T, et al. Microfluidic evaporator for on-chip sample concentration. *Lab Chip* 2012; 12: 4049–4054.
- [98] Seemann R, Brinkmann M, Pfohl T, et al. Droplet based microfluidics. *Rep Prog Phys* 2012; 75: 016601.
- [99] Christopher GF, Anna SL. Microfluidic methods for generating continuous droplet streams. *J Phys Appl Phys* 2007; 40: R319.
- [100] Zeng Y, Shin M, Wang T. Programmable active droplet generation enabled by integrated pneumatic micropumps. *Lab Chip* 2012; 13: 267–273.
- [101] Zec H, Rane TD, Wang T-H. Microfluidic platform for on-demand generation of spatially indexed combinatorial droplets. *Lab Chip* 2012; 12: 3055–3062.
- [102] Gielen F, van Vliet L, Koprowski BT, et al. A Fully Unsupervised Compartment-on-Demand Platform for Precise Nanoliter Assays of Time-Dependent Steady-State Enzyme Kinetics and Inhibition. *Anal Chem* 2013; 85: 4761–4769.
- [103] Lin R, Fisher JS, Simon MG, et al. Novel on-demand droplet generation for selective fluid sample extraction. *Biomicrofluidics* 2012; 6: 024103-024103-10.
- [104] Xia Y, Whitesides GM. Soft Lithography. *Angew Chem Int Ed* 1998; 37: 550–575.
- [105] Eddington DT, Puccinelli JP, Beebe DJ. Thermal aging and reduced hydrophobic recovery of polydimethylsiloxane. *Sens Actuators B Chem* 2006; 114: 170–172.
- [106] Basu AS. Droplet morphometry and velocimetry (DMV): a video processing software for time-resolved, label-free tracking of droplet parameters. *Lab Chip* 2013; 13: 1892–1901.
- [107] PIV (Particle Image Velocimetry) --- ImageJ plugin - ImageJ plugins by Qingzong TSENG. <https://sites.google.com/site/qingzongtseng/piv><https://sites.google.com/site/qingzongtseng/piv> (accessed 16 October 2013).
- [108] Oh KW, Lee K, Ahn B, et al. Design of pressure-driven microfluidic networks using electric circuit analogy. *Lab Chip* 2012; 12: 515–545.
- [109] Bremond N, Thiam AR, Bibette J. Decompressing Emulsion Droplets Favors Coalescence. *Phys Rev Lett* 2008; 100: 024501.
- [110] Bithi SS, Vanapalli SA. Behavior of a train of droplets in a fluidic network with hydrodynamic traps. *Biomicrofluidics* 2010; 4: 044110-044110-10.

- [111] Prakash M, Gershenfeld N. Microfluidic Bubble Logic. *Science* 2007; 315: 832–835.
- [112] Xu S, Nie Z, Seo M, et al. Generation of monodisperse particles by using microfluidics: control over size, shape, and composition. *Angew Chem* 2004; 117: 734–738.
- [113] Arayanarakool R, Shui L, Kengen SWM, et al. Single-enzyme analysis in a droplet-based micro- and nanofluidic system. *Lab Chip* 2013; 13: 1955–1962.
- [114] Verbruggen B, Tóth T, Atalay YT, et al. Design of a flow-controlled asymmetric droplet splitter using computational fluid dynamics. *Microfluid Nanofluidics* 2013; 15: 243–252.
- [115] Garstecki P, Fuerstman MJ, Stone HA, et al. Formation of droplets and bubbles in a microfluidic T-junction—scaling and mechanism of break-up. *Lab Chip* 2006; 6: 437.
- [116] Schindler M, Ajdari A. Droplet Traffic in Microfluidic Networks: A Simple Model for Understanding and Designing. *Phys Rev Lett* 2008; 100: 044501.
- [117] Yang Y-J, Feng X, Xu N, et al. Generation of sub-femtoliter droplet by T-junction splitting on microfluidic chips. *Appl Phys Lett* 2013; 102: 123502-123502–5.
- [118] Song H, Chen DL, Ismagilov RF. Reactions in Droplets in Microfluidic Channels. *Angew Chem Int Ed* 2006; 45: 7336–7356.
- [119] Pompano RR, Liu W, Du W, et al. Microfluidics Using Spatially Defined Arrays of Droplets in One, Two, and Three Dimensions. *Annu Rev Anal Chem* 2011; 4: 59–81.
- [120] Lee M, Collins JW, Aubrecht DM, et al. Synchronized Reinjection and Coalescence of Droplets in Microfluidics. *Lab Chip*. Epub ahead of print 19 November 2013. DOI: 10.1039/C3LC51214B.
- [121] Nelson BJ, Kaliakatsos IK, Abbott JJ. Microrobots for Minimally Invasive Medicine. *Annu Rev Biomed Eng* 2010; 12: 55–85.
- [122] Peyer KE, Zhang L, Nelson BJ. Bio-inspired magnetic swimming microrobots for biomedical applications. *Nanoscale* 2013; 5: 1259–1272.
- [123] Stanton MM, Trichet-Paredes C, Sánchez S. Applications of three-dimensional (3D) printing for microswimmers and bio-hybrid robotics. *Lab Chip*. Epub ahead of print 29 January 2015. DOI: 10.1039/C5LC90019K.
- [124] Servant A, Qiu F, Mazza M, et al. Controlled In Vivo Swimming of a Swarm of Bacteria-Like Microrobotic Flagella. *Adv Mater* 2015; 27: 2981–2988.

- [125] Berg HC, Anderson RA. Bacteria Swim by Rotating their Flagellar Filaments. *Nature* 1973; 245: 380–382.
- [126] Dreyfus R, Baudry J, Roper ML, et al. Microscopic artificial swimmers. *Nature* 2005; 437: 862–865.
- [127] Zhang L, Peyer KE, Petit T, et al. Motion control of artificial bacterial flagella. 2010, pp. 893–896.
- [128] Gao W, Manesh KM, Hua J, et al. Hybrid Nanomotor: A Catalytically/Magnetically Powered Adaptive Nanowire Swimmer. *Small* 2011; 7: 2047–2051.
- [129] Gibbs JG, Fischer P. Active colloidal microdrills. *Chem Commun* 2015; 51: 4192–4195.
- [130] Toonder J den, Bos F, Broer D, et al. Artificial cilia for active micro-fluidic mixing. *Lab Chip* 2008; 8: 533–541.
- [131] Solvas XC i, Lambert RA, Kulinsky L, et al. Micromixing and flow manipulation with polymer microactuators. *Microfluid Nanofluidics* 2011; 11: 405–416.
- [132] Zhang L, Abbott JJ, Dong L, et al. Micromanipulation using artificial bacterial flagella. In: *IEEE/RSJ International Conference on Intelligent Robots and Systems, 2009. IROS 2009*. 2009, pp. 1401–1406.
- [133] Zhang L, Abbott JJ, Dong L, et al. Characterizing the Swimming Properties of Artificial Bacterial Flagella. *Nano Lett* 2009; 9: 3663–3667.
- [134] Peyer KE, Qiu F, Zhang L, et al. Movement of artificial bacterial flagella in heterogeneous viscous environments at the microscale. In: *2012 IEEE/RSJ International Conference on Intelligent Robots and Systems (IROS)*. 2012, pp. 2553–2558.
- [135] Temel FZ, Erman AG, Yesilyurt S. Characterization and Modeling of Biomimetic Untethered Robots Swimming in Viscous Fluids Inside Circular Channels. *IEEEASME Trans Mechatron* 2014; 19: 1562–1573.
- [136] Tottori S, Zhang L, Qiu F, et al. Magnetic Helical Micromachines: Fabrication, Controlled Swimming, and Cargo Transport. *Adv Mater* 2012; 811–816.
- [137] Huang T-Y, Qiu F, Tung H-W, et al. Cooperative manipulation and transport of microobjects using multiple helical microcarriers. *RSC Adv* 2014; 4: 26771.
- [138] Peters C, Ergeneman O, García PDW, et al. Superparamagnetic Twist-Type Actuators with Shape-Independent Magnetic Properties and Surface Functionalization for Advanced Biomedical Applications. *Adv Funct Mater* 2014; 24: 5269–5276.

- [139] Qiu F, Zhang L, Peyer KE, et al. Noncytotoxic artificial bacterial flagella fabricated from biocompatible ORMOCOMP and iron coating. *J Mater Chem B* 2013; 2: 357–362.
- [140] Suter M, Zhang L, Siringil EC, et al. Superparamagnetic microrobots: fabrication by two-photon polymerization and biocompatibility. *Biomed Microdevices* 2013; 15: 997–1003.
- [141] Qiu F, Fujita S, Mhanna R, et al. Magnetic Helical Microswimmers Functionalized with Lipoplexes for Targeted Gene Delivery. *Adv Funct Mater* 2015; 25: 1666–1671.
- [142] Qiu F, Mhanna R, Zhang L, et al. Artificial bacterial flagella functionalized with temperature-sensitive liposomes for controlled release. *Sens Actuators B Chem* 2014; 196: 676–681.
- [143] Mhanna R, Qiu F, Zhang L, et al. Artificial Bacterial Flagella for Remote-Controlled Targeted Single-Cell Drug Delivery. *Small* 2014; 10: 1953–1957.
- [144] Zhang L, Abbott JJ, Dong L, et al. Artificial bacterial flagella: Fabrication and magnetic control. *Appl Phys Lett* 2009; 94: 064107.
- [145] Cumpston BH, Ananthavel SP, Barlow S, et al. Two-photon polymerization initiators for three-dimensional optical data storage and microfabrication. *Nature* 1999; 398: 51–54.
- [146] Wu S, Serbin J, Gu M. Two-photon polymerisation for three-dimensional micro-fabrication. *J Photochem Photobiol Chem* 2006; 181: 1–11.
- [147] von Freymann G, Ledermann A, Thiel M, et al. Three-Dimensional Nanostructures for Photonics. *Adv Funct Mater* 2010; 20: 1038–1052.
- [148] Juodkazis S, Mizeikis V, Seet KK, et al. Two-photon lithography of nanorods in SU-8 photoresist. *Nanotechnology* 2005; 16: 846.
- [149] De Marco C, Gaidukeviciute A, Kiyan R, et al. A New Perfluoropolyether-Based Hydrophobic and Chemically Resistant Photoresist Structured by Two-Photon Polymerization. *Langmuir* 2013; 29: 426–431.
- [150] Xing J-F, Zheng M-L, Duan X-M. Two-photon polymerization microfabrication of hydrogels: an advanced 3D printing technology for tissue engineering and drug delivery. *Chem Soc Rev*. Epub ahead of print 20 May 2015. DOI: 10.1039/C5CS00278H.
- [151] Kintses B, van Vliet LD, Devenish SR, et al. Microfluidic droplets: new integrated workflows for biological experiments. *Curr Opin Chem Biol* 2010; 14: 548–555.
- [152] Theberge AB, Courtois F, Schaerli Y, et al. Microdroplets in Microfluidics: An Evolving Platform for Discoveries in Chemistry and Biology. *Angew Chem Int Ed* 2010; 49: 5846–5868.

- [153] Chung BG, Lee K-H, Khademhosseini A, et al. Microfluidic fabrication of microengineered hydrogels and their application in tissue engineering. *Lab Chip* 2011; 12: 45–59.
- [154] El-Ali J, Sorger PK, Jensen KF. Cells on chips. *Nature* 2006; 442: 403–411.
- [155] Hindson BJ, Ness KD, Masquelier DA, et al. High-Throughput Droplet Digital PCR System for Absolute Quantitation of DNA Copy Number. *Anal Chem* 2011; 83: 8604–8610.
- [156] Raemdonck K, Demeester J, Smedt SD. Advanced nanogel engineering for drug delivery. *Soft Matter* 2009; 5: 707–715.
- [157] Braschler T, Johann R, Heule M, et al. Gentle cell trapping and release on a microfluidic chip by in situ alginate hydrogel formation. *Lab Chip* 2005; 5: 553–559.
- [158] Tan W-H, Takeuchi S. Dynamic microarray system with gentle retrieval mechanism for cell-encapsulating hydrogel beads. *Lab Chip* 2008; 8: 259–266.
- [159] Chan EM, Alivisatos AP, Mathies RA. High-Temperature Microfluidic Synthesis of CdSe Nanocrystals in Nanoliter Droplets. *J Am Chem Soc* 2005; 127: 13854–13861.
- [160] Niu G, Ruditskiy A, Vara M, et al. Toward continuous and scalable production of colloidal nanocrystals by switching from batch to droplet reactors. *Chem Soc Rev*. Epub ahead of print 11 March 2015. DOI: 10.1039/C5CS00049A.
- [161] Villar G, Graham AD, Bayley H. A Tissue-Like Printed Material. *Science* 2013; 340: 48–52.
- [162] Wauer T, Gerlach H, Mantri S, et al. Construction and Manipulation of Functional Three-Dimensional Droplet Networks. *ACS Nano* 2014; 8: 771–779.
- [163] Stanley CE, Wootton RCR, deMello AJ. Continuous and Segmented Flow Microfluidics: Applications in High-throughput Chemistry and Biology. *Chim Int J Chem* 2012; 66: 88–98.
- [164] Kang D-K, Monsur Ali M, Zhang K, et al. Droplet microfluidics for single-molecule and single-cell analysis in cancer research, diagnosis and therapy. *TrAC Trends Anal Chem* 2014; 58: 145–153.
- [165] Mazutis L, Gilbert J, Ung WL, et al. Single-cell analysis and sorting using droplet-based microfluidics. *Nat Protoc* 2013; 8: 870–891.
- [166] Brouzes E, Kruse T, Kimmerling R, et al. Rapid and continuous magnetic separation in droplet microfluidic devices. *Lab Chip*. Epub ahead of print 11 December 2014. DOI: 10.1039/C4LC01327A.
- [167] Lauga E. Life around the scallop theorem. *Soft Matter* 2011; 7: 3060–3065.

- [168] Li J. Behaviour of titanium and titania-based ceramics in vitro and in vivo. *Biomaterials* 1993; 14: 229–232.
- [169] Swaay D van, Mächler J-P, Stanley C, et al. A chip-to-world connector with a built-in reservoir for simple small-volume sample injection. *Lab Chip* 2013; 14: 178–181.
- [170] Kemna EWM, Schoeman RM, Wolbers F, et al. High-yield cell ordering and deterministic cell-in-droplet encapsulation using Dean flow in a curved microchannel. *Lab Chip* 2012; 12: 2881–2887.
- [171] Abate AR, Chen C-H, Agresti JJ, et al. Beating Poisson encapsulation statistics using close-packed ordering. *Lab Chip* 2009; 9: 2628–2631.
- [172] Edd JF, Carlo DD, Humphry KJ, et al. Controlled encapsulation of single-cells into monodisperse picolitre drops. *Lab Chip* 2008; 8: 1262–1264.
- [173] Tottori S, Zhang L, Peyer KE, et al. Assembly, Disassembly, and Anomalous Propulsion of Microscopic Helices. *Nano Lett* 2013; 13: 4263–4268.
- [174] Holt DJ, Payne RJ, Chow WY, et al. Fluorosurfactants for microdroplets: Interfacial tension analysis. *J Colloid Interface Sci* 2010; 350: 205–211.
- [175] Velev OD, Prevo BG, Bhatt KH. On-chip manipulation of free droplets. *Nature* 2003; 426: 515–516.
- [176] Jung Y-M, Kang IS. A novel actuation method of transporting droplets by using electrical charging of droplet in a dielectric fluid. *Biomicrofluidics* 2009; 3: 022402.
- [177] Wixforth A, Strobl C, Gauer C, et al. Acoustic manipulation of small droplets. *Anal Bioanal Chem* 2004; 379: 982–991.
- [178] Pei SN, Valley JK, Neale SL, et al. Light-actuated digital microfluidics for large-scale, parallel manipulation of arbitrarily sized droplets. In: *2010 IEEE 23rd International Conference on Micro Electro Mechanical Systems (MEMS)*. 2010, pp. 252–255.
- [179] Cho SK, Moon H, Kim C-J. Creating, transporting, cutting, and merging liquid droplets by electro-wetting-based actuation for digital microfluidic circuits. *J Microelectromechanical Syst* 2003; 12: 70–80.
- [180] Jebrail MJ, Bartsch MS, Patel KD. Digital microfluidics: a versatile tool for applications in chemistry, biology and medicine. *Lab Chip* 2012; 12: 2452–2463.
- [181] Walczak MM, Leavitt PK, Thiel PA. Oxygenated fluorocarbons adsorbed at metal surfaces: chemisorption bond strengths and decomposition. *J Am Chem Soc* 1987; 109: 5621–5627.

- [182] Sakar MS, Steager EB, Kim DH, et al. Single cell manipulation using ferromagnetic composite microtransporters. *Appl Phys Lett* 2010; 96: 043705.
- [183] Medina-Sánchez M, Schwarz L, Meyer AK, et al. Cellular Cargo Delivery: Toward Assisted Fertilization by Sperm-Carrying Micromotors. *Nano Lett* 2016; 16: 555–561.
- [184] Behjati S, Tarpey PS. What is next generation sequencing? *Arch Dis Child Educ Pract Ed* 2013; 98: 236–238.
- [185] Nederbragt L. developments in NGS. Epub ahead of print 8 July 2016. DOI: 10.6084/m9.figshare.100940.v9.
- [186] Levy SE, Myers RM. Advancements in Next-Generation Sequencing. *Annu Rev Genomics Hum Genet* 2016; 17: null.
- [187] Treangen TJ, Salzberg SL. Repetitive DNA and next-generation sequencing: computational challenges and solutions. *Nat Rev Genet* 2012; 13: 36–46.
- [188] Kuleshov V, Xie D, Chen R, et al. Whole-genome haplotyping using long reads and statistical methods. *Nat Biotechnol* 2014; 32: 261–266.
- [189] Li R, Hsieh C-L, Young A, et al. Illumina Synthetic Long Read Sequencing Allows Recovery of Missing Sequences even in the 'Finished' *C. elegans* Genome. *Sci Rep* 2015; 5: 10814.
- [190] Amini S, Pushkarev D, Christiansen L, et al. Haplotype-resolved whole-genome sequencing by contiguity-preserving transposition and combinatorial indexing. *Nat Genet* 2014; 46: 1343–1349.
- [191] Tilgner H, Jahanbani F, Blauwkamp T, et al. Comprehensive transcriptome analysis using synthetic long-read sequencing reveals molecular co-association of distant splicing events. *Nat Biotechnol* 2015; 33: 736–742.
- [192] Goodwin S, McPherson JD, McCombie WR. Coming of age: ten years of next-generation sequencing technologies. *Nat Rev Genet* 2016; 17: 333–351.
- [193] Adey A, Kitzman JO, Burton JN, et al. In vitro, long-range sequence information for de novo genome assembly via transposase contiguity. *Genome Res* 2014; 24: 2041–2049.
- [194] Zheng GXY, Lau BT, Schnall-Levin M, et al. Haplotyping germline and cancer genomes with high-throughput linked-read sequencing. *Nat Biotechnol* 2016; 34: 303–311.
- [195] DeKosky BJ, Ippolito GC, Deschner RP, et al. High-throughput sequencing of the paired human immunoglobulin heavy and light chain repertoire. *Nat Biotechnol* 2013; 31: 166–169.

- [196] DeKosky BJ, Kojima T, Rodin A, et al. In-depth determination and analysis of the human paired heavy- and light-chain antibody repertoire. *Nat Med* 2014; 21: 86–91.
- [197] Mullis K, Faloona F, Scharf S, et al. Specific Enzymatic Amplification of DNA In Vitro: The Polymerase Chain Reaction. *Cold Spring Harb Symp Quant Biol* 1986; 51: 263–273.
- [198] Bell LE. Cooling, Heating, Generating Power, and Recovering Waste Heat with Thermoelectric Systems. *Science* 2008; 321: 1457–1461.
- [199] Woolley AT, Hadley D, Landre P, et al. Functional Integration of PCR Amplification and Capillary Electrophoresis in a Microfabricated DNA Analysis Device. *Anal Chem* 1996; 68: 4081–4086.
- [200] Kopp MU, Mello AJ de, Manz A. Chemical Amplification: Continuous-Flow PCR on a Chip. *Science* 1998; 280: 1046–1048.
- [201] Diehl F, Li M, He Y, et al. BEAMing: single-molecule PCR on microparticles in water-in-oil emulsions. *Nat Methods* 2006; 3: 551–559.
- [202] White RA, Blainey PC, Fan HC, et al. Digital PCR provides sensitive and absolute calibration for high throughput sequencing. *BMC Genomics* 2009; 10: 116.
- [203] Tewhey R, Warner JB, Nakano M, et al. Microdroplet-based PCR enrichment for large-scale targeted sequencing. *Nat Biotechnol* 2009; 27: 1025–1031.
- [204] Nishikawa Y, Hosokawa M, Maruyama T, et al. Monodisperse Picoliter Droplets for Low-Bias and Contamination-Free Reactions in Single-Cell Whole Genome Amplification. *PLOS ONE* 2015; 10: e0138733.
- [205] Kiss MM, Ortoleva-Donnelly L, Beer NR, et al. High-Throughput Quantitative Polymerase Chain Reaction in Picoliter Droplets. *Anal Chem* 2008; 80: 8975–8981.
- [206] Sgro AE, Allen PB, Chiu DT. Thermoelectric Manipulation of Aqueous Droplets in Microfluidic Devices. *Anal Chem* 2007; 79: 4845–4851.
- [207] Hettiarachchi K, Kim H, Faris GW. Optical manipulation and control of real-time PCR in cell encapsulating microdroplets by IR laser. *Microfluid Nanofluidics* 2012; 13: 967–975.
- [208] Fakruddin M, Mannan KSB, Chowdhury A, et al. Nucleic acid amplification: Alternative methods of polymerase chain reaction. *J Pharm Bioallied Sci* 2013; 5: 245–252.
- [209] Zanolini LM, Spoto G. Isothermal Amplification Methods for the Detection of Nucleic Acids in Microfluidic Devices. *Biosensors* 2012; 3: 18–43.

- [210] Mori Y, Notomi T. Loop-mediated isothermal amplification (LAMP): a rapid, accurate, and cost-effective diagnostic method for infectious diseases. *J Infect Chemother* 2009; 15: 62–69.
- [211] Poon LLM, Leung CSW, Tashiro M, et al. Rapid Detection of the Severe Acute Respiratory Syndrome (SARS) Coronavirus by a Loop-Mediated Isothermal Amplification Assay. *Clin Chem* 2004; 50: 1050–1052.
- [212] Surabattula R, Vejandla MP, Mallepaddi PC, et al. Simple, rapid, inexpensive platform for the diagnosis of malaria by loop mediated isothermal amplification (LAMP). *Exp Parasitol* 2013; 134: 333–340.
- [213] Njiru ZK, Mikosza ASJ, Armstrong T, et al. Loop-Mediated Isothermal Amplification (LAMP) Method for Rapid Detection of *Trypanosoma brucei rhodesiense*. *PLoS Negl Trop Dis* 2008; 2: e147.
- [214] Tomita N, Mori Y, Kanda H, et al. Loop-mediated isothermal amplification (LAMP) of gene sequences and simple visual detection of products. *Nat Protoc* 2008; 3: 877–882.
- [215] Damhorst GL, Duarte-Guevara C, Chen W, et al. Smartphone-Imaged HIV-1 Reverse-Transcription Loop-Mediated Isothermal Amplification (RT-LAMP) on a Chip from Whole Blood. *Engineering* 2015; 1: 324–335.
- [216] Rane TD, Chen L, Zec HC, et al. Microfluidic continuous flow digital loop-mediated isothermal amplification (LAMP). *Lab Chip* 2015; 15: 776–782.
- [217] Turchaninova MA, Britanova OV, Bolotin DA, et al. Pairing of T-cell receptor chains via emulsion PCR. *Eur J Immunol* 2013; 43: 2507–2515.
- [218] Klein AM, Mazutis L, Akartuna I, et al. Droplet Barcoding for Single-Cell Transcriptomics Applied to Embryonic Stem Cells. *Cell* 2015; 161: 1187–1201.
- [219] Tao Y, Rotem A, Zhang H, et al. Artifact-Free Quantification and Sequencing of Rare Recombinant Viruses by Using Drop-Based Microfluidics. *ChemBioChem* 2015; 16: 2167–2171.
- [220] McDaniel JR, DeKosky BJ, Tanno H, et al. Ultra-high-throughput sequencing of the immune receptor repertoire from millions of lymphocytes. *Nat Protoc* 2016; 11: 429–442.
- [221] Vogelstein B, Kinzler KW. Digital PCR. *Proc Natl Acad Sci* 1999; 96: 9236–9241.
- [222] Schuler F, Schwemmer F, Trotter M, et al. Centrifugal step emulsification applied for absolute quantification of nucleic acids by digital droplet RPA. *Lab Chip*. Epub ahead of print 7 May 2015. DOI: 10.1039/C5LC00291E.

- [223] Dressman D, Yan H, Traverso G, et al. Transforming single DNA molecules into fluorescent magnetic particles for detection and enumeration of genetic variations. *Proc Natl Acad Sci* 2003; 100: 8817–8822.
- [224] Ottesen EA, Hong JW, Quake SR, et al. Microfluidic Digital PCR Enables Multigene Analysis of Individual Environmental Bacteria. *Science* 2006; 314: 1464–1467.
- [225] Hindson CM, Chevillet JR, Briggs HA, et al. Absolute quantification by droplet digital PCR versus analog real-time PCR. *Nat Methods* 2013; 10: 1003–1005.
- [226] Debrand E, Lykoudi A, Bradshaw E, et al. A Non-Invasive Droplet Digital PCR (ddPCR) Assay to Detect Paternal CFTR Mutations in the Cell-Free Fetal DNA (cffDNA) of Three Pregnancies at Risk of Cystic Fibrosis via Compound Heterozygosity. *PLOS ONE* 2015; 10: e0142729.
- [227] Mehrian-Shai R, Yalon M, Moshe I, et al. Identification of genomic aberrations in hemangioblastoma by droplet digital PCR and SNP microarray highlights novel candidate genes and pathways for pathogenesis. *BMC Genomics* 2016; 17: 56.
- [228] Watanabe M, Kawaguchi T, Isa S, et al. Ultra-Sensitive Detection of the Pretreatment EGFR T790M Mutation in Non-Small Cell Lung Cancer Patients with an EGFR-Activating Mutation Using Droplet Digital PCR. *Clin Cancer Res* 2015; 21: 3552–3560.
- [229] Trypsteen W, Kiselina M, Vandekerckhove L, et al. Diagnostic utility of droplet digital PCR for HIV reservoir quantification. *J Virus Erad* 2016; 2: 162–169.
- [230] Orhant L, Anselem O, Fradin M, et al. Droplet digital PCR combined with minisequencing, a new approach to analyze fetal DNA from maternal blood: application to the non-invasive prenatal diagnosis of achondroplasia. *Prenat Diagn* 2016; 36: 397–406.
- [231] Lièvre A, Bachet J-B, Corre DL, et al. KRAS Mutation Status Is Predictive of Response to Cetuximab Therapy in Colorectal Cancer. *Cancer Res* 2006; 66: 3992–3995.
- [232] Gazdar A. Activating and resistance mutations of EGFR in non-small-cell lung cancer: role in clinical response to EGFR tyrosine kinase inhibitors. *Oncogene* 2009; 28: S24–S31.
- [233] Siravegna G, Mussolin B, Buscarino M, et al. Clonal evolution and resistance to EGFR blockade in the blood of colorectal cancer patients. *Nat Med* 2015; 21: 795–801.
- [234] Zhong Q, Bhattacharya S, Kotsopoulos S, et al. Multiplex digital PCR: breaking the one target per color barrier of quantitative PCR. *Lab Chip* 2011; 11: 2167–2174.
- [235] Taly V, Pekin D, Benhaim L, et al. Multiplex Picodroplet Digital PCR to Detect KRAS Mutations in Circulating DNA from the Plasma of Colorectal Cancer Patients. *Clin Chem* 2013; 59: 1722–1731.

- [236] Miotke L, Lau BT, Rumma RT, et al. High Sensitivity Detection and Quantitation of DNA Copy Number and Single Nucleotide Variants with Single Color Droplet Digital PCR. *Anal Chem* 2014; 86: 2618–2624.
- [237] Petriv OI, Heyries KA, VanInsberghe M, et al. Methods for Multiplex Template Sampling in Digital PCR Assays. *PLOS ONE* 2014; 9: e98341.
- [238] Elowitz MB, Levine AJ, Siggia ED, et al. Stochastic Gene Expression in a Single Cell. *Science* 2002; 297: 1183–1186.
- [239] Liberali P, Snijder B, Pelkmans L. Single-cell and multivariate approaches in genetic perturbation screens. *Nat Rev Genet* 2015; 16: 18–32.
- [240] Greaves M, Maley CC. Clonal evolution in cancer. *Nature* 2012; 481: 306–313.
- [241] Proserpio V, Mahata B. Single-cell technologies to study the immune system. *Immunology* 2016; 147: 133–140.
- [242] Xu X, Hou Y, Yin X, et al. Single-Cell Exome Sequencing Reveals Single-Nucleotide Mutation Characteristics of a Kidney Tumor. *Cell* 2012; 148: 886–895.
- [243] Gawad C, Koh W, Quake SR. Single-cell genome sequencing: current state of the science. *Nat Rev Genet* 2016; 17: 175–188.
- [244] Macosko EZ, Basu A, Satija R, et al. Highly Parallel Genome-wide Expression Profiling of Individual Cells Using Nanoliter Droplets. *Cell* 2015; 161: 1202–1214.
- [245] Picelli S. Single-cell RNA-sequencing: The future of genome biology is now. *RNA Biol* 2016; 0: 1–14.
- [246] Collins DJ, Neild A, deMello A, et al. The Poisson distribution and beyond: methods for microfluidic droplet production and single cell encapsulation. *Lab Chip* 2015; 15: 3439–3459.
- [247] Martel JM, Toner M. Inertial Focusing in Microfluidics. *Annu Rev Biomed Eng* 2014; 16: 371–396.
- [248] Zheng GXY, Terry JM, Belgrader P, et al. Massively parallel digital transcriptional profiling of single cells. *bioRxiv* 2016; 065912.
- [249] Fu Y, Li C, Lu S, et al. Uniform and accurate single-cell sequencing based on emulsion whole-genome amplification. *Proc Natl Acad Sci* 2015; 112: 11923–11928.

- [250] Rotem A, Ram O, Shores N, et al. Single-cell ChIP-seq reveals cell subpopulations defined by chromatin state. *Nat Biotechnol* 2015; 33: 1165–1172.
- [251] Eastburn DJ, Sciambi A, Abate AR. Identification and genetic analysis of cancer cells with PCR-activated cell sorting. *Nucleic Acids Res* 2014; 42: e128–e128.
- [252] Leng X, Zhang W, Wang C, et al. Agarose droplet microfluidics for highly parallel and efficient single molecule emulsion PCR. *Lab Chip* 2010; 10: 2841–2843.
- [253] Kumachev A, Greener J, Tumarkin E, et al. High-throughput generation of hydrogel microbeads with varying elasticity for cell encapsulation. *Biomaterials* 2011; 32: 1477–1483.
- [254] Novak R, Zeng Y, Shuga J, et al. Single-Cell Multiplex Gene Detection and Sequencing with Microfluidically Generated Agarose Emulsions. *Angew Chem Int Ed* 2011; 50: 390–395.
- [255] Zhang H, Jenkins G, Zou Y, et al. Massively Parallel Single-Molecule and Single-Cell Emulsion Reverse Transcription Polymerase Chain Reaction Using Agarose Droplet Microfluidics. *Anal Chem* 2012; 84: 3599–3606.
- [256] Geng T, Novak R, Mathies RA. Single-Cell Forensic Short Tandem Repeat Typing within Microfluidic Droplets. *Anal Chem* 2014; 86: 703–712.
- [257] Sørli T, Perou CM, Tibshirani R, et al. Gene expression patterns of breast carcinomas distinguish tumor subclasses with clinical implications. *Proc Natl Acad Sci* 2001; 98: 10869–10874.
- [258] Lawson DA, Bhakta NR, Kessenbrock K, et al. Single-cell analysis reveals a stem-cell program in human metastatic breast cancer cells. *Nature* 2015; 526: 131–135.
- [259] Humphries C. Adoptive cell therapy: Honing that killer instinct. *Nature* 2013; 504: S13–S15.
- [260] Dudley ME, Yang JC, Sherry R, et al. Adoptive Cell Therapy for Patients With Metastatic Melanoma: Evaluation of Intensive Myeloablative Chemoradiation Preparative Regimens. *J Clin Oncol* 2008; 26: 5233–5239.
- [261] Rosenberg SA, Restifo NP. Adoptive cell transfer as personalized immunotherapy for human cancer. *Science* 2015; 348: 62–68.
- [262] WHO | Cancer. *WHO* <http://www.who.int/mediacentre/factsheets/fs297/en/> (accessed 29 August 2017).

- [263] Irving M, Vuillefroy de Silly R, Scholten K, et al. Engineering Chimeric Antigen Receptor T-Cells for Racing in Solid Tumors: Don't Forget the Fuel. *Front Immunol*; 8. Epub ahead of print 2017. DOI: 10.3389/fimmu.2017.00267.
- [264] Takayama T, Sekine T, Makuuchi M, et al. Adoptive immunotherapy to lower postsurgical recurrence rates of hepatocellular carcinoma: a randomised trial. *Lancet Lond Engl* 2000; 356: 802–807.
- [265] H Clevers, B Alarcon, T Wileman, et al. The T Cell Receptor/CD3 Complex: A Dynamic Protein Ensemble. *Annu Rev Immunol* 1988; 6: 629–662.
- [266] Moffatt MF, Hill MR, Faux JA, et al. Genetic linkage of T-cell receptor α/δ complex to specific IgE responses. *The Lancet* 1994; 343: 1597–1600.
- [267] Nunes JK, Tsai SSH, Wan J, et al. Dripping and jetting in microfluidic multiphase flows applied to particle and fiber synthesis. *J Phys Appl Phys*; 46. Epub ahead of print 20 March 2013. DOI: 10.1088/0022-3727/46/11/114002.
- [268] Munson DJ, Egelston CA, Chiotti KE, et al. Identification of shared TCR sequences from T cells in human breast cancer using emulsion RT-PCR. *Proc Natl Acad Sci* 2016; 113: 8272–8277.
- [269] Carlo DD. Inertial microfluidics. *Lab Chip* 2009; 9: 3038–3046.
- [270] Commissioner O of the. Press Announcements - FDA approval brings first gene therapy to the United States <https://www.fda.gov/NewsEvents/Newsroom/PressAnnouncements/ucm574058.htm> (accessed 10 September 2017).
- [271] Cao X, deMello AJ, Elvira KS. Enhanced versatility of fluid control in centrifugal microfluidic platforms using two degrees of freedom. *Lab Chip* 2016; 16: 1197–1205.
- [272] Maceiczuk RM, deMello AJ. Fast and Reliable Metamodeling of Complex Reaction Spaces Using Universal Kriging. *J Phys Chem C* 2014; 118: 20026–20033.
- [273] Reizman BJ, Jensen KF. Feedback in Flow for Accelerated Reaction Development. *Acc Chem Res* 2016; 49: 1786–1796.
- [274] Weaver JA, Melin J, Stark D, et al. Static control logic for microfluidic devices using pressure-gain valves. *Nat Phys* 2010; 6: 218–223.
- [275] Wang J, Brisk P, Grover WH. Random design of microfluidics. *Lab Chip*. Epub ahead of print 28 September 2016. DOI: 10.1039/C6LC00758A.

Curriculum Vitae

Yun Ding

Nationality: China
Date of Birth: 22.07.1986

ETH Zurich
HCI F 106
Vladimir-Prelog-Weg 1-5 / 10
8093 Zurich
Switzerland

+41 44 633 44 96
yun.ding@chem.ethz.ch

Education

- 2012–2017 **PhD Chemical Engineering**, *ETH Zurich*, Switzerland.
- 2010–2012 **MSc Chemical and Bioengineering**, *ETH Zurich*, Switzerland.
- 2005–2009 **BEng Pharmaceutical Engineering**, *Zhejiang University*, China.
- 2009 Spring **Exchange student**, *Czech Technical University in Prague*, Czech Republic.

Publications

- [1] Ding, Y., Choo, J., and deMello, A.J. (2017). From single-molecule detection to next-generation sequencing: microfluidic droplets for high-throughput nucleic acid analysis. *Microfluidics and Nanofluidics*, 21, 58.
- [2] Ding, Y., Qiu, F., Casadevall i Solvas, X., Chiu, F. W. Y., Nelson, B. J., & deMello, A. (2016). Microfluidic-Based Droplet and Cell Manipulations Using Artificial Bacterial Flagella. *Micromachines*, 7(2), 25.
- [3] Ding, Y., Casadevall i Solvas, X., & deMello, A. (2014). “V-junction”: a novel structure for high-speed generation of bespoke droplet flows. *The Analyst*, 140, 414-421. (**Inside cover article**).
- [4] Qiu, F., Mhanna, R., Zhang, L., Ding, Y., Fujita, S., & Nelson, B. J. (2014). Artificial bacterial flagella functionalized with temperature-sensitive liposomes for controlled release. *Sensors and Actuators B: Chemical*, 196, 676-681.
- [5] Mhanna, R., Qiu, F., Zhang, L., Ding, Y., Sugihara, K., Zenobi-Wong, M., & Nelson, B. J. (2014). Artificial Bacterial Flagella for Remote-Controlled Targeted Single-Cell Drug Delivery. *Small*, 10(10), 1953-1957.

Conference

- [1] Ding Y, Schanz M, Casadevall i Solvas X, Huber M, deMello A. A Highly Efficient Droplet-Based Microfluidic Strategy for Next-Generation Sequencing in Single Cell Level. *ICMFLOC 2016*, Dalian, China, oral presentation.
- [2] Ding Y, Stavrakis S, Casadevall i Solvas X, deMello A. A High Throughput Droplet-Based Microfluidic Barcode Generator. *MicroTAS 2013*, Freiburg, Germany, 299-301.
- [3] Qiu F, Mhanna R, Zhang L, Ding Y, Tottori S, Sugihara K, Zenobi-Wong M, Nelson B. Artificial Bacterial Flagella Functionalized with Temperature-sensitive Liposomes for Biomedical Applications. *Transducers 2013*, Barcelona, Spain, 2130-2133.

